tude smaller than in the adjacent hypolimnion. Practically, the turbulent boundary layer is well-mixed and not stratified by temperature. Also excluded can be a chemical stratification. In fact, WÜEST AND GLOOR [298] took Lake Alpnach as an explicit example for a lake in which the stratification by dissolved solids, important in the main basin of Lake Lucerne, can be neglected. A density stratification caused by resuspended particles, as described for the same lake by GLOOR ET AL. [91], is unlikely since resuspension is reported only for burst-like events during which the current speed exceeded 7cm/s, a value not recorded in the measuring period.
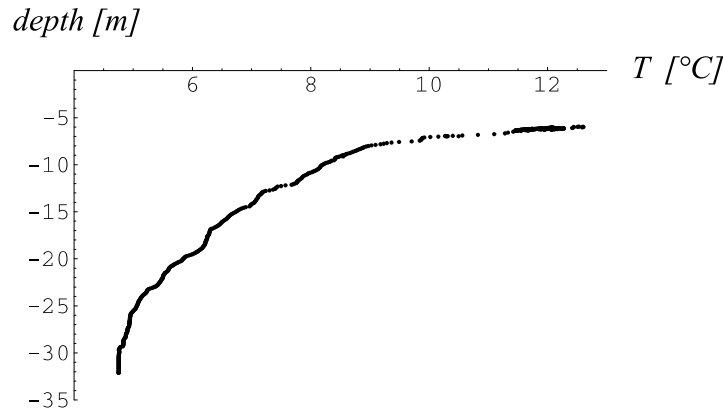

Figure 4.11: Typical temperature profile for the measuring period. At the bottom a well-mixed layer of approximately 3 m height can be recognized.

If the velocity profiles are averaged to filter out their fluctuating parts, mean profiles as illustrated in Fig. 4.12 are obtained. It turns out that during periods of maximum current speed an almost perfect logarithmic curve fit to the velocity profiles is possible (right profile in Fig. 4.12). Even though tempting, it is very questionable to imply that these profiles coincide with the logarithmic velocity profiles of the "clean" and steady-state law-of-the-wall obtained in standard laboratory setups. The arguments of several authors cited in the introduction to this section, and the reasoning used in this work below, demonstrate that a logarithmic function has powerful interpolating properties, but is probably not always an indicator for the existence of the law-of-the-wall. Another interesting feature exhibited by the velocity profile on the right panel of Fig. 4.12 is the maximum of the current speed at a height of approximately 3.5 m. It will be shown below, that it can be explained by considering a small phase-lag of the velocity at different heights.

Logarithmic interpolations like that in Fig. 4.12 can be found by simply adjusting a logarithmic function with the two fit parameters "friction velocity", u_*, and "roughness
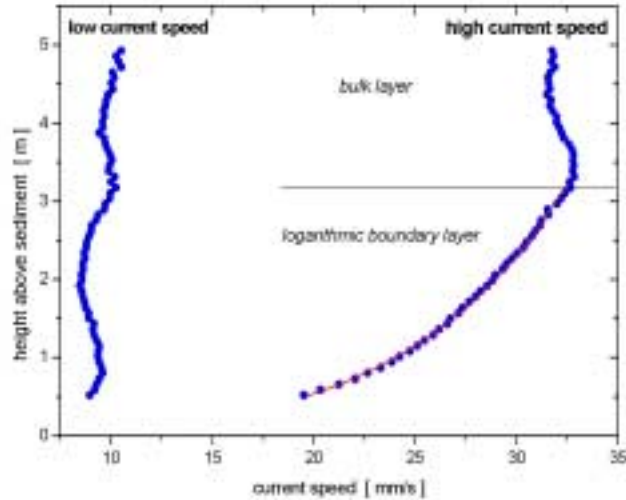
Figure 4.12:   Typical time averaged velocity profiles at flow reversal (left) and at maximum current speed. Note the maximum in the velocity profile at a height of approximately 3.5 m. Also included is a logarithmic curve fit to the right profile. (Courtesy of A. Lorke)

height", z_0, to the measured velocity profiles. The results for a number of measured profiles are displayed in Fig. 4.13. Comparing the left panel of this figure to the velocity time series in Fig. 4.10, a clear correlation with u_* can be recognized: At periods of high current speed also the friction velocity is high. The quantitative agreement, however, is less satisfactory: A simple friction law of the form $u_*^2 = c_{1m}\, u_{1m}^2$ yields a maximum current speed of approximately $u_{1m} = 0.09$ m/s one meter above the sediment, if u_* is taken from Fig. 4.13 and a drag coefficient $c_{1m} = 1.6 \cdot 10^{-3}$, suggested by WÜEST AND GLOOR [298] for this lake, is used. It can be seen from Fig. 4.10 and Fig. 4.12 that the value of u_{1m} is at least twice too large. The picture is even less consistent for the roughness
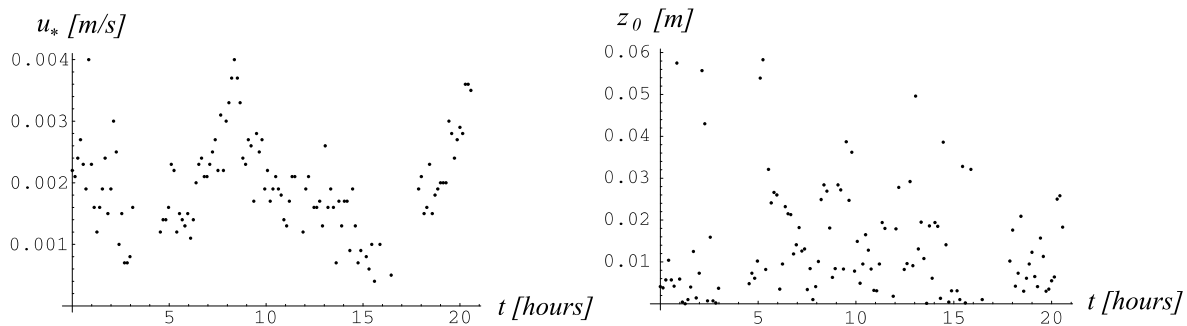

Figure 4.13:   Friction velocity, u_* (left panel), and bottom roughness length, z_0 (right panel), obtained by a number of logarithmic curve fits as that in Fig. 4.12. The von Kármán constant was assigned a value of $\kappa = 0.4$.

length, shown on the right panel of Fig. 4.13. The values for z_0 are scattered over one order of magnitude. Using the relation (A.15), values computed for the sand roughness, k_s, correspond to roughness elements of tens of centimetres diameter. This is one or two orders of magnitude too high, if compared to values reasonable for the sediment structure of this lake (A. Lorke, pers. comm.). On the other hand, if a viscous sub-layer is assumed at the lake bottom, (A.11) implies that the "roughness length" z_0 varies as u_*^{-1}. Clearly, such a systematic dependence is not corroborated by the data displayed in Fig. 4.13.

A second method of estimating values of the friction velocity is based on measurements of the rate of dissipation, ϵ. If this quantity is known, the friction velocity can be inferred from the logarithmic boundary layer relation (see Appendix (A.1))

$$\epsilon = \frac{u_*^3}{\kappa(z + z_0)} \quad . \tag{4.9}$$

Even though this method also relies on the existence of a logarithmic region in the law-of-the-wall, errors obtained in u_* will be much smaller, simply because of the fact that u_* is computed as the cubic root of an expression according to (4.9). On the other hand, if the rate of dissipation is obtained from u_* (estimated from a logarithmic fit of the velocity profile), errors in u_* will be amplified by the third power of u_* in (4.9). If u_* is overestimated by a factor of 2 or more (see above), the computed ϵ will be almost an order of magnitude too high.

The second method was used more than a decade ago by DEWEY AND CRAWFORD [63] for the determination of the friction velocity on the continental shelf near Vancouver Island. They pointed out that bottom stress estimates obtained with the dissipation method were consistently 4.5 times smaller than those obtained from logarithmic curve fits. This picture is consistent with the preliminary lake data of the EAWAG. Fig. 4.14 clearly demonstrates that dissipation rates from the law-of-the-wall fit are at least one order of magnitude larger than those obtained from microstructure profiles.

Interestingly, Fig. 4.14 also indicates a phase shift of about 2 hours between the rate of dissipation directly measured and obtained from a law-of-the-wall fit (compare the data between 20.00h and 22.00h). However, the data are a bit scattered and an entirely conclusive decision has to await the complete evaluation of all microstructure profiles.
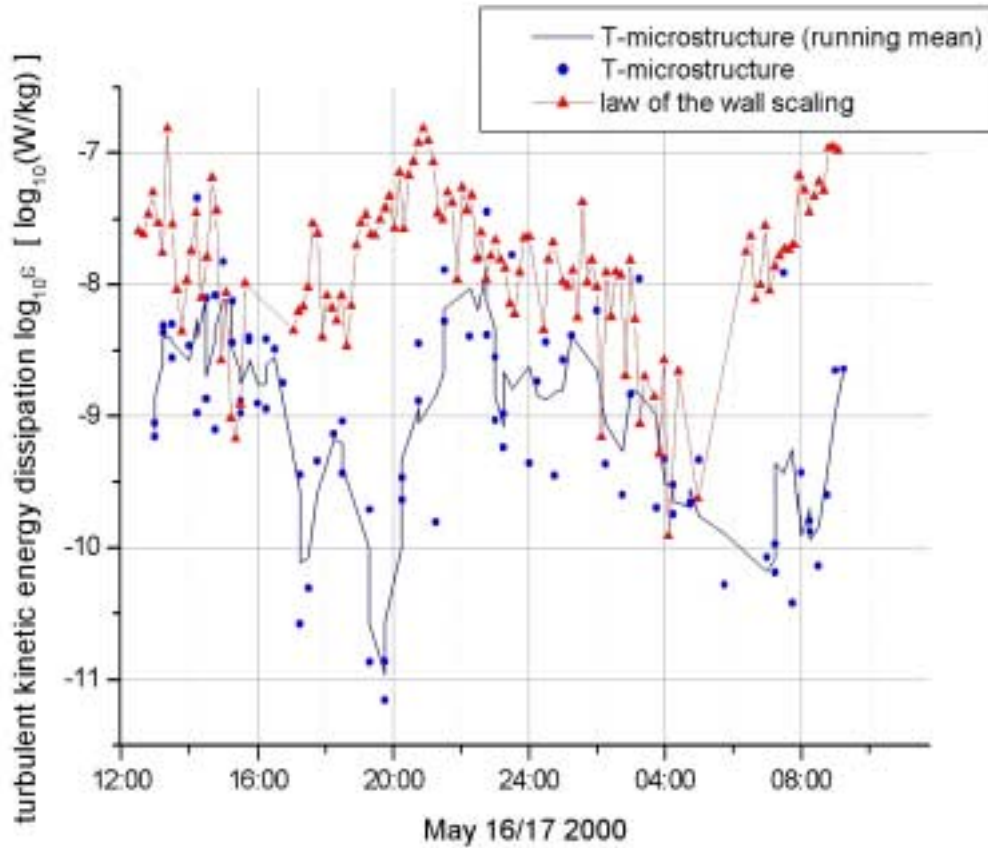
Figure 4.14:   Dissipation rates estimated from fits of the logarithmic velocity profiles
and from microstructure measurements in the bottom boundary layer at 1m height
above the sediment. Courtesy of A. Lorke

4.2.2   The Model

The seiche-induced bottom boundary layer will be modelled as an oscillating, horizon-
tal, non-rotating boundary layer. With these simplifications the one-dimensional models
developed in Chapters 1 and 2 can be applied. The driving force is an oscillating pressure-
gradient, imposed by the outer flow, of the form

$$\frac{1}{\rho_0}\frac{\partial p}{\partial x} = -P\cos\left(\omega t + \varphi_0\right) \quad \text{for } t \geq 0 , \quad \omega = \frac{2\pi}{T} , \tag{4.10}$$

where T is the seiche period, P the amplitude of the pressure-gradient, and φ_0 a phase-
shift. If the x-axis is aligned with the mean flow direction, (2.37) can be re-written for
the oscillating boundary layer as

$$\frac{\partial u}{\partial t} = P\cos\left(\omega t + \varphi_0\right) - \frac{\partial\langle u'w'\rangle}{\partial z} \quad . \tag{4.11}$$

If the vertical momentum flux contribution is negligible, this equation integrates to

$$u = \frac{P}{\omega} \sin \frac{2\pi t}{T} ,$$ (4.12)

where the phase-shift $\varphi_0 = 0$ has been chosen to correspond to the initial condition $u = 0$ at $t = 0$.

In the general case, when the turbulent momentum flux is retained, both, u and $\langle u'w' \rangle$ will be periodic functions of time after the initial disturbances have died away. However, due to the non-linearity of the turbulence models it cannot be expected in general that the simple trigonometric form of the forcing (4.10) will be preserved in u and $\langle u'w' \rangle$. Nevertheless, the following useful result can be obtained, if it is assumed that $\langle u'w' \rangle$ is *approximately* trigonometric: Then, setting

$$\frac{\partial \langle u'w' \rangle}{\partial z} = F(z) \sin \left(\omega t + \varphi_1 \left(z \right) \right) ,$$ (4.13)

where $\varphi_1(z) \neq \varphi_0$ is a phase-shift determined by the turbulence model, it can be shown by using some well-known trigonometric relations that the velocity is of the form

$$u(z) = U(z) \sin \left(\omega t + \varphi_2 \left(z \right) \right) ,$$ (4.14)

where both, amplitude U and phase-shift $\varphi_2(z)$ are functions of the parameters P/ω, F/ω, and φ_1. To make the point, changes in the amplitude of the friction terms will not only influence the amplitude of the velocity, but also its phase. It will be shown below, that this result also holds, if u and $\langle u'w' \rangle$ are not strictly trigonometric functions.

This section is structured as follows: After a first part, in which an appropriate value of the roughness length, z_0, is determined and results from the k-ω model and the k-ϵ model are compared, properties of the unstratified bottom boundary layer are investigated. Then, the influence of stratification is discussed. The height of the well mixed bottom layer for different stratifications will be compared to the measurements in Lake Alpnach. It will be demonstrated that stratification has only a relatively small influence on turbulent quantities, *once* a well mixed bottom boundary layer has been eroded. This implies that most of the results for the unstratified case also apply to (initially) stratified boundary layers. It will be demonstrated that the measured and computed dissipation rates are in good agreement. However, the phase-lag with respect to the velocity field is apparently underestimated by the two-equation models.

In all cases, except in the stratified ones, the results are presented after the initial disturbances have died away and the model has run into a quasi steady-state, where phase and amplitude of the oscillating fields are approximately constant.

Influence of the Roughness Length

Before the models can be applied to the bottom boundary layer of Lake Alpnach, an important model parameter, the roughness length z_0, has to be adjusted. It has been argued above that a roughness length of order $z_0 \approx 0.01\,\text{m}$ (see Fig. 4.13) is at least an order of magnitude too large. It is, however, unclear if a roughness length of $z_0 \approx 0.001\,\text{m}$ or a hydrodynamically smooth surface should be assumed in the models. To estimate the sensitivity of the models to the choice of z_0, computations for different values of this parameter have been conducted.

Fig. 4.15 displays model results for a pressure-gradient of the form (4.10) (with a seiche[4] period of 6 hours) and different roughness parameterizations.
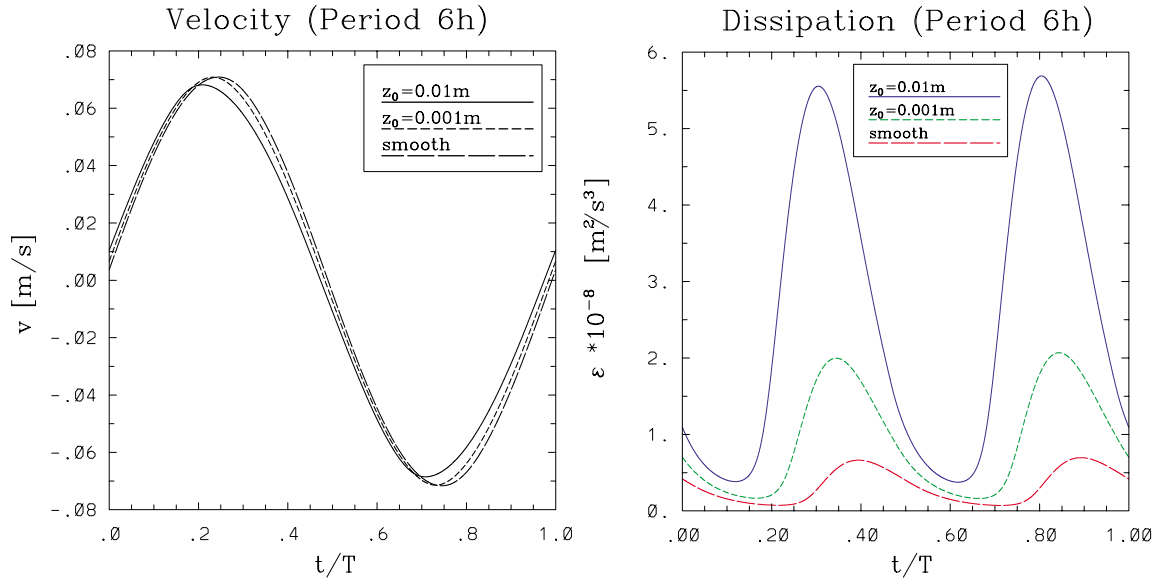

Figure 4.15:   Velocity (left panel) and turbulent dissipation rate (right panel) at $2.5\,\text{m}$ above the sediment for different values of the bottom roughness length, z_0. Pressure-gradient according to (4.10) with amplitude $\frac{1}{\rho}\frac{\partial p}{\partial x} = 2 \cdot 10^{-5}\ \text{m/s}^2$. The seiche period is $T = 6\,\text{h}$.

The left panel of this figure shows that turbulent friction cannot have a large influence on the velocity field: The numerical solution is very similar to the simple sine curve of (4.12) for the frictionless case. Hence, the main balance in (4.11) is between the rate term and

---

[4]The term "seiche" is used here as a synonym for "oscillation", even though a seiche strictly relates only to an internal oscillation with the eigenfrequency of a basin. However, it is irrelevant for an oscillating boundary layer by which mechanism the pressure-gradient imposed by the outer flow is generated as long as the vertical velocity shear of the corresponding vertical seiche mode is weak in the boundary layer.

the pressure-gradient. Nevertheless, the numerical solution exhibits a small phase-shift and a reduction of the amplitude for all values of z_0. The phase-shift increases for larger values of z_0.

This is consistent with the right panel of Fig. 4.15, revealing that z_0 exerts a large influence on the turbulent dissipation rate: Its value changes by almost an order of magnitude, depending on whether a smooth or an extremely rough surface with $z_0 = 0.01\,\text{m}$ is considered. For all following computations a value of $z_0 = 0.001\,\text{m}$ is chosen, since higher values are not justifiable by the sediment structure in Lake Alpnach. Fig. 4.15 illustrates that a lower value of z_0 or the assumption of a hydrodynamically smooth sediment leads to dissipation rates of the same order of magnitude. Differences in the computed dissipation rate for $z_0 = 0.001\,\text{m}$ and for a hydrodynamically smooth sediment, however, are hardly relevant if compared to the large scatter in the measurements (see Fig. 4.14).

Comparison of Different Two-Equation Models

For a direct comparison with the measured velocities (see Fig. 4.10), P in (4.10) was adjusted by hand for each seiche period to yield approximately the measured magnitude of the current speed between 3.5 and 4 cm/s. Model runs were conducted for seiche periods of 6, 12, and 24 hours in the unstratified case. The seiche period for Lake Alpnach during the measuring period was somewhere between the latter two values. A surface roughness length of $z = 10^{-3}$ m, appropriate for the conditions at the lake bottom was chosen (see above). Corresponding to the measurements (see Fig. 4.10), all records are plotted at the heights 114 cm, 184 cm and 254 cm, respectively.

To ascertain differences in performance of different model types in oscillating boundary layers, the two-equation models discussed in the preceeding chapters (except the Mellor-Yamada model) were compared. It turned out that velocity profiles computed from the k-ϵ model and different versions of the k-ω model were so similar that it was unnecessary to compare them in a plot. This was to be expected since turbulence only has a marginal influence on the velocity in the upper part of the boundary layer, and all models have been tuned to yield the same constants in the law-of-the-wall region of the lowest part of the boundary layer.

However, some differences were visible in the turbulent quantities as illustrated in Fig. 4.16 for a seiche period of 6 h: The k-ϵ model and the new WILCOX [294] k-ω model tend to perform quite similarly, but the old WILCOX [293] k-ω model exhibits a considerably
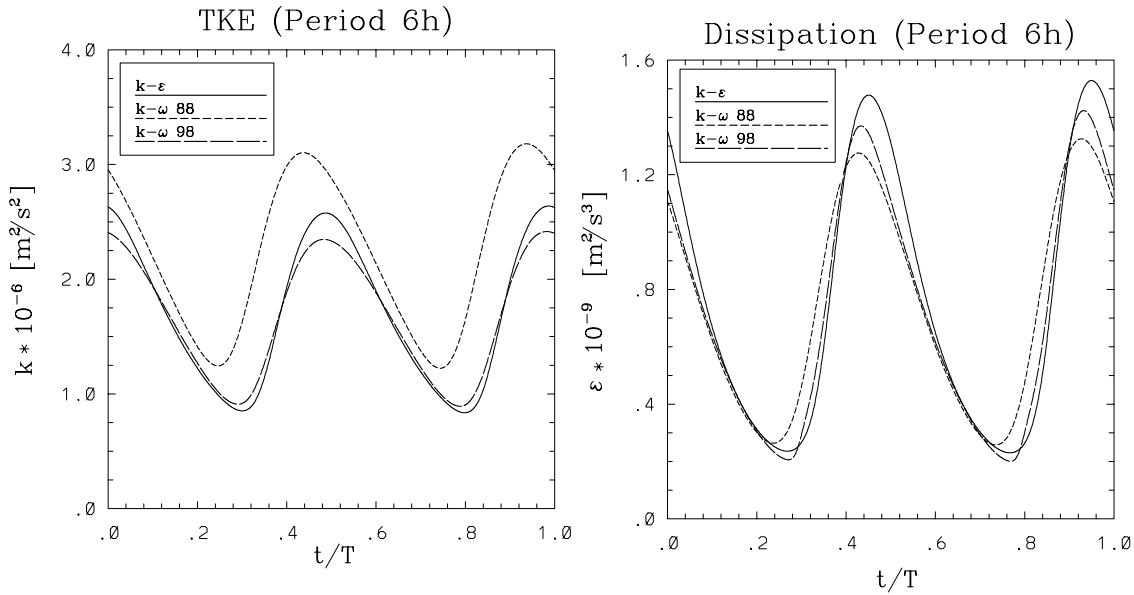
Figure 4.16: Turbulent kinetic energy, k, (left panel) and its rate of dissipation, ϵ, in an unstratified seiche-induced bottom boundary layer at $z = 2.54\,\mathrm{m}$ distance from the sediment as calculated by different models. The seiche period is $T = 6\,\mathrm{h}$, the amplitude of the exciting pressure-gradient is $\frac{1}{\rho}\frac{\partial p}{\partial x} = 1.4\cdot10^{-5}\ \mathrm{m/s^2}$, the bottom roughness length is $z_0 = 10^{-3}$ m.

different phase and amplitude behaviour of the turbulent kinetic energy, evident in the left panel of Fig. 4.16. In this case, a phase-shift of approximately $0.06T$ (i.e. approximately 20 minutes for $T = 6\,\mathrm{h}$) compared to the k-ϵ model can be observed. This fact also implies that the k-ω model predicts a smaller phase-shift between the velocity and the turbulent kinetic energy compared to the k-ϵ model. The same is true, though to a lesser extent, for the dissipation rate. Note, that it was already pointed out by BAUMERT AND RADACH [12] in a study of tidal flow, that the k-ϵ model predicts a too small phase-shift between the velocity and the turbulent kinetic energy, k, compared to measurements. Since the k-ω model predicts an even smaller phase-shift, it was rejected for the study of turbulent boundary layers and only the k-ϵ model was applied to the turbulent bottom boundary layer in Lake Alpnach.

Analysis of the Momentum Equation in the Unstratified Boundary Layer

As already remarked in the context of Fig. 4.15, the velocity time series are only slightly affected by the turbulent motion. Fig. 4.17, which compares the computed velocity records for the smallest and the largest seiche period, corroborates this fact. Both panels of this figure show a quasi-sinusoidal evolution of the velocity, similar to that predicted
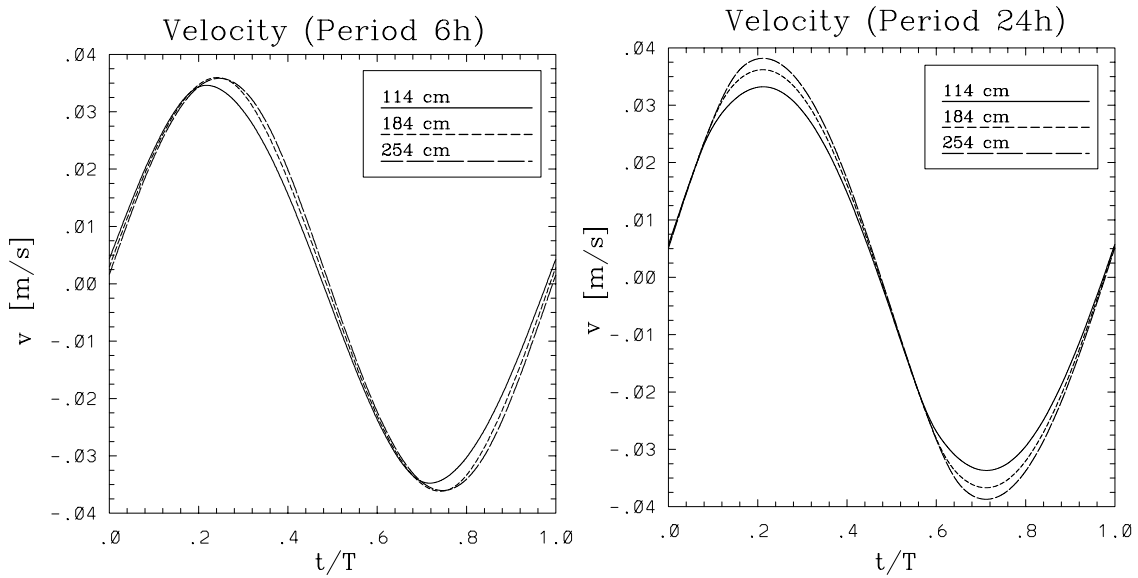
Figure 4.17: Velocity, v, in a seiche-induced bottom boundary layer as calculated by the k-ϵ model at different distances from the sediment. Seiche periods are $T = 6\,\mathrm{h}$ (left panel) and $T = 24\,\mathrm{h}$ (right panel). The amplitudes of the oscillating pressure-gradients are $\frac{1}{\rho}\frac{\partial p}{\partial x} = 1.4{\cdot}10^{-5}\,\mathrm{m/s^2}$ and $\frac{1}{\rho}\frac{\partial p}{\partial x} = 3{\cdot}10^{-6}\,\mathrm{m/s^2}$, respectively. The bottom roughness length is $z_0 = 10^{-3}\,\mathrm{m}$.

by (4.12). However, some systematic differences between individual records can be seen: Velocity records closer to the wall exhibit generally a slightly larger phase-shift, most obvious at $t = 0$ for the smaller seiche period on the left panel. Besides this, the phase-shift at all levels is larger for the longer seiche period displayed on the right panel. Since in this case the driving pressure-gradient is much smaller, the relative influence of turbulence will be larger. This is also consistent with the above argument, that turbulent friction should have an effect on the phase of the velocity and not only on its magnitude.

The square of the bottom friction velocity for all three seiche periods is illustrated in Fig. 4.18. In all cases, the records are remarkably equal, and the differences are likely to be due to the fact, that the magnitude of the driving pressure-gradient has been adjusted "by hand" for each seiche period to yield boundary layer velocities close to the measured ones. There is almost no phase-shift between records of different seiche periods. Since the friction velocity is computed from the velocity at the grid point closest to the sediment, this implies that there is also no phase-shift between the velocity records near the sediment for different seiche periods.

If the values of u_* computed from Fig. 4.18 are compared to the values obtained from the logarithmic curve fits in Fig. 4.13, it becomes evident, that the curve fits are likely
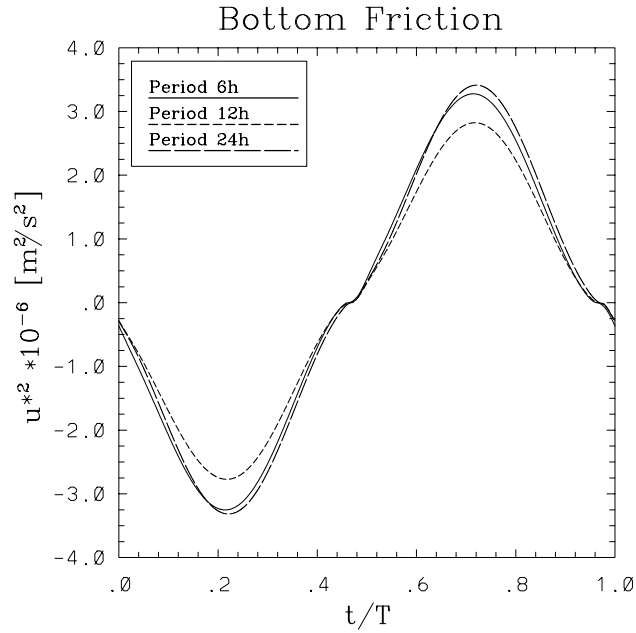
Figure 4.18:   Square of the friction velocity, $u_*^2 = \tau_w/\rho$, at the sediment as a function of dimensionless time for different seiche periods. Note, that the sign of the bottom stress, τ_w, has been retained in this plot.

to overestimate the true bottom stress by a factor of at least 2. The consequences with respect to the estimated dissipation values have already been discussed above.

Interesting insight in the dynamics of the bottom boundary layer can be gained by investigating the budget of the momentum equation. According to (4.11), the budget consists of a rate term, a pressure-gradient term, and the divergence[5] of the turbulent momentum flux. Since the pressure-gradient is prescribed according to (4.10) with $\varphi_0 = 0$, at $t = 0$ and $t = T/2$ there will be an almost perfect balance between the pressure-gradient and the rate term, which attain their respective maxima at approximately these times. The influence of the turbulent friction terms is negligible in this case.

Because of this fact, it is more interesting to study profiles of the budget at different times, e.g. at $t = T/4$, as displayed for the smallest and the largest seiche period in Fig. 4.19. Since the pressure-gradient is exactly zero at that time, the balance can be only between the rate term and the divergence of the turbulent momentum flux. Fig. 4.19 reveals that for both seiche periods the divergence of the turbulent transport extracts momentum from the lower part of the boundary layer and adds momentum to its upper part. As a direct consequence, fluid will be retarded in the lower part, whereas it will be

---

[5]The term "divergence" denotes here and in the following only the x-component of the divergence vector in the boundary layer approximation, i.e. $\partial\langle u'w'\rangle/\partial z$.

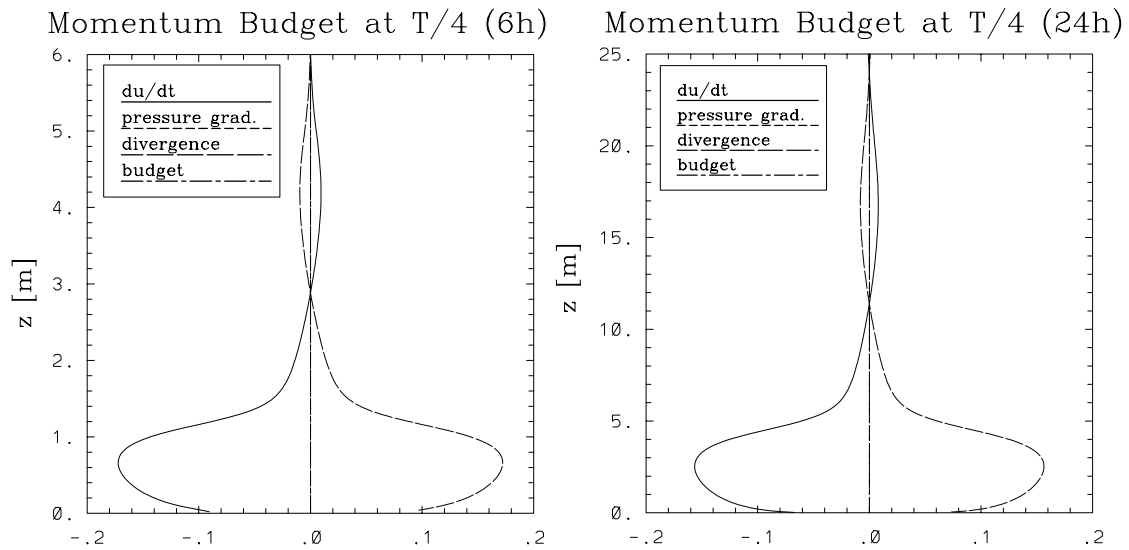Momentum Budget at T/4 (6h)   Momentum Budget at T/4 (24h)

Figure 4.19:   Profiles of the terms contributing to the budget of momentum at $t = T/4$. All terms have been made dimensionless with the maximum amplitude of the pressure-gradient, P. Left panel: Seiche period $T = 6\,\mathrm{h}$, right panel: Seiche period $T = 24\,\mathrm{h}$. "Budget" denotes the sum of all terms. Note the different scales!

accelerated in the upper part. It will be shown below, that this differential acceleration is the mechanism leading to the characteristic velocity maximum seen in both, the z-profiles of the measurements (Fig. 4.12) and the calculations (see Fig. 4.21 and Fig. 4.22 below).

Momentum Budget at 3/8T (6h)   Momentum Budget at 3/8T (24h)
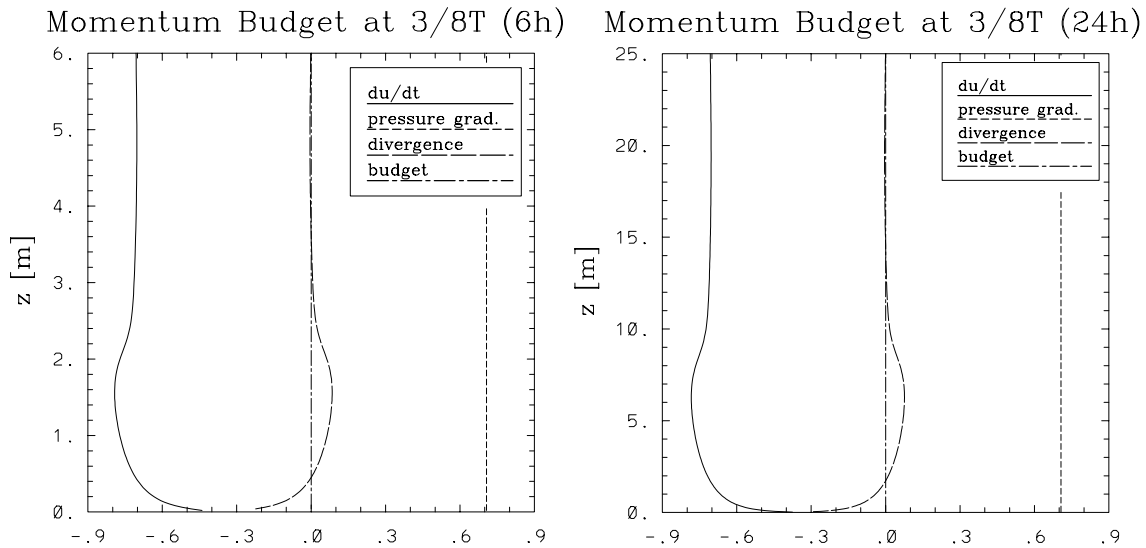
Figure 4.20:   As in Fig. 4.19, but now at $t = (3/8)T$. Note the different scales!

The budget at $t = (3/8)T$ is representative for a situation in which all terms in (4.11) can contribute: The rate term, since the fluid is retarded at all levels, the pressure-gradient term, which has an intermediate value of $P/\sqrt{2}$ at that time, and the turbulent friction

term. It can be seen from Fig. 4.20 that in this case the dominant balance is between the rate term and the pressure-gradient. The divergence term contributes only in the lowest part of the turbulent layer, where it leads to a relative retardation of the fluid. These results apply to both, the smallest and the largest seiche period.

The net effect of differential acceleration in turbulent boundary layers is illustrated in Fig. 4.21 and in the left panel of Fig. 4.22 that display velocity profiles at the approximate time of maximum current speed: *For all seiche periods the velocity exhibits a characteristic maximum.* This result should be compared to the measured profiles of Fig. 4.12, which exhibit a very similar velocity maximum at the time of maximum current speed. It is believed that the above arguments provide an explanation to this phenomenon.
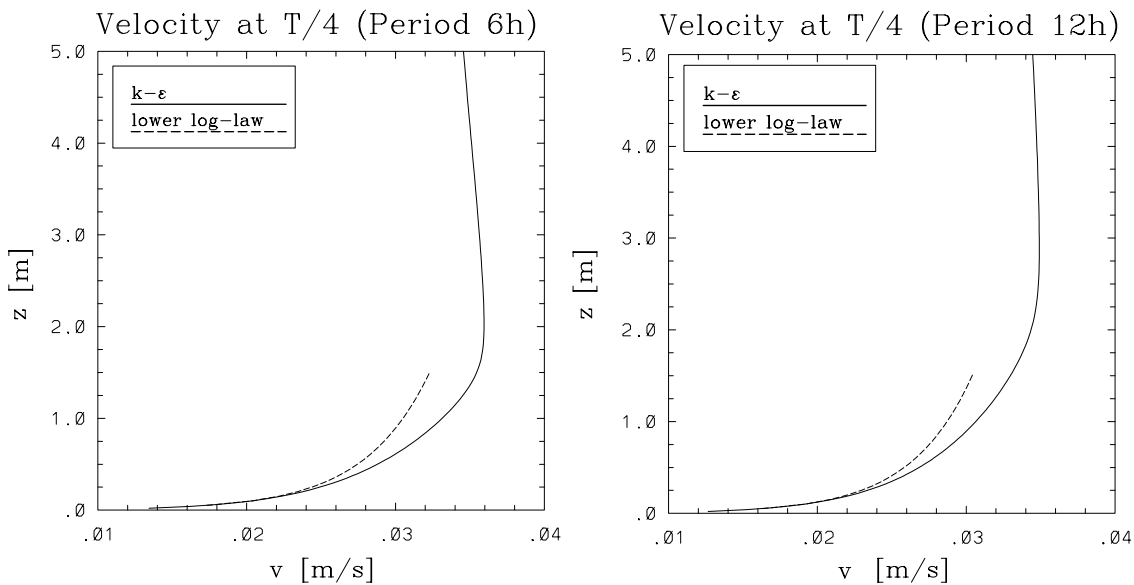
Figure 4.21:   Profiles of the velocity, v, at $t = T/4$ for a seiche period of $T = 6\,\mathrm{h}$ (left panel) and $T = 12\,\mathrm{h}$ (right panel). The corresponding logarithmic part of the law-of-the-wall is also indicated.

Fig. 4.21 and the left panel of Fig. 4.22 also include the logarithmic velocity profiles according to the law-of-the-wall (derived from the known values of u_*, z_0, and κ.) *Clearly, these profiles are only a valid approximation in the lowest part of the oscillating boundary layer.*

The following experiment deserves particular attention: If the lowest $0.5\,\mathrm{m}$ of the computed velocity profiles from Fig. 4.21 are disregarded, and the rest of the profiles up the velocity maximum is interpolated by simple logarithmic functions, "perfect" curve fits, shown on the right panel of Fig. 4.22 can be obtained. With these "spurious" fits, how-

Figure 4.22:   Left panel: Same as in Fig. 4.21, but now for a seiche period of $T = 24\,h$. Right panel: Velocity profiles from Fig. 4.21 , but now displayed together with "spurious" logarithmic fits (see text).

ever, *the friction velocity, u_*, is overestimated by a factor of about 1.5, and the bottom roughness length, z_0, by a factor of 5 compared to the true valu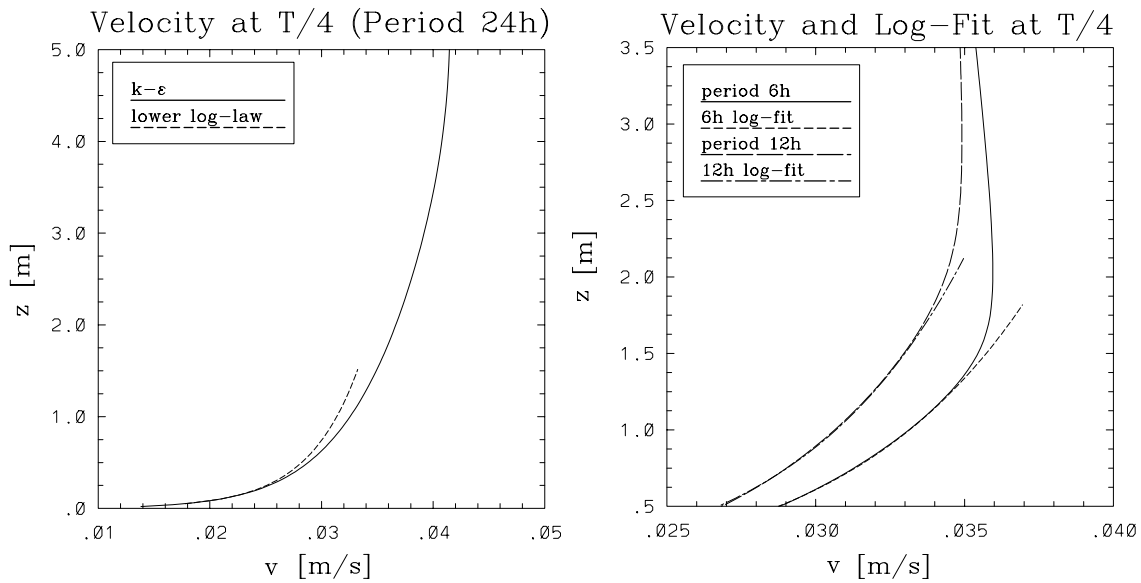es.* It is believed that this argument, at least partly, also explains the "perfect" logarithmic fit of the measured velocity profiles shown in Fig. 4.12 (in which the lowest $0.5\,m$ have been also ignored) on the one hand, and the poor quality of the "fit parameters" u_* and z_0 in Fig. 4.13 on the other hand. Theses errors lead to an overestimation of the rate of dissipation of more than an order of magnitude (see Fig. 4.14).

Analysis of the Turbulent Quantities in the Unstratified Boundary Layer

Several interesting features can be observed from the time series of the turbulent kinetic energy and its rate of dissipation, shown in Fig. 4.23–Fig. 4.25. First, it is obvious that both turbulent quantities exhibit a phase-lag with respect to the velocity records shown in earlier figures. For both, k and ϵ, this phase-lag becomes gradually smaller for all seiche periods, if the sediment is approached. Indeed, this behaviour had to be expected, since very close to the sediment the logarithmic law-of-the-wall relations apply, which do not predict any phase-lag between the velocity and turbulent quantities. For large seiche periods (see Fig. 4.25) the relative phase-shift of turbulent quantities at different heights above the sediment is smaller than for small seiche periods.
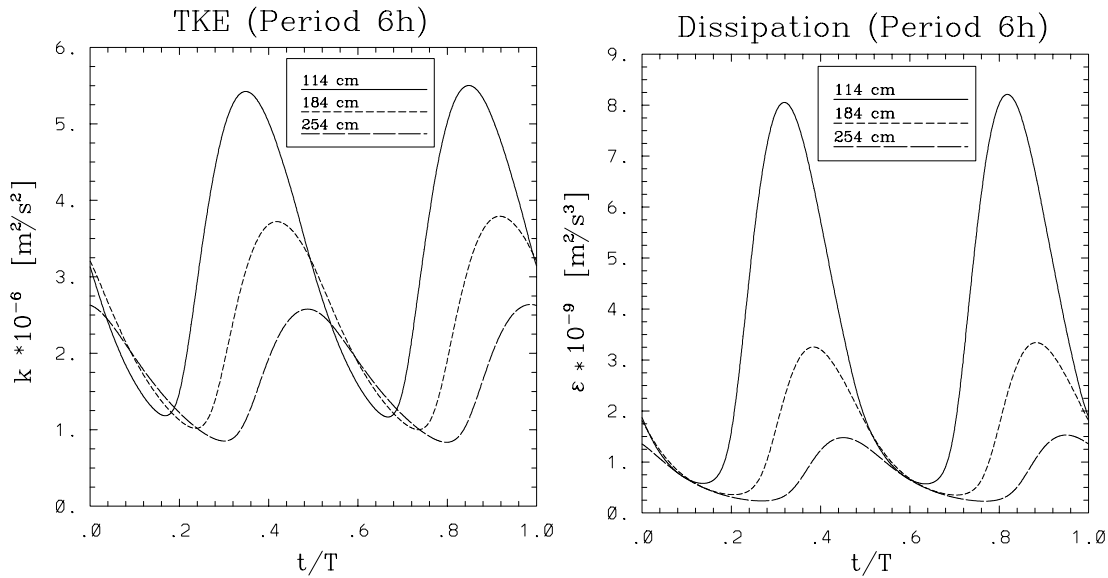
Figure 4.23:   Time series of the turbulent kinetic energy, k, (left panel) and its rate of dissipation, ϵ, (right panel) for one complete seiche cycle at different heights above the sediment. The seiche period is $T = 6\,\mathrm{h}$.

For the turbulent kinetic energy, k, computed at different levels above the sediment, not only the relative phase-lag becomes smaller for larger seiche periods, but also the differences in amplitude of k. However, even for an infinite seiche period, k will not become equal at all levels as in the logarithmic boundary layer. This is simply due to the fact that in a steady-state pressure-driven boundary layer, u_* and hence k are linear functions of z (as, e.g., in Fig. 4.3).

For large seiche periods, the phase-lag with respect to the velocity (measured in units of T) is smaller than for small periods. Since large periods are thought to be closer to a steady state current with no phase-lag at all, this behaviour is not surprising. Tab. 4.2 gives the absolute values of the phase-lag at different heights and for different seiche periods. From this table a phase-lag of about 1 h for the dissipation rate at a height of

distance	k (6 h)	ϵ (6 h)	k (24 h)	ϵ (24 h)
114 cm	0.6h	0.5h	1.2h	1.0h
254 cm	1.7h	1.4h	2.2h	1.7h

Table 4.2:   Approximate phase-shift between turbulent quantities and the velocity at several heights above the sediment and for the seiche periods $T = 6\,\mathrm{h}$ and $T = 24\,\mathrm{h}$

approximately 1 m above the sediment and for a seiche period of 24 h can be deduced.
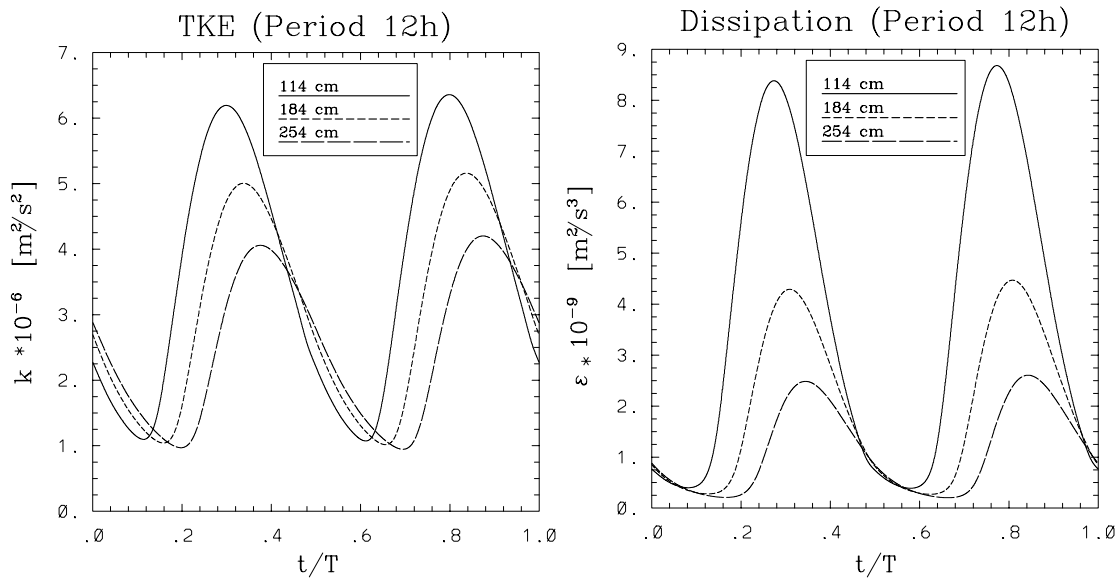
Figure 4.24: Same as Fig. 4.23, but now for a seiche period of $T = 12\,\text{h}$.

This phase-lag can directly be compared to the phase-lag of about $2\,\text{h}$ indicated by the microstructure measurements in Lake Alpnach (displayed in Fig. 4.14). Even though the data are somewhat scattered and the phase-lag cannot be determined with high accuracy, the phase-lag predicted by the k-ϵ model is apparently somewhat too small. BAUMERT AND RADACH [12] compared their k-ϵ model to the measured phase-lag between the velocity and the turbulent kinetic energy in a tidal flow and came to a similar conclusion. It should be noted, that the k-ω model would have predicted an even smaller phase-lag.

Fig. 4.26 displays profiles of all terms contributing to the budget of k for the smallest and the largest seiche period at approximately the time of maximum current speed. The scale was adjusted to resolve the small contributions of the rate term and the divergence of the turbulent transport of k. Close to the bottom there is a clear balance between shear production and dissipation of k, and one of the necessary conditions for the existence of a logarithmic part of the law-of-the-wall is satisfied.

TKE (Period 24h)

Dissipation (Period 24h)
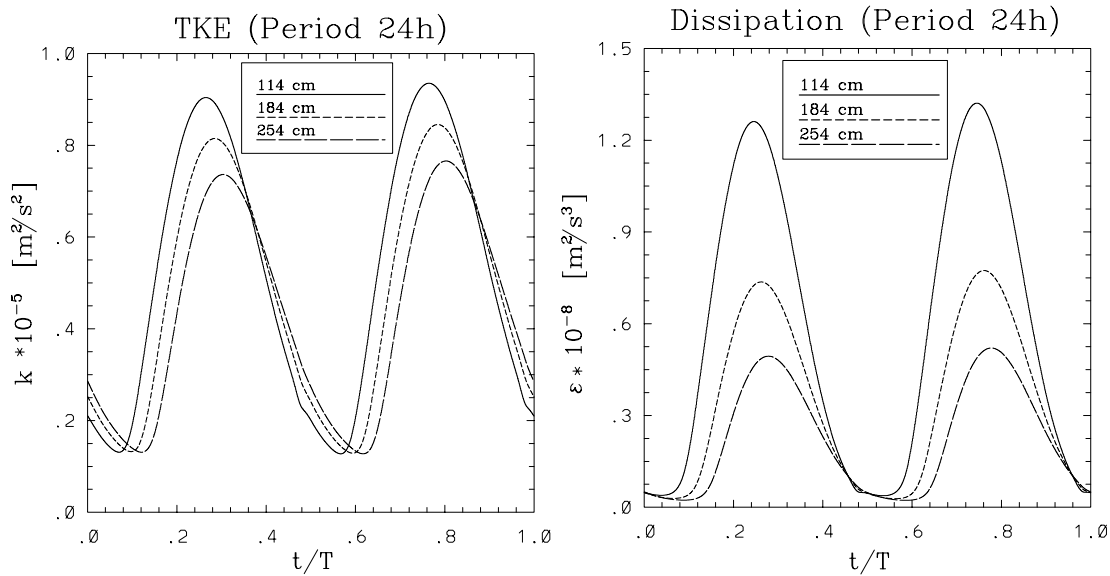
Figure 4.25:   Same as Fig. 4.23, but now for a seiche period of $T = 24\,\text{h}$.

TKE Budget (Period 6h)

TKE Budget (Period 24h)
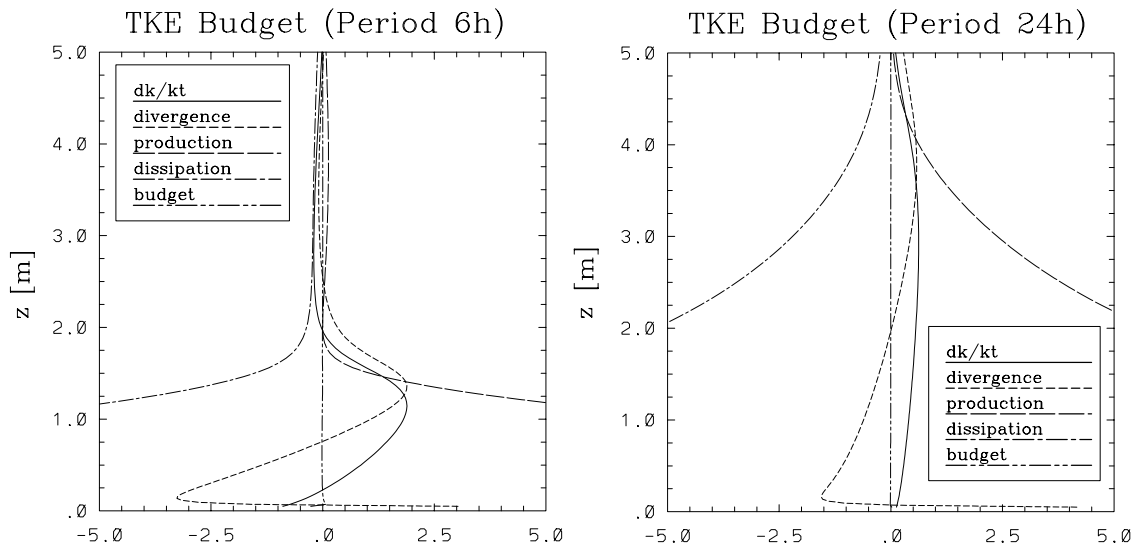
Figure 4.26:   Non-dimensional budget of the turbulent kinetic energy, k, as a function of distance from the sediment, z, at $t = T/4$. Seiche periods are $T = 6\,\text{h}$ (left panel), $T = 24\,\text{h}$ (right panel). "Budget" denotes the sum of all terms.

However, above this "shear layer" of approximately $1\,\text{m}$ thickness for $T = 6\,\text{h}$ and $4\,\text{m}$ thickness for $T = 24\,\text{h}$, the rate and turbulent transport terms become important and may even dominate the budget at some levels. Profiles of the dissipation rate at the time of maximum current speed are given in Fig. 4.27. *As with the velocity profiles displayed above, the logarithmic law-of-the-wall is seen to be a reasonable approximation up to at*
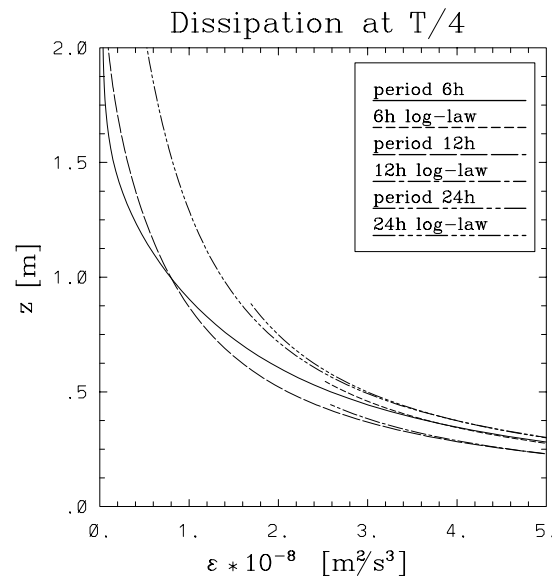
Figure 4.27:   Rate of dissipation, ϵ, as a function of distance from the bottom, z, for different seiche periods T. Also displayed are the respective logarithmic law-of-the-wall relations $\epsilon = u_*^3/[\kappa(z + z_0)]$.

most 1 m above the sediment for all periods.

4.2.3   Modelling the Stratified Seiche-Induced Boundary Layer

It is known from numerous publications on Lake Alpnach (see above) that during summer time the lower part of the hypolimnion of this lake is stratified with a buoyancy frequency somewhat larger than $N^2 \approx 10^{-5} \text{s}^{-2}$. GLOOR ET AL. [90] demonstrated that most of the energy contained in the internal seiching motion is dissipated at the bottom, but a small part is converted to potential energy used to mix the water within a couple of meters distance from the sediment. These authors also pointed out that it is difficult to obtain an exact value of the thickness of this well mixed boundary layer, since the seiching motion convects water from regions of the boundary layer where the thickness may be considerably different.

To assess the height of the bottom boundary layer induced by only *local* mixing, the k-ϵ model together with the ASM of LUYTEN ET AL. [156], described in previous chapters, was applied to the bottom boundary layer of Lake Alpnach. This model has already been shown to compute a mixing layer depth in very good agreement with experimental data for an entrainment situation with constant friction velocity, u_*, provided that the steady-state Richardson number is tuned to $Ri_{st} = 0.25$ (see Section 4.1.3). Thus, it

seems fair to expect that this model also provides a reasonable prediction of the height of the oscillating bottom boundary layer.

Bottom Mixed Layer Height
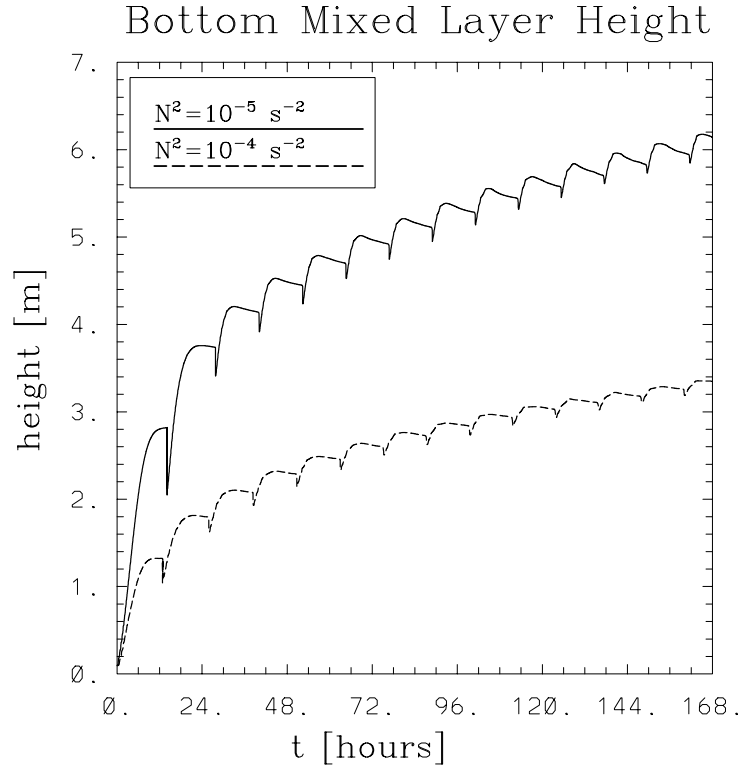
Figure 4.28:   Height of the bottom mixing layer eroded by a seiche bottom current for two different linear initial stratifications as indicated. It is assumed that initially no bottom mixing layer exists. Seiche Period $T = 24h$, amplitude of the driving pressure-gradient is $\frac{1}{\rho}\frac{\partial p}{\partial x} = 3 \cdot 10^{-6}$ m/s^2. Computed by the k-ϵ model and the ASM of LUYTEN ET AL. [156]. Bottom roughness is $z_0 = 10^{-3}$ m.

To conform to the conditions in Lake Alpnach, the model was run for a seiche period of 24 h driven by a periodic pressure-gradient as in (4.10). The maximum current speed in the boundary layer was adjusted to the measured values of 3.5-4.0 cm/s. The computed mixed layer heights for initial stratifications with $N^2 = 10^{-5}$s^{-2} and $N^2 = 10^{-4}$s^{-2} are displayed in Fig. 4.28. The actual value of the buoyancy frequency of most measurements was between these two values, and hence this figure gives upper and lower bounds for the expected height of the mixing layer[6]. Fig. 4.28 reveals that, after one week of seiching motion, the model predicts boundary layer heights of approximately 3.4 m for $N^2 = 10^{-4}$s^{-2} and 6.2 m for $N^2 = 10^{-5}$s^{-2}. These values are in good agreement with

---

[6]The height of the mixing layer is defined as the distance from the sediment above which the criterion $N^2 < 0.5N_0^2$ is violated. Note, that this height does not exactly coincide with the height reached by the turbulent front, since turbulence needs some time to reduce the initial stratification N_0^2 in the entrainment region to $0.5N_0^2$.

the measured height of 4-5 m (see GLOOR ET AL. [90]). It is seen that the bottom layer is eroded in two steps per seiche period, each followed by a small collapse. Note, that this collapse does not coincide exactly with the time of flow reversal. Rather, it takes place when the turbulent quantities close to the entrainment region, which slightly lag the velocity field, attain their minimum values. This is consistent with the perception that mixing layer entrainment should be determined by the turbulent quantities in the entrainment region.

It is also apparent from Fig. 4.28 that, even though an equilibrium height is not reached after one week, the largest part of the bottom layer is eroded after a couple of days. This clearly contradicts the current believe that the erosion of the well mixed bottom layer in Lake Alpnach takes several months (see GLOOR ET AL. [91, 89]). These authors predicted the boundary layer height with a formula of the form

$$h = c_{\mathrm{KP}} u_* (t/N_0^2)^{\frac{1}{3}} \,, \tag{4.15}$$

with the dimensionless constant c_{KP}. This formula coincides precisely with the formula derived by KATO AND PHILLIPS [137] to describe their mixing layer entrainment experiments. However, the model constant in (4.15) used by GLOOR ET AL. [91, 89] is $c_{\mathrm{KP}} = 1.145$, only approximately half of the value $c_{\mathrm{KP}} = 2.466$ suggested originally by KATO AND PHILLIPS [137].

There are a couple of problems with (4.15) making it seem plausible that GLOOR ET AL. [91, 89] arrived at the wrong conclusion:

- (4.15) (and also the improved version (4.5) introduced in Section 4.1.3) were originally intended to describe mixing layer deepening by a *constant* surface stress without pressure-gradient. Most of the potential energy needed for entrainment in such experiments is extracted from the strong velocity shear in the entrainment region. Quite contrary, in the entrainment region of turbulent bottom layers there is almost no velocity shear. Energy for the entrainment must be obtained from turbulent transport or from the locally stored turbulent kinetic energy in the case of decaying turbulence.

- There is no physically sound argument for the applicability of both formulae to *oscillating* boundary layers driven by a pressure-gradient, if merely the friction velocity is replaced by some mean value as in GLOOR ET AL. [91, 89]. In fact, it can be shown that, e.g., formula (4.5) then predicts a boundary layer height more than three times larger than that of Fig. 4.28. (Recall that the same formula coincides almost perfectly with the model predictions for constant u_* as in Fig. 4.5.)

- The average value of u_* used by GLOOR ET AL. [91, 89] is at least twice too small, since it was based on a too small value of the drag coefficient $c_{1m} = 1.5 \cdot 10^{-3}$. (Values following from the logarithmic law-of-the-wall would be $c_{1m} = 2.1 \cdot 10^{-3}$ for hydrodynamically smooth walls and $c_{1m} = 3.5 \cdot 10^{-3}$ for a roughness length of $z_0 = 10^{-3}$ m.) Thus, even if (4.15) were correct, these authors would not have obtained the right boundary layer height.

All results from the preceeding part of this section were derived for unstratified oscillating boundary layers. Nevertheless, many of the conclusions drawn can be directly applied to initially stratified boundary layers after a well mixed layer has been eroded. This is demonstrated in Fig. 4.29, Fig. 4.30, and Fig. 4.31 which display time series of the rate of dissipation at different heights above the sediment for the case of no stratification, weak stratification ($N^2 = 10^{-5}$s^{-2}), and strong stratification ($N^2 = 10^{-4}$s^{-2}), respectively.

These figures illustrate that after the onset of the fluid motion a certain entrainment time is required for different layers to become turbulent. It can be most clearly seen from the dissipation rate time series at 2.5 m height above the sediment that the required time strongly depends on the initial stratification: The turbulent front reaches this level after approximately 4 hours in the unstratified case, after 5 hours in the weakly stratified case, and after more than 30 hours in the strongly stratified case. After these times the boundary layer heights given in Fig. 4.28 are approximately reached (in fact, they are somewhat larger now, because different criteria have been used to determine the boundary layer height.)

After the turbulent front has reached a certain level in the stratified cases, it takes a few seiche periods before the time series of this level becomes comparable to its unstratified counterpart. However, due to the presence of a small buoyancy flux in the stratified cases, phase and amplitude do not completely coincide. Note, that the maximum rate of dissipation in the weakly stratified case (Fig. 4.30) is larger than in the stratified case. This apparently paradoxical behaviour can be explained by the fact that the third term on the left hand side of (3.13)$_2$ makes a positive contribution to the budget of ϵ since both, the buoyancy production, G, and the model coefficient, $c_{\epsilon 3}$ are negative.

The above illustration indicates, that even though the stratified cases will always be influenced by a small buoyancy flux until the boundary layer height has reached its equilibrium value, its contribution does not overly affect the results compared to the unstratified boundary layer. The maximum value of the rate of dissipation in the stratified boundary layer is somewhat larger than 10^{-8}m^{2}s^{-3}. Recall from the first part of this section, that it

Dissipation (unstratified)
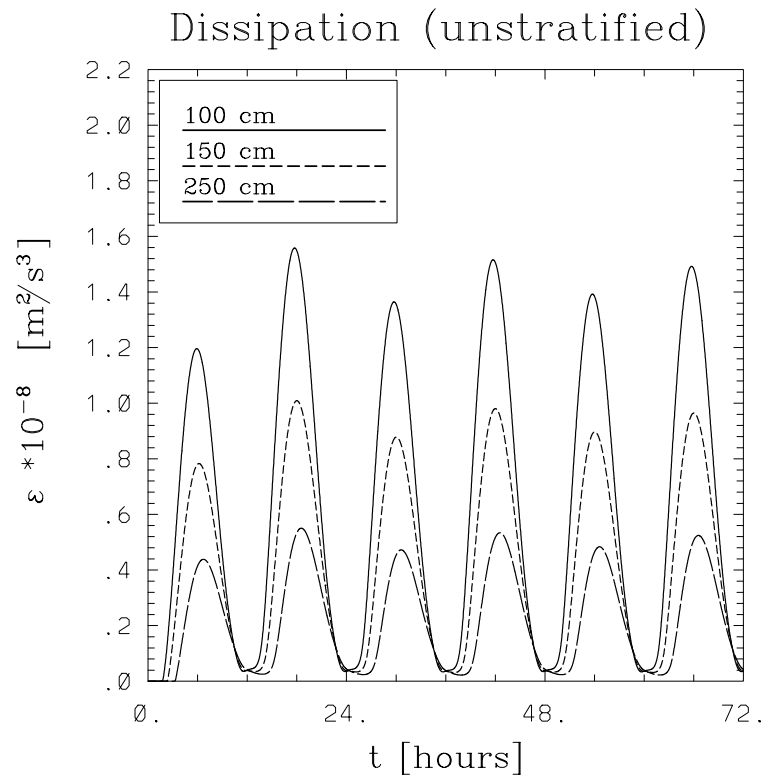
Figure 4.29: Rate of turbulent dissipation at different heights and without stratification. For clarity, only the first three days of entrainment are displayed.

would have been about 50% smaller for a hydrodynamically smooth sediment surface. It is satisfying to see that a dissipation rate of this order of magnitude is in good agreement with the microstructure measurements of the EAWAG (see the running mean value in Fig. 4.14). In contrast to that, all estimates based on the logarithmic curve fits are at least an order of magnitude too large.

Summarising, the following results have been obtained in this section:

- The first comparison of measured time series of the dissipation rate in an oscillating boundary layer in a lake and results from two-equation models has been performed.

- Satisfactory agreement between the measured and the computed magnitude of the dissipation rate could be achieved.

- The phase-lag of about 2 hours between the bottom friction velocity and the dissipation rate 1m above the sediment could only be reproduced partly by the two-equation models. The phase-lag predicted by the k-ω model is smaller compared to the k-ϵ model.
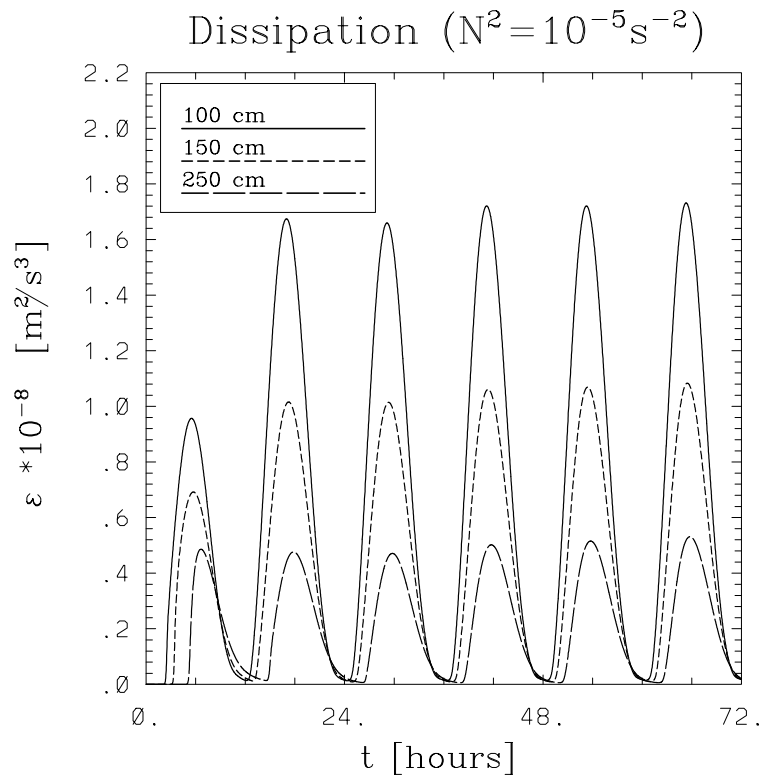
Figure 4.30:   Same as Fig. 4.29, but now with initial stratification $N^2 = 10^{-5}$ s^{-2}.

- The characteristic maximum in the current speed at a certain level above the sediment, seen in the measurements, was reproduced by the model. It could be shown that the maximum occurs because of differential acceleration caused by different values of the divergence of the turbulent momentum flux at different levels.

- It was shown that logarithmic curve fits are no appropriate method to derive values for the friction velocity and the rate of dissipation in pressure-driven dynamical boundary layers and lead to a massive overestimation of the rate of dissipation.

To arrive at a more conclusive statement about phase-shifts in bottom boundary layers of lakes, more detailed microstructure measurements are required. Ideally, they should be accompanied by continuous measurements of the turbulent kinetic energy, a quantity that was predicted in this section to have an even larger phase-lag than the dissipation rate. Future work will examine whether a low Reynolds number version of the models used here would predict an increased phase-lag between the velocity and the turbulent quantities. Also, the phase differences in the turbulent fields induced by the small buoyancy flux in initially stratified boundary layers need a closer investigation.
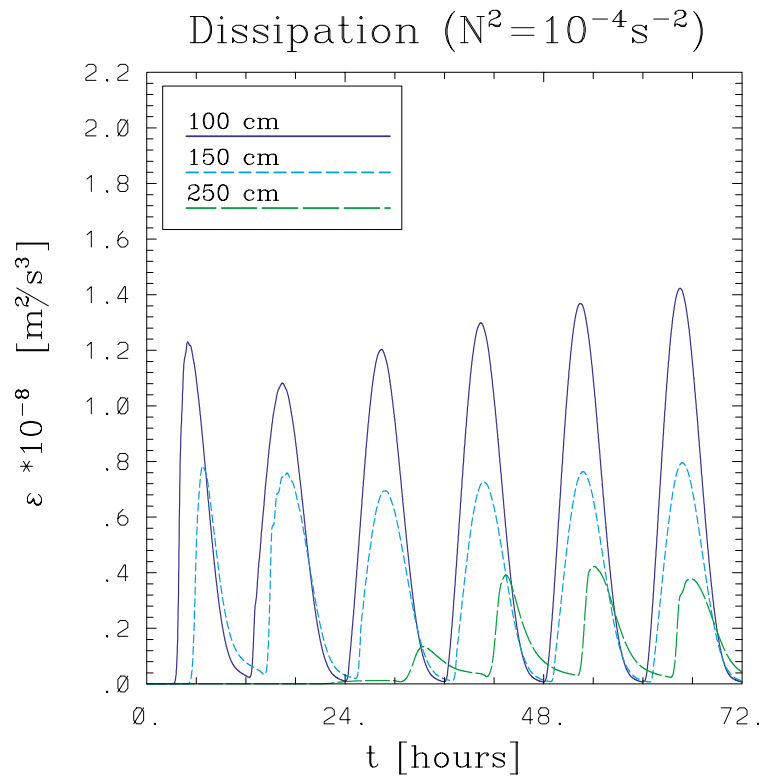
Figure 4.31: Same as Fig. 4.30, but now with initial stratification $N^2 = 10^{-4}$ s^{-2}.

4.3 Physical-Biological Coupling

4.3.1 Introduction

Ecological modelling is a rapidly growing interdisciplinary scientific field. This is particularly evident in limnology, the science of inland waters[7]. Because of their comparably isolated character as ecosystems and the relative simplicity of their planktonic organisms, lakes have been described as "little theatres where (...) the interactions among organisms and between organisms and their environment could be studied more easily than anywhere else" (LAMPERT AND SOMMER [144]). It is thus not surprising that many successful ecological models have been applied to limnological problems. Above this, many of the fundamental concepts of modern ecology can be traced back to limnology.

Beyond its role as a scientific discipline, limnology also provides a scientific basis for

---

[7]In this section, moderate use of the standard limnological terminology is made. Readers not familiar with this topic are referred to the first pages of any limnological text book (e.g. WETZEL [292], SCHWOERBEL [221]).

the management of lakes and rivers. Ecological models, in this context better known under names like "water quality models" or "coupled physical-biological models" were used successfully to gain a deeper understanding of the eutrophication problem of the seventies and eighties of the last century. Even though the trophic state of many lakes has recovered since then, at least in the developed countries, there is still an urgent need for a more quantitative environmental management to be able to solve the steadily increasing pollution problems.

For a precise prediction of the most important parameters describing the quality of water in lakes and reservoirs, a vast number of different model types has been suggested. Usually, a general distinction is made between so-called inductive (or empirical) and deductive (or theoretical) models, even though in environmental sciences their distinction appears to be blurred. The relative merits of both methods with respect to a limnological problem are discussed in an interesting conversation between LIVINGSTONE AND IMBODEN [152, 153] and MOLOT [174]. Here, the deductive approach in the spirit of LIVINGSTONE AND IMBODEN [152] is preferred, since it seemed best suited to the object of study: An investigation of the oxygen budget of Lake Ammer, a medium-sized Alpine lake in Southern Germany.

However, even if one has decided to concentrate on the deductive approach, the available amount of literature in limnology and oceanography is overwhelming. In a classical style, FRANKS [78] reviewed some recently published coupled physical-biological models applied in oceanography, whereas JØRGENSEN [133] discussed the state-of-the-art of ecological modelling in limnology from a more methodological point of view. From both reviews it is evident that there are many different types of models and many more or less reasonable ways to group them. Here, the hydrodynamical component of the models is emphasized. It is plausible then to discern, according to the introduction of Chapter 3, between integrated and differential models[8]. An example of the former type, applied to limnological problems, is the relatively simple model of FRANKE ET AL. [77], who used a physical component of the Kraus-Turner type to simulate an environment for competing phytoplankton species under grazing pressure. Another, more elaborate, model of the same type is the multi-component biogeochemical model of HAMILTON AND SCHLADOW [97, 216], which is based on the well-known hydrodynamical bulk model DYRESM (see 3.2).

From the experience gained with an integral method (see FRANKE ET AL. [77]), it must be concluded that there are a number of undesirable features restricting the applicability of integrated models to physically-biologically coupled systems:

---

[8]Only horizontally averaged, one-dimensional models are investigated.

- FRANKE ET AL. [77] showed that integral methods may exhibit strong daily oscillations of the predicted thermocline depth. Even though, on a seasonal scale, the thermocline depth coincides to a good degree with the measured values, this behaviour can lead to an un-precise simulation of the biological parameters.

- By their nature, integral models do not provide an epilimnetic exchange coefficient and cannot resolve the spatial structure of epilimnetic parameters. This limits their performance in the modelling of biogeochemical processes, since, as pointed out by FANG AND STEFAN [71], "both surface gas transfer and diffusion depend on turbulence near the water surface", indicating that a detailed knowledge of the turbulent quantities near the surface is of great importance for a precise description of the gas budget.

- The influence of turbulence on small aquatic organisms is an evolving field in the study of physical and biological interactions (see DENMAN AND GARGETT [61]). Only turbulence models, that resolve the turbulent fields will be able to provide the parameters necessary to model such interactions.

There is also a number of coupled models that are based on a differential description of hydrodynamical parameters. Most of them parameterize the vertical diffusivities, needed in such models, by primitive zeroth-order closure models, often implemented in form of simple Richardson number dependent formulations. Oceanographical examples are the multi-component food web model of a Norwegian fjord of AKSNES AND LIE [3] and the model of TUSSEAU ET AL. [275] for the Mediterranean Sea. MOISAN AND HOFFMANN [172] derived the physical variables of their elaborate one-dimensional physical-bio-optical model of the Californian coastal transition zone from a three-dimensional model calculation. However, their turbulence parameterization reduces to the most simple form of constant (in space and time) turbulent diffusivities. The physical component of the three-dimensional version of this model (MOISAN ET AL. [173]) is described and tested in detail with respect to its applicability to lakes in UMLAUF ET AL. [283].

Also, a number of coupled models of the differential type, applied to limnological problems, has been published: RILEY AND STEFAN [202], STEFAN AND FANG [243], and CULBERSON AND PIEDRAHITA [55], e.g., presented coupled models intended primarily to study lake eutrophication and control strategies. Only very few three-dimensional models, usable as management tools for lakes and reservoirs, have been published, e.g., by RAJAR AND CETINA [197] and by SOYUPAK ET AL. [231] (the latter authors coupled a three-dimensional biological model with a vertically integrated two-dimensional physical model).

Apparently, in limnology only few modellers coupled their biological algorithms to Reynolds closure schemes as described in Chapters 1 and 2, an exception being, e.g., BLUMBERG AND DI TORO [17], who computed the turbulent diffusivities for their 15 component biological model of Lake Erie with a level 2.5 model of the MELLOR AND YAMADA [169] hierarchy.

The physical component of the model described in this section is based on a k-ϵ two-equation model with the ASM of GIBSON AND LAUNDER[9] [87, 88] (see Chapters 1 and 2). A one-dimensional (vertical) representation was chosen, since due to the effect of gravity, the physical and biological parameters are structured predominantly in this direction. Unfortunately, many other interesting features, including most wave types or the effects of horizontal advection, cannot be directly described by such models.

The price, however, for the greater capabilities of three-dimensional modelling is high. Using the results of UMLAUF ET AL. [283], it can be shown that the ratio of the computation times for three- compared to one-dimensional modelling is roughly 10^3–10^4. Even though a few successful simulations of enclosed or semi-enclosed basins of medium size over annual cycles with three-dimensional hydrodynamical models have been recently reported (AHSAN AND BLUMBERG [2], BLUMBERG ET AL. [15]), the computational effort must be considered very demanding: On a present-day personal computer[10] the overall computation time for a one-year's three-dimensional hydrodynamical simulation is of the order of days or even weeks, but for a one-dimensional simulation only of the order of tens of minutes. Clearly, a detailed parameter adjustment, crucial in physical-biological coupled modelling, is extremely costly in the three-dimensional case. For this reason and for the fact that three-dimensional hydrodynamical and biological data and a precise description of the two-dimensional wind field are hardly ever available for calibrating and verifying these models, one-dimensional modelling can still be considered an appropriate and convincing approach for the prediction of water quality.

The biological component coupled turbulence-oxygen model introduced here solves the one-dimensional transport equation for oxygen, adopting the vertical diffusivities and the temperature profiles from the two-equation model. The biomass of photosynthetic algae is represented by measured values of the chlorophyll-a concentration. This is the main difference to most existing models that derive the biomass from a dynamical system of conservation equations for different species and nutrients. Surface re-aeration is repre-

---

[9]Note, that here the turbulent diffusivity of momentum was computed from the standard k-ϵ model, and only the turbulent Prandtl number was derived from the ASM to take into account the influence of stratification.

[10]For example on a 1 GHz Pentium III processor.

sented as a surface flux term and time and depth depending source and sink terms for photosynthetic production, respiration of algae, biochemical oxygen demand of bacterial decay (S_{BOD}), and sedimentary oxygen demand (S_{SOD}) are included. Some of the model results have already been described in JÖHNK [130], JÖHNK AND UMLAUF [129], and UMLAUF AND JÖHNK [281].

4.3.2 The Model Equations

The evolution of all variables will be described by one-dimensional vertical diffusion equations with time and space dependent vertical diffusivities. In physical limnology, these equations have been formulated for a variable φ either in a horizontally integrated form, depending on the area A at depth z as in

$$\frac{\partial \varphi}{\partial t} = \frac{1}{A} \frac{\partial}{\partial z} \left(A \left(\nu^\varphi + \nu_t^\varphi \right) \frac{\partial \varphi}{\partial z} \right) + P_\varphi \,, \tag{4.16}$$

or for a horizontally infinite fluid as in

$$\frac{\partial \varphi}{\partial t} = \frac{\partial}{\partial z} \left(\left(\nu^\varphi + \nu_t^\varphi \right) \frac{\partial \varphi}{\partial z} \right) + P_\varphi \,, \tag{4.17}$$

where ν^φ and ν_t^φ are the molecular and turbulent vertical diffusivities of the variable φ, respectively. P_φ is the production of the variable φ, which in the case of (4.16) also includes a contribution from the flux of φ through the lateral boundaries.

Whether variables are represented either with or without horizontal integration of their transport equations depends on the size and the geometry of the lake, and on the time-scale of the mixing processes considered[11]. Note, however, that if no reasonable parameterization of the boundary fluxes of φ as production terms can be found, (4.16) cannot be used in a meaningful way.

For computations on a seasonal time-scale, evidence was found for an influence of the boundary fluxes for the balance of heat

$$\frac{\partial \theta}{\partial t} = \frac{1}{A} \frac{\partial}{\partial z} \left(A(\nu^\theta + \nu_t^\theta) \frac{\partial \theta}{\partial z} \right) + \frac{1}{\rho_0 c_v} P_\theta \,, \tag{4.18}$$

and for the oxygen budget

$$\frac{\partial O}{\partial t} = \frac{1}{A} \frac{\partial}{\partial z} \left(A(\nu^O + \nu_t^\theta) \frac{\partial O}{\partial z} \right) + P_O \,, \tag{4.19}$$

---

[11]For studies of the range of applicability of either type of equation in limnological applications, see TZUR [276], IMBODEN AND EMERSON [121].

where O denotes the concentration of oxygen in the water column. The turbulent diffu-
sivity of a passive tracer is assumed to be equal to the turbulent diffusivity of heat, ν_t^θ,
as in (4.19). Parameterizations of the fluxes of heat and oxygen through the boundary as
production terms are given in (4.26) and (4.45) below.

The parameterization of the production term in (4.17) for $\varphi = u, v$, i.e. for the momentum
equation in horizontally averaged one-dimensional models is an intricate problem, since
two important questions arise that have no simple answer: First, what role do the Coriolis
terms in one-dimensional models of enclosed and stratified basins of medium[12] size play?
Second, how can the bottom momentum flux be parameterized in such models?

The first question is of no particular relevance in one-dimensional models of the ocean and
of very large lakes. In these cases, the Coriolis terms give rise to inertial waves, a well-
known and frequently observed phenomenon in large stratified and unstratified basins.
Even though inertial waves can also be observed in unstratified basins of medium size,
they are neither measured nor computed during summer stratification (for the situation
in Lake Ammer see UMLAUF ET AL. [277, 283]). Basin-wide so-called internal Poincaré-
type waves[13] are frequently observed instead. Since it is completely unclear, how Poincaré
waves in complicated basins should be parameterized in terms of the Coriolis parameter
in a one-dimensional model, the Coriolis terms in (2.37) will be ignored. If the x-axis
is aligned with the horizontal velocity vector, it is sufficient then to retain only the x-
component of (2.37).

The ommission of the Coriolis forces, however, causes a serious problem in one-dimensional
models: Without a momentum sink, wind-driven surface layer velocities will inexorably
increase and, in the course of a seasonal simulation, erroneously enhance mixed layer deep-
ening and cooling of epilimnetic water. A similar problem in oceanography led MELLOR
[164] very recently to suggest the addition of a simple sink term of the form $P_u^{\mathrm{damp}} = -c_D u$
(with the new model constant c_D) to the right hand side of $(2.37)_1$. Clearly, in the absence
of a pressure-gradient and frictional forces, this term leads to an exponential decay of the
velocity with the time-scale $1/c_D$. Even though this approach was demonstrated to yield
acceptable results in practice, it is rejected here for the introduction of the *dimensional*
model constant, c_D. A similar approach, avoiding this complication, has been recently

---

[12]The expression "medium" refers here to basins that are large enough for rotational effects to become
important, but small enough for these effects not to become dominant (see MORTIMER [177]).

[13]Different types of long internal waves occurring in rotating enclosed basins are very briefly discussed in
Appendix B. For a comprehensive overview the reader is referred to standard texts on lake hydrodynamics
(MORTIMER [177], HUTTER [114, 115]).

suggested by JÖHNK [130]. This author introduced a different damping term of the form

$$P_u^{\mathrm{damp}} = -\frac{1}{A}\frac{\partial A}{\partial z}c_D|u|u \qquad (4.20)$$

to the right hand side of $(2.37)_1$. Since the model constant $c_D \approx 0.1$ is dimensionless, a greater range of applicability of this formulation is expected. Note, that (4.20) formally resembles the classical friction law for the wall stress in a turbulent boundary layer flow, weighted by the area to volume ratio at depth z. Using (4.20), and neglecting the Coriolis terms as discussed above, the momentum equation (2.37) in its horizontally integrated form can be written as

$$\frac{\partial u}{\partial t} = -\frac{1}{\rho_0}\frac{\partial p}{\partial x} + \frac{1}{A}\frac{\partial}{\partial z}\left(A\left(\nu + \nu_t\right)\frac{\partial u}{\partial z}\right) - \frac{1}{A}\frac{\partial A}{\partial z}c_D|u|u \ , \qquad (4.21)$$

where the pressure-gradient has to be prescribed[14]. It can be either neglected (JÖHNK [130]) or parameterized by a simple model of the seiche motion (SVENSSON [251]).

4.3.3   Physical Parameterizations

Production terms

The incoming solar radiation was calculated from astronomical and geographical data according to KIRK [138] and FORSYTHE ET AL. [76]. It was corrected for the effects of cloud shading and wind dependent surface water reflectivity.

The decay of the short-wave radiation, I, in the water column is described according to Beer's law,

$$\frac{\mathrm{d}I}{\mathrm{d}z} + (k_{cw} + k_{\mathrm{Chla}}(z))\,I = 0 \ , \qquad (4.22)$$

where k_{cw} is the extinction coefficient of clear water and $k_{\mathrm{Chla}} = a_{\mathrm{Chla}}\mathrm{Chla}$ is the chlorophyll-a specific extinction coefficient depending on the constant absorption coefficient, a_{Chla}, and the concentration of chlorophyll-a, Chla. The solution of (4.22) is

$$\begin{aligned} I \ &= \ I_{\mathrm{surf}}\,\exp\left(-\int_0^z (k_{\mathrm{cw}} + a_{\mathrm{Chla}}\mathrm{Chla}\,(\overline{z})\,)\,\mathrm{d}\overline{z}\right) \\[2mm] &= \ I_{\mathrm{surf}}\,\exp\left(-\left(k_{\mathrm{cw}} + \frac{1}{z}a_{\mathrm{Chla}}\int_0^z \mathrm{Chla}\,(\overline{z})\,\mathrm{d}\overline{z}\right)z\right) \qquad (4.23)\\[2mm] &= \ I_{\mathrm{surf}}\,\exp\left(-k_{\mathrm{eff}}\,(z)\,z\right) , \end{aligned}$$

---

[14]The flux of momentum from an infinitesimal water volume, $dv = A(z)dz$, at depth z through the bottom boundary area, dA, at that depth leads to the factor $1/A(\partial A/\partial z)$ in front of the damping term. This factor expresses simply the ratio of water volume to boundary area at depth z.

where I_{surf} denotes the short-wave radiation just below the water surface. Note, that the effective extinction coefficient, k_{eff}, defined implicitly in (4.23) is different from the local extinction coefficient $k = k_{cw} + k_{\mathrm{Chla}}$. The production of heat at depth z will then be described by taking the divergence of the radiative heat flux,

$$P_{\mathrm{rad}} = \frac{\partial I}{\partial z} \quad . \tag{4.24}$$

The extinction coefficient for clear water was determined by the empirical formula of HENDERSON-SELLERS [107],

$$k_{cw} = \frac{1.7}{z_{Secchi}} \quad . \tag{4.25}$$

Using a Secchi-depth of $z_{Secchi} \approx 7.6\,\mathrm{m}$, measured on January 2 when the chlorophyll-a concentration was still negligible, (4.25) yields the clear-water extinction coefficient of Lake Ammer, $k_{cw} = 0.22\,\mathrm{m}^{-1}$. For the chlorophyll-specific absorption coefficient the value of $a_{Chla} = 0.02\ \mathrm{m}^2\ \mathrm{mgChla}^{-1}$ from the work of HÄSE [105] was adopted. Note, that the
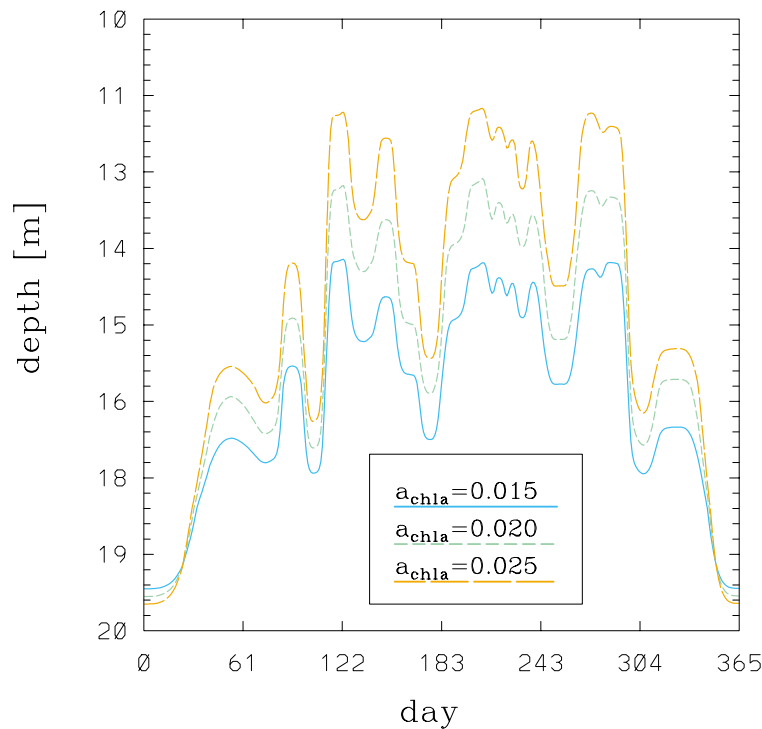
Figure 4.32:   Euphotic depth (corresponding to the depth of 1% residual surface radiation) as a function of the chlorophyll-specific absorption coefficient, a_{Chla}, for Lake Ammer in 1996. The clear water attenuation coefficient is $k_{cw} = 0.22\,\mathrm{m}^{-1}$, a_{Chla} is given in units of $\mathrm{m}^2\ \mathrm{mgChla}^{-1}$.

biological model is quite sensitive to the choice of this parameter, since, as illustrated in Fig. 4.32, a_{Chla} largely determines the euphotic depth. Moderate variations of the

chlorophyll-specific absorption coefficient entail variations of the euphotic depth up to a few meters. The position of the euphotic depth is crucial for the survival and the photosynthetic activity of algae in the metalimnion, and hence for the creation and the extent of the metalimnetic oxygen minimum observed in Lake Ammer.

The production of heat due to the geothermal heat flux, q_{geoth}, through the boundary of a layer of height dz is described by

$$P_{geoth} = \frac{1}{A}\frac{\partial A}{\partial z}\, q_{geoth}\ , \tag{4.26}$$

where $(\partial A/\partial z)/A$ is an approximation for the ratio of the volume of a layer of thickness dz to its boundary, dA, at depth z (see above). The overall heat production, P_θ, defined in (4.18), is then given by

$$P_\theta = P_{\text{rad}} + P_{\text{geoth}}\quad . \tag{4.27}$$

4.3.4 Boundary Conditions

According to the law of Stefan-Boltzmann, the long-wave radiative loss at the water surface, ϕ_w, is given by

$$\phi_w = \epsilon_w \sigma T_w^4\ , \tag{4.28}$$

where T_w is the surface water temperature in Kelvin, $\sigma = 5.67\ 10^{-8}\ \mathrm{W\,m^{-2}\,K^{-4}}$ the Stefan-Boltzmann constant, and $\epsilon_w = 0.97$ the emissivity of water as suggested by HENDERSON-SELLERS [107]. A similar expression is stated for the incoming atmospheric long-wave radiation,

$$\phi_a = \epsilon_a \sigma T_a^4\ , \tag{4.29}$$

though it is evident that different atmospheric radiators at different heights contribute to ϕ_a. For the "global" approach (4.29), an expression for the atmospheric emissivity, ϵ_a, as proposed by SWINBANK [253], was used:

$$\epsilon_a = a_0 T_a^2\ , \tag{4.30}$$

where the model constant a_0 was assigned the value $a_0 = 0.937\ 10^{-5}\ \mathrm{K^{-2}}$. Since (4.30) is applicable only for clear skies, it has been suggested by HENDERSON-SELLERS [107] to modify this value by the factor $(1 + 0.17C)$, where C is the fraction of the sky covered by clouds.

Most formulae for the evaporative and convective heat losses at the water surface are of the forms (HENDERSON-SELLERS [107])

$$\phi_e = f(U_{\text{wind}})(e_{\text{sw}} - e_a)\ , \tag{4.31}$$

and

$$\phi_c = f^*(U_{\text{wind}})(T_w - T_a) \quad . \tag{4.32}$$

where e_{sw} is the saturation vapour pressure at the surface, e_a the actual vapour pressure in the air (both in Pa), T_w the water temperature, and T_a the air temperature in Kelvin. U_{wind} refers to the wind speed at a given height above the water level.

BOWEN [19] first formulated the empirical relation between convective and evaporative heat transfer,

$$\gamma = \frac{f^*(U_{\text{wind}})}{f(U_{\text{wind}})} \quad , \tag{4.33}$$

where

$$\gamma \approx 62 \text{PaK}^{-1} \quad . \tag{4.34}$$

Hence, only one of the wind functions f and f^* needs to be described.

In his extensive literature survey, SWEERS [252] concluded that the formulae of MCMIL-LAN [161] for the wind function f be the most reliable ones. A very similar form, however adjusted in particular to alpine lakes, was suggested by MARTI AND IMBODEN [159]. It reads

$$f(U_{10}) = \rho_{\text{water}} \, L \, a(1 + bU_{10}) \, , \tag{4.35}$$

for wind measurements on land at the 10 meter height given in ms^{-1}. The parameters used for Lake Ammer were $a = 1.36 \cdot 10^{-11}$ ms^{-1} and $b = 0.59$ sm^{-1}. Here, L denotes the latent heat of evaporation of water at the surface water temperature.

Thus, the overall heat flow perpendicular to the surface is

$$\phi_{\text{tot}} = \phi_w + \phi_a + \phi_c + \phi_e \quad . \tag{4.36}$$

The heat flux through the bottom boundary is equal to the geothermal heat flux, q_{geoth}. Since $q_{\text{geoth}} \approx 50 \, \text{mW} \, \text{m}^{-2}$ only, it is ignored.

The flux of momentum through the upper surface of a lake can be described by (HENDERSON-SELLERS [107])

$$\begin{aligned} \tau &= 0.00125 \, \rho_{\text{air}} \, U_{10}^{1.5} \qquad \text{for } U_{10} \leq 1.0\text{ms}^{-1} \, , \\ \tau &= 0.0005 \; \rho_{\text{air}} \, U_{10}^{2.5} \qquad \text{for } U_{10} \geq 1.0\text{ms}^{-1} \quad . \end{aligned} \tag{4.37}$$

The model results were not sensitive with respect to the precise form of the wind-stress parameterization.

4.3.5 The Oxygen Model

The temporal and spatial evolution of the oxygen concentration, O, is described by (4.19). It is assumed that the overall production or depletion of oxygen consists of the sum of different source and sink terms,

$$P_O = P_{\text{photo}} + R + S_{\text{BOD}} + S_{\text{SOD}} , \qquad (4.38)$$

where P_{photo} is the production by photosynthesis, R the respiration of algae, S_{BOD} the total biochemical oxygen demand, and S_{SOD} the oxygen demand exerted by the sediment.

Production by Photosynthesis

Photosynthesis is understood as a biochemical process depending on temperature, solar radiation and nutrients. However, no explicit biological model for the algal growth is supplied. Instead, the biomass of phytoplankton is represented by measured values of the chlorophyll-a concentration, thus implicitly including nutrient limitation, zooplankton grazing, etc.

The photosynthetic production is taken to be proportional to the biomass (expressed in terms of the chlorophyll-a concentration, Chla). Photosynthetic production can be formulated then according to

$$P_{\text{photo}} = r \, \nu_{\text{max}} \, Y_{\text{OChla}} \, \Theta_P^{\theta - 20^o} \tanh\left(\frac{I_{\text{PAR}}}{I_S}\right) \text{Chla} , \qquad (4.39)$$

where ν_{max} is the maximum growth rate of algae under ideal conditions, Y_{OChla} a yield-factor (quantifying the amount of oxygen obtainable at a given chlorophyll-a concentration), Θ_P a model constant determining the temperature dependence of the biochemical processes, I_{PAR} the photosynthetically active short-wave radiation, and I_S a constant of the light limitation model (see below).

The term r appearing on the right hand side of (4.39) accounts for the fact that not all of the measured chlorophyll-a corresponds to living algae. In fact, at greater depths a considerable fraction of the biomass, represented by the chlorophyll-a concentration, may be dead. Recently, Jöhnk [130] attacked this problem by describing a vertical profile for the factor r,

$$r = \frac{1}{1 + \left(\frac{z}{z_c}\right)^{p_c}} , \qquad (4.40)$$

where $z = z_c$ corresponds to the depth, where half of the algae are either dead or alive. z_c can be conveniently identified with the euphotic depth. The exponent p_c is a measure for the width of the transition region. $p_c \to \infty$ corresponds to zero width, i.e. to a step-wise transition.

The cholorphyll-a concentration, Chla, is specified in μgChla l^{-1}. STEFAN AND FANG [244] set the yield-factor to $Y_{\mathrm{OChla}} = 0.125$ mgO$_2$ μgChla^{-1}. Since the maximum growth rate of algae typically is about $\nu_{\mathrm{max}} \approx 1\text{--}3\,\mathrm{d}^{-1}$, one may calculate an average first order production coefficient $k_P = \nu_{\mathrm{max}} Y_{\mathrm{OChla}} = 0.25$ mgO$_2$ μgChla^{-1} d^{-1}, only corrected by the temperature adjustment coefficient $\Theta_P = 1.036$. These values are taken from STEFAN AND FANG [244] fitted to the data of MEGARD [162].

To account for the effects of light limitation on algal growth and photosynthetic production, the simple model of JASSBY AND PLATT [128] is adopted. This model does not include a parameterization of light inhibition in the case of extremely strong short-wave radiation. According to HARRIS [104], the value of the model constant I_S is mostly between 60–100 μE m^{-2} s^{-1} PAR (corresponding to $I_S \approx 12.5\text{--}25\,\mathrm{Wm}^{-2}$). A value of $I_S = 20\,\mathrm{Wm}^{-2}$ is chosen here.

Respiration

Respiration is modelled as a first-order kinetic process related only to the temperature and the concentration of chlorophyll-a,

$$R = r\,\nu_R\,Y_{\mathrm{OChla}}\,\Theta_R^{\theta - 20^\circ}\,\mathrm{Chla} \quad . \tag{4.41}$$

Clearly, the factor r in this equation implies that only living algae contribute to respiration.

The assumption is made that the yield-factor, Y_{OChla}, for respiration is equal to that for production. Considering a respiration rate, ν_R, of roughly ten percent of the growth rate (see HENDERSON-SELLERS [107]), a combined coefficient,

$$k_R = \nu_R Y_{\mathrm{OChla}} = 0.025\ \mathrm{mgO_2}\,\mu\mathrm{gChla}^{-1}\,\mathrm{d}^{-1}\ , \tag{4.42}$$

can be calculated.

STEFAN AND FANG [244] reported a range of $k_R \approx 0.0025 - 0.075$ mgO$_2$ μgChla^{-1} d^{-1} and corrected for the influence of temperature with $\theta_R = 1.045$. The value of PATTERSON

ET AL. [190] can be converted to $k_R = 0.082 \, \mathrm{mgO_2 \, \mu gChla^{-1} \, d^{-1}}$. However, their value seems to include also the respiration of bacteria.

Biochemical Oxygen Demand

The total biochemical oxygen demand (BOD) of organic material (detritus and dissolved organic carbon (DOC)) in a lake is a function of the decaying biomass expressed in oxygen equivalents (THOMANN AND MUELLER [259]). This concept leads to a sink term of the form

$$S_{\mathrm{BOD}} = \nu_B \, \theta_B^{\theta - 20^0} \mathrm{BOD} \, , \tag{4.43}$$

where ν_B is the first-order decay coefficient, θ_B the temperature adjustment coefficient, and BOD the oxygen equivalent of organic material subject to decay (measured in $\mathrm{mgO_2 \, l^{-1}}$). THOMANN AND MUELLER [259] suggested a rather large range $\nu_B \approx 0.1\text{--}0.5 \, \mathrm{d^{-1}}$ and $\theta_B \approx 1.02\text{--}1.1$.

So far, no assumption has been made about the amount of organic matter available for decay. It is, however, possible to relate the primary production (here represented as chlorophyll-a) to the production of organic matter (measured, e.g., as carbon). Organic matter in turn is related to detritus and BOD. In fact, this argument was implicitly also used by STEFAN AND FANG [244], when relating values for BOD to the trophic state of a lake. Here, the more general relation

$$S_{\mathrm{BOD}} = (1 - r) \, k_B \, \theta_B^{T - 20^\circ} \mathrm{Chla} \tag{4.44}$$

is suggested, which is in form identical to (4.41). However, only the fraction $1 - r$ of algae (i.e. the fraction of dead algae) is subject to bacterial decay. Since the ratio of chlorophyll-a to carbon varies greatly between species the precise value of k_B has to be found by calibration. Both approaches shall be discussed in Section 4.3.7.

Sedimentary Oxygen Demand

To account for the sedimentary oxygen demand of settled phytoplankton, dead aquatic plants and detritus, the model also implements a bottom area dependent sink term according to THOMANN AND MUELLER [259],

$$S_{\mathrm{SOD}} = \frac{1}{A} \frac{\partial A}{\partial z} \, S_{\mathrm{b20}} \, \theta_S^{\theta - 20^o} \quad . \tag{4.45}$$

Here, S_{b20} is the bulk rate of the sedimentary oxygen demand, measured in $gO_2 \, m^{-2} \, d^{-1}$. Depending on the conditions at the lake bottom, THOMANN AND MUELLER [259] suggested different values for S_{b20}. For sandy bottom, appropriate for Lake Ammer, they give the range $S_{b20} \approx 0.2$–$1.0 \, gO_2 \, m^{-2} \, d^{-1}$. S_{SOD} is strongly temperature dependent. Usually, a value of $\theta_S = 1.065$ is used for the temperature adjustment, but STEFAN AND FANG [244] for example suggest the somewhat higher value $\theta_S = 1.13$. Since the hypolimnetic oxygen budget is very sensitive to S_{SOD}, and very little precise information about it exists, these values had to be refined by model calibration.

4.3.6   Surface Re-aeration

Particularly in the absence of photosynthetic production, surface re-aeration is a major source term in the integral oxygen budget. Here, it is implemented as a surface-flux boundary condition in (4.19), assuming the flux to be proportional to the difference between actual and saturated oxygen concentrations at the surface,

$$q_C = k_e(C_{sat} - C_{surface}) \,, \tag{4.46}$$

where the saturation concentration, C_{sat} in $mgO_2 l^{-1}$, is described according to MORTIMER [178] by

$$C_{sat} = 2234.3374 \, (\theta_{surf} + 45.93)^{-1.31403} \,, \tag{4.47}$$

θ_{surf} being the surface temperature of lake water. The oxygen exchange coefficient, k_e, is usually given as a function of the wind speed. Here, the suggestion of WANNIKHOF ET AL. [288],

$$k_e = 0.108 \, U_{10}^{1.64}(600/S_{ct})^{0.5} \,, \tag{4.48}$$

is adopted. Using a representation of the Schmidt number of oxygen at the surface, S_{ct}, derived by STEFAN AND FANG [244], (4.48) can be re-written as

$$k_e = 0.02256 \left(0.10656 \, e^{(-0.0627\theta)} + 0.00495\right)^{-0.5} U_{10}^{1.64} \,, \tag{4.49}$$

where the temperature is given in centigrades and the velocities in ms^{-1}.

4.3.7   Results

Lake Ammer

Lake Ammer is a medium-sized Alpine lake, situated in Southern Germany. It is a channel like basin with a length of approximately $16 \, km$ (from South to North) and maximum

width of less than 5 km. Its maximum depth is 82 m. The topography is illustrated in the left panel of Fig. 4.33. Meteorological data for this lake were available for the
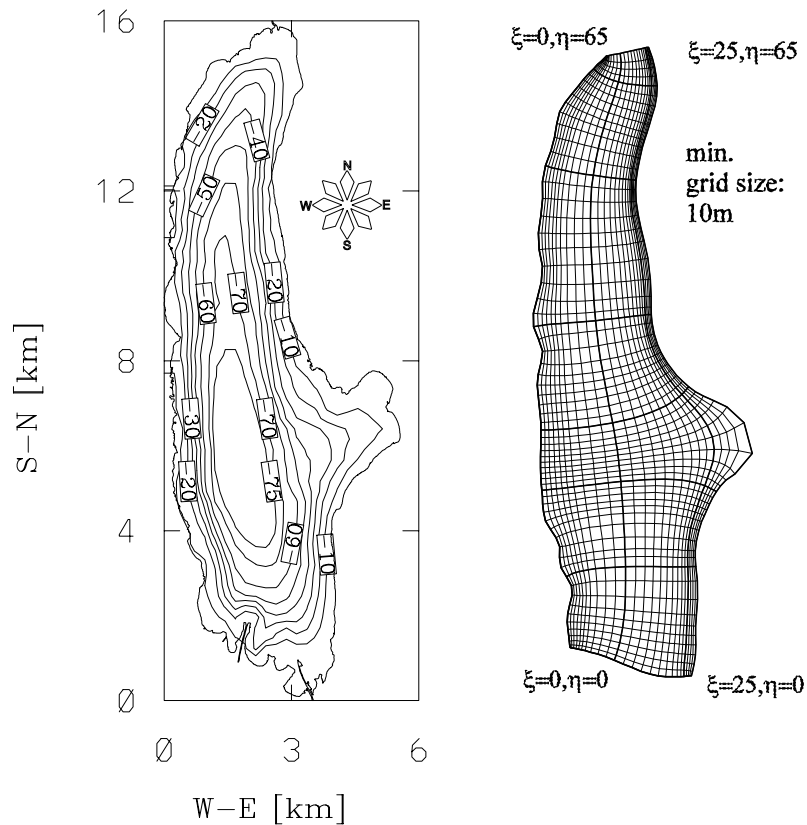
Figure 4.33: The topography of Lake Ammer (left) and the horizontal orthogonal grid (right). For later reference: The horizontal velocity components u and v refer to the local direction of the curvilinear coordinates ξ and η, respectively.

years 1990 and 1996 from the nearby weather station at Wielenbach and also from the German Weather Service (DWD). They included data of wind speed and direction, air temperature, humidity, and cloud cover. Limnological data were made available by the Bavarian Department of Water Management. This institution measured profiles of water temperature, conductivity, chlorophyll-a, and dissolved oxygen at the deepest part of the lake (see Fig. 4.33).

Even though Lake Ammer is one of the largest German lakes, apparently measurements of neither mean flow nor turbulent parameters are known. A three-dimensional circulation model was used to derive at least some information about the overall dynamics of this lake. However, none of the results computed by this model could be verified for the lack of data. For later reference, the computational grid of the three-dimensional numerical model described in UMLAUF ET AL. [283] is displayed in the right panel of Fig. 4.33.

Temperature Stratification

The temperature stratification of Lake Ammer was measured at several dates during the years 1990 and 1996. The model was calibrated with temperature and oxygen data from 1996 and verified with those of the exceptional year 1990, which showed a very pronounced metalimnetic oxygen minimum of about 1 mgO$_2$/l below the thermocline (see JÖHNK AND HUTTER [131]). The model was initialized with a nearly homogeneous temperature profile as measured on January 2. The total radiative heat flux was derived semi-empirically as described above; other meteorological parameters were available (see above). The results for the year 1996 are displayed in the panels of Fig. 4.39 and Fig. 4.40. These figures show a good overall agreement between the measured data and the computation, and thus demonstrate the predictive capabilities of the two-equation model.

Nevertheless, at some dates, discrepancies between predictions and measurements can be observed: The initial formation of the thermocline on April 29 as displayed in Fig. 4.39 is not met very well by the model: Obviously, turbulent mixing is overestimated and cannot be out-balanced appropriately by the stabilizing effect of solar radiation until May 29. From that point, the data are represented remarkably well by the model. Only on July 23 and 29 the model predicts a surface mixed layer of increasing depth in contrast to the measured data, which exhibit a nearly linear decrease of temperature with depth. This behaviour is assumed to be related to a strong inflow event from July 9 until July 11, leading to horizontal advection of differently temperated water which a one-dimensional model cannot cope with. The simulation results following August 8 again show good agreement with the data.

Calibration of the Oxygen Model

The results of the temperature simulation confirm the capability of the k-ϵ model to provide a sufficient representation of the epilimnetic exchange coefficients and the temperature profiles. However, not much can be said about the exchange processes in the lower metalimnion and hypolimnion. In fact, after the formation of a stable thermocline in June (see Fig. 4.39) and after the stored turbulent kinetic energy is dissipated, the turbulence model calculates only molecular diffusivities in the hypolimnion. Since no information was supplied about internal wave and boundary layer mixing, this had to be expected.

It was remarked in the introduction to Section 4.2 that the measured net diffusivities in

the hypolimnion are in general higher than the molecular value. In this context it was also illustrated that the seiching induced by long internal waves can lead to a considerable enhancement of mixing in the bottom boundary layer of a lake. In this case, and if the near-sediment density stratification is not too strong, the theory developed by WÜEST AND GLOOR [298] predicts a net hypolimnetic diffusivity much above the molecular level. However, the same authors also pointed out that if the bottom currents are too weak and the water adjacent to the sediment is chemically stratified (as it is the case, e.g., in Zugersee, Switzerland), almost no boundary mixing occurs and the boundary layer diffusivities are close to molecular. In this case, enhanced values of the net hypolimnetic diffusivity are predominantly due to intermittent mixing in local turbulent patches in the bulk of a weakly stratified hypolimnion.

As already remarked, there are no measurements of hydrodynamical quantities in Lake Ammer. However, a three-dimensional numerical model[15] was available that has been already successfully applied to Lake Constance, which is in many respects similar to Lake Ammer (WANG [285], WANG AND HUTTER [286, 287], CHUBARENKO ET AL. [49]). It is expected that with this tool at least some insight can be gained in the fundamental dynamics of Lake Ammer, first of all in the structure of the internal oscillations that lead to enhanced boundary mixing in some other lakes (see discussion in Section 4.2).

The numerical results shown in Fig. 4.34 are taken from UMLAUF ET AL. [283]. This figure illustrates the reaction of Lake Ammer after the onset of a constant and uniform wind of moderate strength ($3\,\mathrm{m/s}$) from South. A typical summer stratification, according to the measurements introduced above, was prescribed. The main dynamical features are very briefly discussed here; only the possibility of seiche-induced boundary mixing in Lake Ammer shall be touched. For a more detailed analysis the reader is referred to the original publication.

The upper two panels of this figure reveal that, after the onset of the wind, an oscillation of the alongshore current at the western and eastern shore with a period of about a day is the predominant flow component. It can be shown that this velocity pattern corresponds to a Kelvin-type wave, circulating counter clockwise around the lake (see Appendix B). For the prescribed wind field (blowing along the main axis of the channel-like basin of Lake Ammer) the lateral u-component of the velocity (see Fig. 4.33) in the lake is very small (see lower left panel of Fig. 4.34). However, the influence of the Kelvin-type wave

---

[15]The model solves the three-dimensional shallow-water equations and the energy equation on a curvilinear grid. Turbulent diffusivities are determined by a zeroth-order closure with spatially varying diffusivities. A detailed description of this and a related model is given in UMLAUF ET AL. [283].
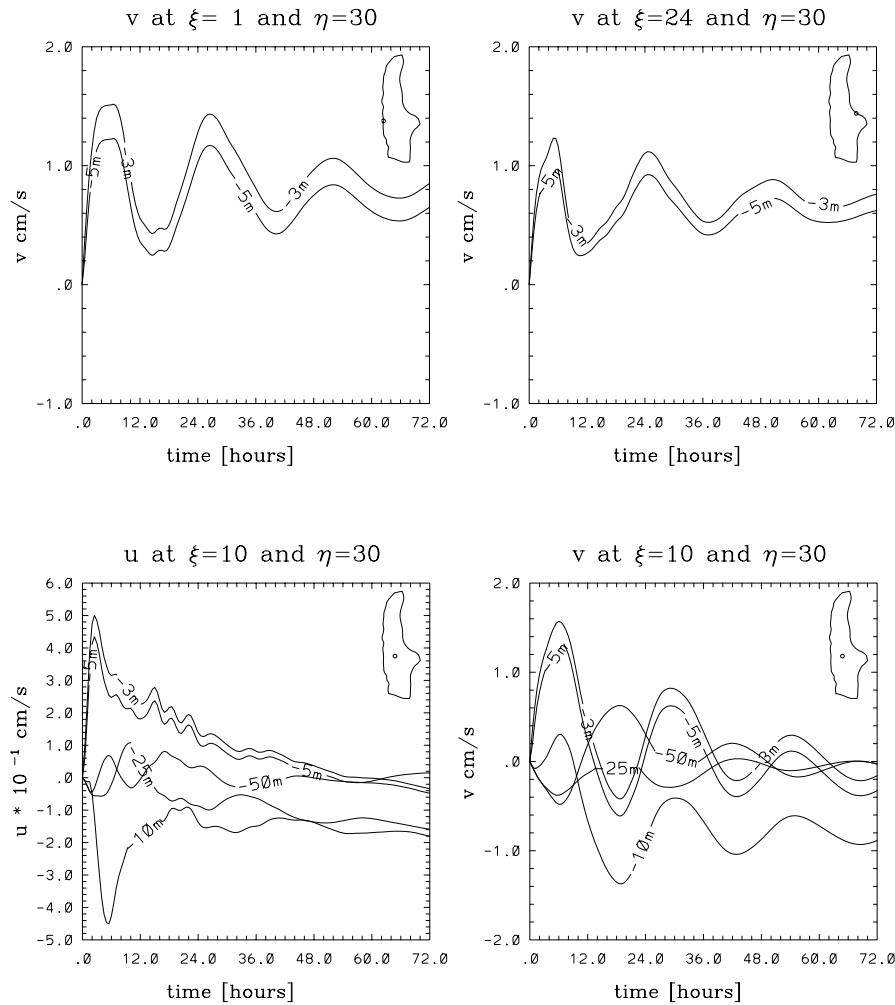
Figure 4.34:   Time-series of current speeds at different positions in the stratified Lake Ammer for a constant and uniform wind of $3\,\mathrm{m/s}$ from South (starting at $t = 0$). Upper panels: Longshore component of the velocity at the western (left panel) and eastern shore at the depth levels $3\,\mathrm{m}$ and $5\,\mathrm{m}$. Lower panels: Lateral velocity (left panel) and longitudinal velocity in the middle of the lake at the depth levels $3\,\mathrm{m}$, $5\,\mathrm{m}$, $10\,\mathrm{m}$, $25\,\mathrm{m}$, and $50\,\mathrm{m}$. Position labels are shown in the upper right corner of each panel. For the numerical grid see Fig. 4.33.

is also felt in the longitudinal v-component of the velocity in the middle of the lake (lower right panel), indicating that the internal Rossby radius is comparable to the channel width. The hypolimnion is predicted to oscillate with a phase-shift of approximately π with respect to the epilimnion (lower right panel). Hence, the three-dimensional model predicts a seiche-induced oscillation of the whole bottom boundary layer of Lake Ammer. The seiche period of approximately one day is comparable to the period of Lake Alpnach[16], and a comparable resonant effect with the diurnal component of the wind field is to be

[16]Note, however, that the seiche period of one day in Lake Ammer corresponds to the first vertical mode, whereas in Lake Alpnach the diurnal wind excites predominantly the second vertical mode.

expected. It is very likely, that this oscillation causes enhanced mixing at the bottom in a manner outlined in Section 4.2. However, the hypolimnetic current speed is low (less than 1 cm/s for the given wind speed) and is not comparable to the value of almost 4 cm/s in Lake Alpnach, even if the model is run with a stronger wind (not shown).

To examine whether enhanced bottom mixing effectively leads to a well-mixed bottom boundary layer, as in Lake Alpnach, profiles of the oxygen concentration and the conductivity[17] are displayed in Fig. 4.35 for the stagnation period in 1996. Both panels of this
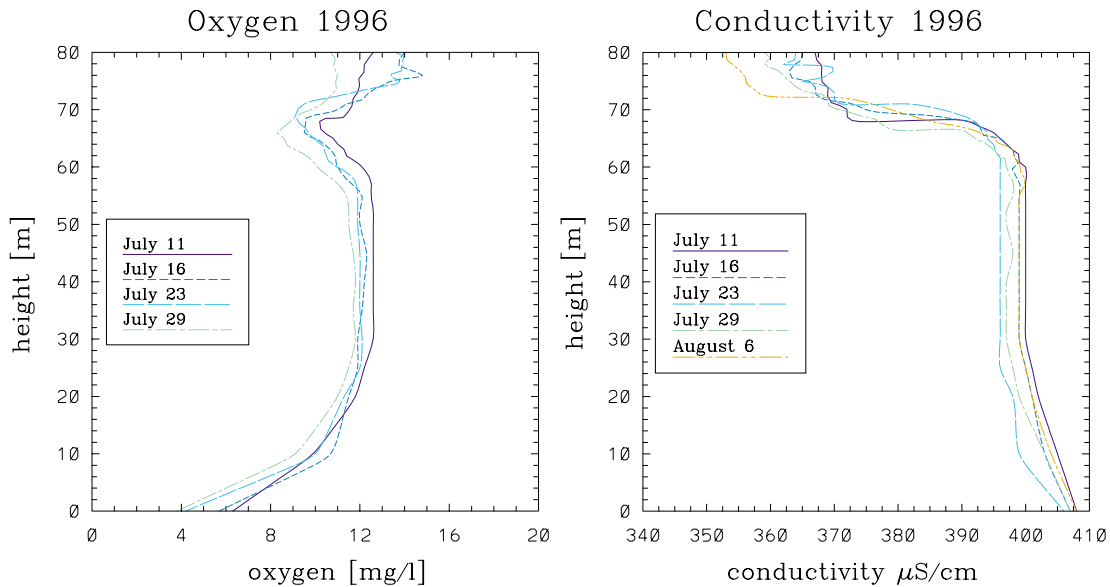
Figure 4.35:   Measured profiles of oxygen (left panel) and conductivity (right panel) at greatest depth of Lake Ammer during the stagnation period in 1996.

figure reveal distinct gradients in the lowest part of the hypolimnion, indicating that the bottom currents are not energetic enough to completely homogenize the fluid adjacent to the sediment. Hence, the dynamics of the bottom boundary layer in Lake Ammer must be considered different from that of Lake Alpnach. This fact does, however, not imply that there is no mixing at all near the sediment: Since the chemical density stratification is weak near the bottom[18], even low current speeds can induce a turbulent bottom boundary layer with high mixing efficiency. The following argument applies: If there is turbulence at the bottom, the only way to explain why the bottom layer is chemically *not* well-mixed, is by assuming a chemical buoyancy flux from the sediment. Strong indicators for the presence of at least some turbulent mixing in the boundary layer are the

---

[17]Since the temperature is nearly homogeneous in the lower part of the hypolimnion, conductivity should be used as a measure for a chemically induced density stratification near the sediment.

[18]Making a rough estimate, the chemical density stratification in the lower 15 m amounts to $N^2 \approx 7 \cdot 10^{-6} s^{-2}$ (BÜHRER AND AMBÜHL [23]). This value is low, but nevertheless dynamically relevant.

completely homogeneous temperature profiles in the lower hypolimnion: Quite contrary, in Zugersee, where the boundary layer diffusivities are close to molecular, an inverse temperature gradient due to the small geothermal heat flux has been observed (WÜEST AND GLOOR [298]). Of course, these arguments are somewhat speculative and have to await a verification by current and microstructure measurements in this lake and a more precise evaluation of the roles of the near-sediment density stratification and the buoyancy flux from the sediment.

To account for enhanced hypolimnetic mixing (be it caused by boundary mixing or not), the most simple parameterization was implemented by adding a constant "background" diffusivity, ν_t^b, in the hypolimnion. This, of course, led to a new parameter that had to be found by model calibration. Thus, three parameters, crucial for the hypolimnetic oxygen budget, had to be specified by the calibration procedure: The sedimentary oxygen demand, the biochemical oxygen demand, and the hypolimnetic diffusivity of oxygen. The chlorophyll-a concentration was measured several times and the data were linearly interpolated to the model's time-steps (see Fig. 4.37, lower panel).

The calibration parameters were subject to two constraints: First, the computed values should give a good fit to the measured oxygen profiles. Second, the global oxygen budget of the hypolimnion should be satisfied.

The total oxygen budget for the lower hypolimnion ranging from the bottom up to a depth of 40 m was formulated as

$$\text{HOD} = \frac{(A_{\text{hyp}} \, S_{\text{SOD}} + V_{\text{hyp}} \, S_{\text{BOD}})}{V_{\text{hyp}}} \ , \tag{4.50}$$

assuming zero net flux at the top of this lake compartment, which is presumably a good approximation for the stagnation period between July and September. The hypolimnetic oxygen demand, HOD, represents the total, time dependent oxygen depletion of the lower hypolimnion. S_{SOD} is the sedimentary oxygen demand according to (4.45), and S_{BOD} is the biochemical oxygen demand, following either from (4.43) or (4.44). $A_{\text{hyp}} = 21.3 \ \text{km}^2$ is the sediment surface of the lake compartment below a depth of 40 m and $V_{\text{hyp}} = 0.497 \, \text{km}^3$ the corresponding water volume. In general, HOD is a function of time. However, during the stagnation period, the oxygen content in the lower hypolimnion was found to be a linear function of time, resulting in a constant hypolimnetic oxygen demand of HOD = 0.037 $\text{mgO}_2 \, \text{l}^{-1} \, \text{d}^{-1}$ (see Fig. 4.36). During this period the oxygen depletion was mainly due to the sedimentary oxygen demand (see below).

The best curve fit to the measured oxygen profiles, still satisfying (4.50), could be found
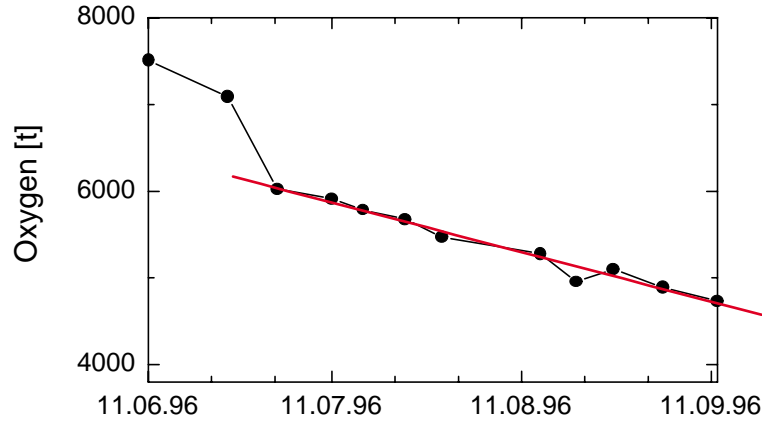
Figure 4.36: Total amount of oxygen in the lower hypolimnion (40 to 80 meters) in 1996 and linear fit to the measured data. The first two points were not included in the regression.

for the hypolimnetic diffusivity $\nu_t^b = 2 \cdot 10^{-5}$ m^2 s^{-1} and for the bulk sedimentary oxygen demand $S_{b20} = 1.5$ gO$_2$ m^{-2} d^{-1} (at 20°C). The temperature adjustment coefficient was set to $\theta_S = 1.13$, a value already used by STEFAN AND FANG [244]. Assuming a constant temperature in the hypolimnion (justified by the panels in Fig. 4.39 and Fig. 4.40), (4.45) and (4.50) can be used to compute the biochemical oxygen demand $S_{BOD} = 0.00268$ mgO$_2$ l^{-1} d^{-1}.

Using (4.43) with a value of $\nu_B = 0.1$ d^{-1} and a bulk value of BOD $= 0.2$ mgO$_2$ l^{-1} as suggested by STEFAN AND FANG [244] leads to the value of S_{BOD} computed above.

Alternatively, using the arguments that led to (4.44), the biochemical oxygen demand can be directly related to the concentration of chlorophyll-a. With the parameter $k_B = 0.075$ mgO$_2$ l^{-1} d^{-1}, the value of S_{BOD} computed above corresponds to a concentration of 0.25 μgChla l^{-1}, if all of the biomass represented by the chlorophyll-a concentration is assumed to be dead and decaying. Both formulae included the same temperature correction coefficient $\theta_B = 1.13$ (suggested by STEFAN AND FANG [244]).

It should be pointed out that besides the obvious relation between S_{SOD} and S_{BOD} via (4.50), there was a strong dependence of both parameters on the choice of the vertical hypolimnetic diffusivity, ν_t^b. Similar to the ideas of IMBODEN AND EMERSON [121] in limnology and PARKER [188] in oceanography, results of the oxygen model were used

here to draw inferences about physical quantities, in this case about the hypolimnetic diffusivity. No measurements of the rate of dissipation or the turbulent diffusivity were performed in Lake Ammer, so it is difficult to assess the utility of this method. Note, that the high value for the sedimentary oxygen demand, S_{b20}, is partly due to the choice of the vertically constant diffusivity derived with the method above. For all these reasons, "veracity" of the parameters derived by model calibration cannot be claimed. There were other choices leading also to good fits to the measured data. For the lack of physical data, it can merely be stated that the selected parameters are in the range reported in the literature and do fit the measured data.

The Metalimnetic Oxygen Minimum

The contour plots in Fig. 4.37 give an overall impression of the major parameters related to the oxygen distribution: Temperature, chlorophyll-a, and oxygen. Some basic correlations between these parameters are immediately evident from this figure: The high epilimnetic oxygen concentration at the beginning of May, e.g., is most likely caused by the high concentration of chlorophyll-a, which indicates the beginning of the algal bloom triggered by increasing epilimnetic temperatures. Also obvious is the increasing influence of the sedimentary oxygen demand, leading to a hypolimnetic oxygen depletion during the months following May.

However, the limits of a one-dimensional model are also indicated by this figure: The distinctive hypolimnetic oxygen maximum in June (located at a depth of approximately 45 m) cannot be explained by any one-dimensional mechanism: Even though the epilimnetic water is over-saturated at that time (see below), its absolute oxygen concentration is lower than that in the central hypolimnion, so any internal redistribution of oxygen cannot be a possible reason. Photosynthetic production also has to be excluded, since the euphotic depth (see Fig. 4.32) is almost certainly too small and there is not enough light for algae to maintain their metabolism. The most probable cause for the hypolimnetic oxygen maximum is the lateral inflow of very cold, saturated riverine water.

A more detailed view of the development of the metalimnetic oxygen minimum is displayed in Fig. 4.38. The upper panel of this figure illustrates the situation in spring: As long as basin-wide mixing occurs the oxygen level is always around saturation. With the beginning of the spring bloom, the water column stabilizes, the mixing becomes less vigorous and due to photosynthetic production oxygen concentrations exceed the saturation point by far.
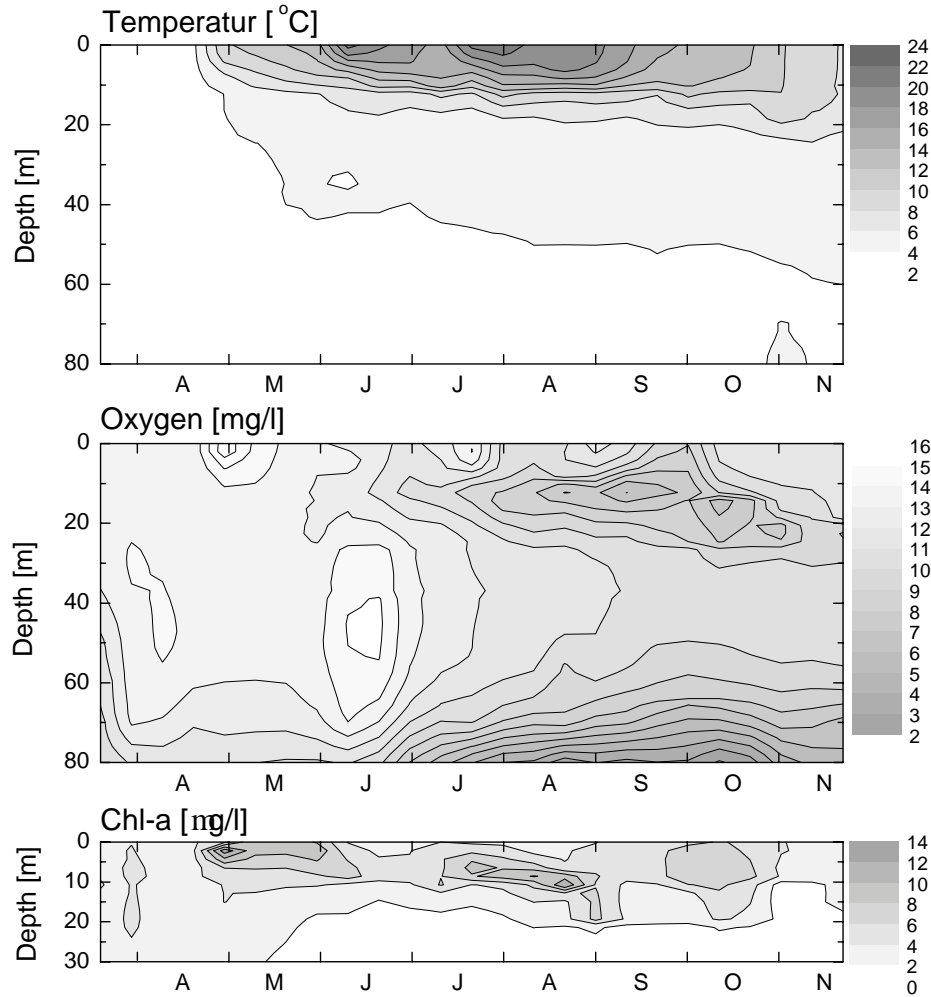
Figure 4.37:   Contour plots of the temperature (upper panel), the oxygen (middle panel), and the chlorophyll-a concentration (lower panel) for 1996. Measurements were taken from March 19 (day 79) until November 20 (day 325).

The middle panel, representative for the situation in summer, exhibits a different picture: Even though the oxygen level in the well-mixed epilimnion is beyond saturation, the formation of a metalimnetic oxygen minimum has already started. The hypolimnion is cut off from the high epilimnetic oxygen concentration, and only very little vertical exchange occurs because of the suppressing effect of stratification. This situation prevails until autumn (lower panel), when stratification becomes weaker and wind mixing is more effective. Saturated epilimnetic water can be mixed in, the minimum is filled up slowly and simultaneously deepened.
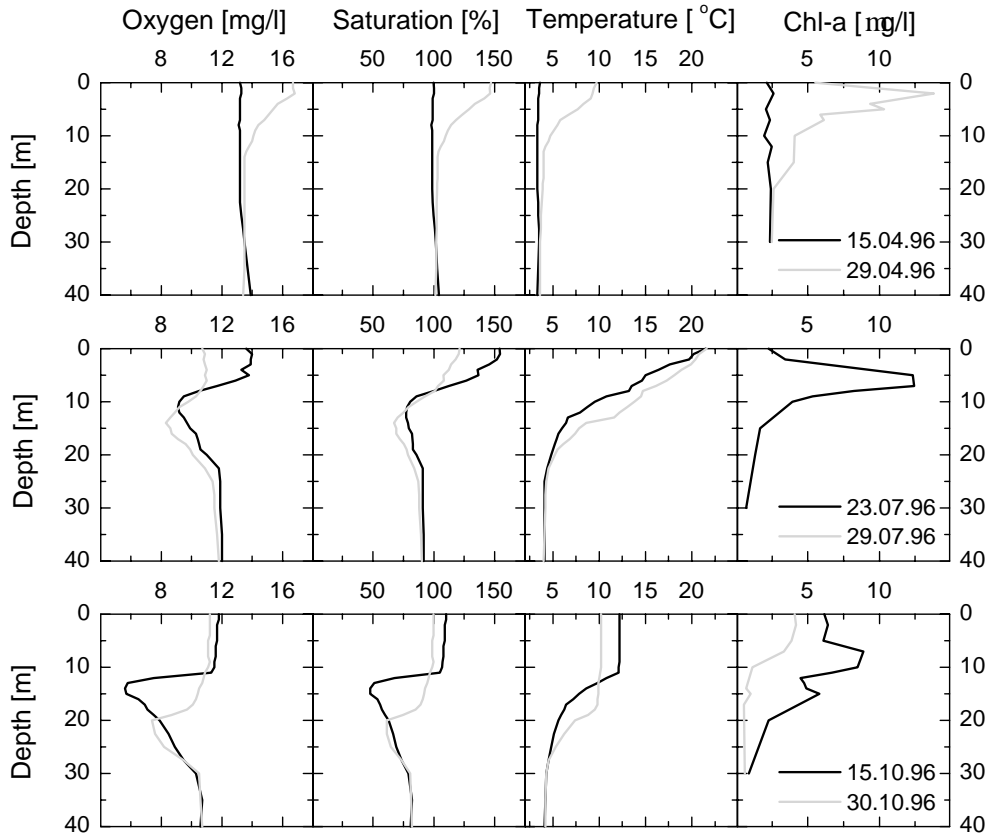
Figure 4.38:   From left to right: Total oxygen concentration, relative oxygen concentration, temperature, and chlorophyll-a concentration in Lake Ammer in 1996. Upper panel: The spring bloom causes a rise in the oxygen concentration by photosynthesis; Middle panel: The formation of the metalimnetic minimum, caused by biochemical oxygen demand, has started; Lower panel: In autumn, over-saturated oxygenated water is mixed down and the minimum is slowly filled up.

The model described above was applied to a lake compartment reaching from the bottom up to a depth of 10 meters to simulate the metalimnetic oxygen minimum. The model results and the measured data for the period of the oxygen minimum are compared in Fig. 4.41. Three domains can be distinguished in each panel:

1. A bottom layer of high oxygen depletion. In this region of high sediment area to water volume ratio, the oxygen budget is dominated by the sedimentary oxygen demand, which can only partly be balanced by the diffusive transport of oxygen from above. During the winter/spring turnover this deficit is filled up again.

2. A hypolimnetic bulk with a combination of sedimentary and biochemical oxygen demand adding up to a comparably small overall oxygen demand.

3. A region of a metalimnetic oxygen minimum at the top of the hypolimnion. Due to the low level of photosynthetically active short-wave radiation at that depth, the oxygen production is low compared to the consumption by respiration and, in particular, biochemical oxygen demand.

The situation described above is somewhat different from that in smaller lakes with high transparency, where a metalimnetic oxygen *maximum*, caused by photosynthetic production, may occur (see STEFAN ET AL. [243], WETZEL [292] for the U.S. lakes). Future studies with the model introduced here will focus on the evolution of the different possible types of oxygen profiles depending on morphometry, irradiance, and temperature stratification. Their relation to euphotic depth was depicted by STEFAN ET AL. [243] for a positive heterograd curve. In Lake Ammer we find a negative heterograd oxygen profile, which can be attributed to the increase of biochemical oxygen demand due to increasing temperature in the metalimnion persisting throughout the stagnation period.

It can be concluded that the metalimnetic oxygen minimum in Lake Ammer is caused by the strongly temperature dependent BOD and the onset and duration of a strong stratification reducing the oxygen transport between epilimnion and hypolimnion. Due to the effects of self-shading, the euphotic depth in August is somewhat larger than 10 m (Fig. 4.32). The high chlorophyll-a concentration at comparable depth (see figure 4.37) presumably indicates a low-light adapted type of algae with oxygen balanced between photosynthetic production and respiration, since there is no evidence in the data of a change in oxygen content during their occurrence. This hypothesis is supported by simulations for the year 1990 exhibiting much lower metalimnetic oxygen concentrations than 1996 (not shown). This year was characterized by an earlier onset of stratification and higher overall temperature, leading to a higher oxygen consumption through BOD in the metalimnion.

Future work will focus on the impact of different climate conditions on temperature structure and oxygen content. In particular, the formation of a metalimnetic oxygen minimum is of great importance for the fishery management. Also the influence of horizontal processes (like horizontal circulation patterns and inflow/outflow effects) will be addressed.
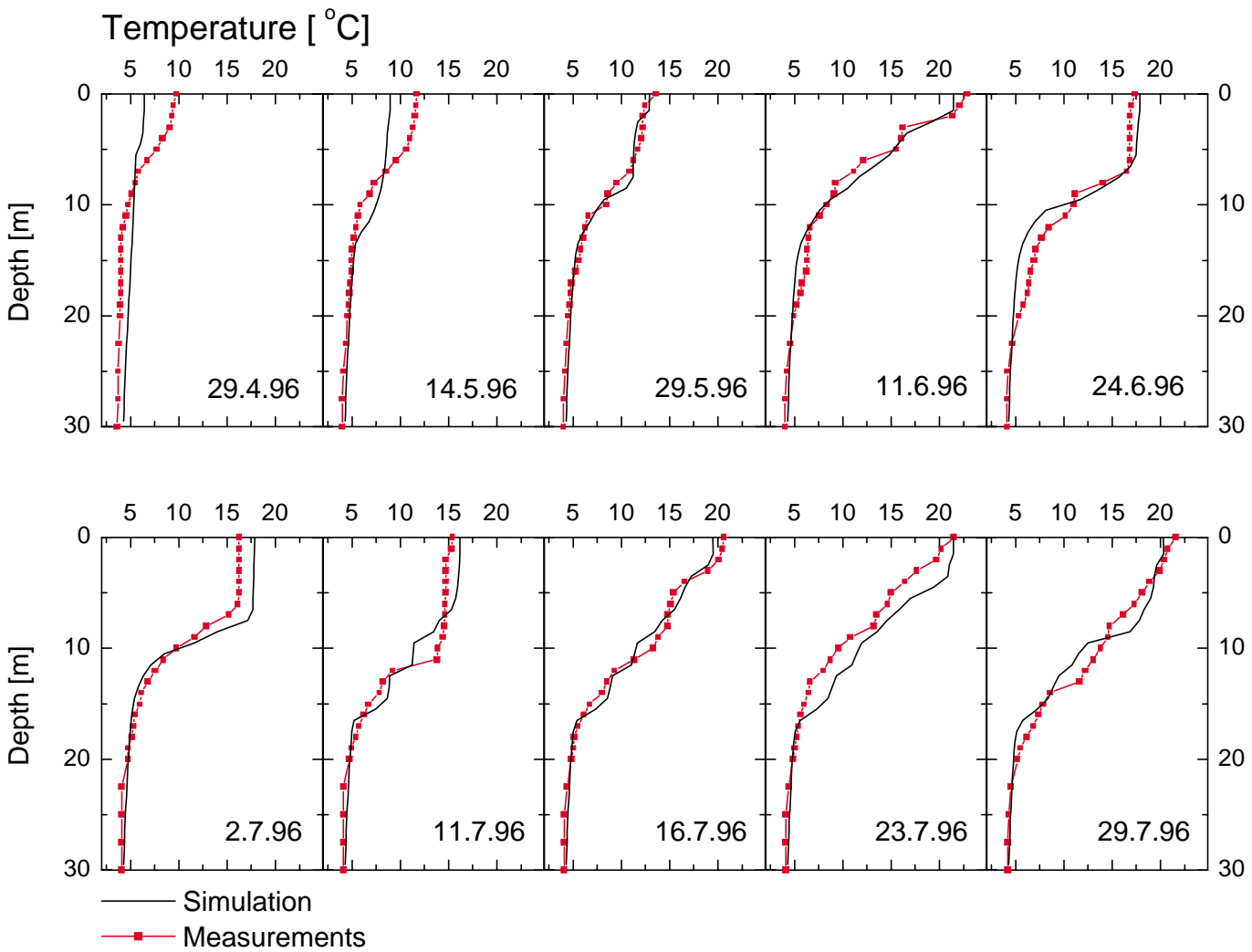
Figure 4.39: Comparison of measured and computed temperature profiles in Lake Ammer in 1996 (April until July)
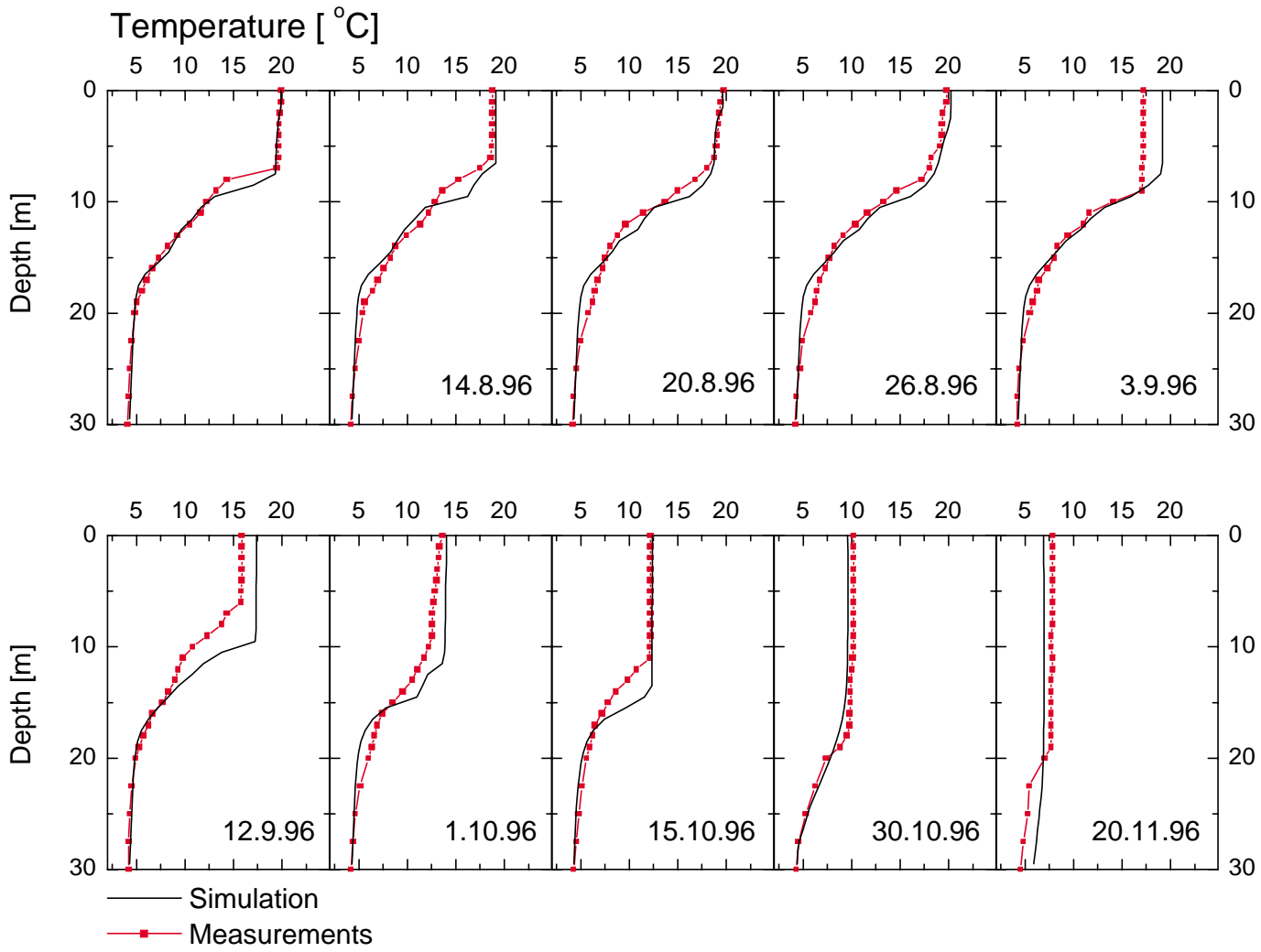
Figure 4.40: Comparison of measured and computed temperature profiles in Lake Ammer in 1996 (August until November)
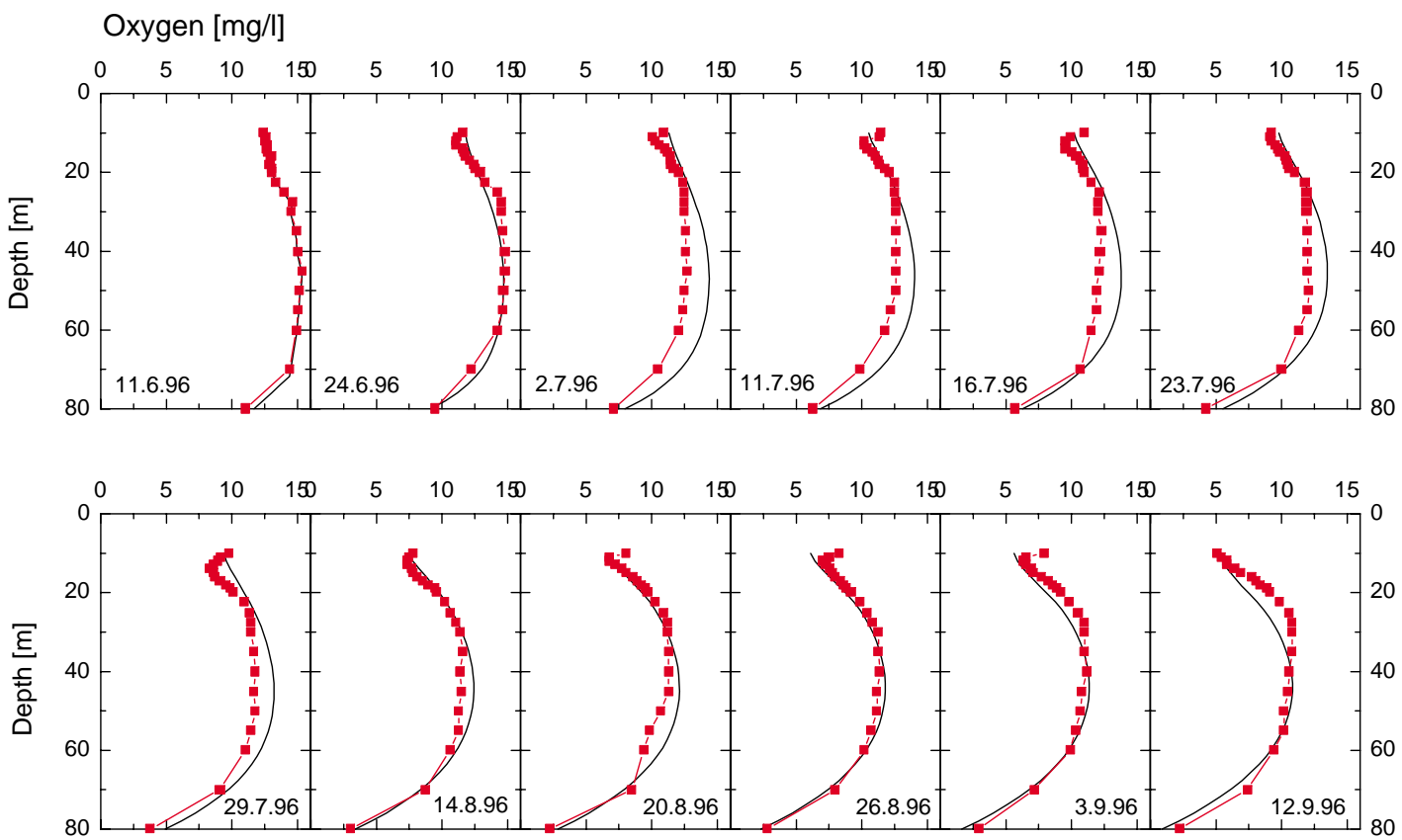
Figure 4.41: Comparison of measured and computed oxygen profiles in Lake Ammer in 1996

Chapter 5

Numerics

5.1   The Finite-Volume Method

The individual differential equations encountered in the preceeding chapters expressed a certain conservation principle. Apparently, all variables obey a generalized balance law that can be formulated as

$$Am\dot{\varphi} = \frac{\partial}{\partial z}\left(Ak\frac{\partial\varphi}{\partial z}\right) + AL\varphi + AS \ , \tag{5.1}$$

where φ denotes the variable considered, m a generalized density, k a diffusivity, and L and S the linear and constant parts of the source term. As discussed in the context of (4.16) in Section 4.3, the horizontal averaging procedure of conservation equations in enclosed basins introduces, in addition, the horizontal area, $A(z)$, at position z.

Numerous numerical procedures are known to solve (5.1). Here, a technique, which is particularly interesting in the context of conservation equations and which is usually referred to as the Finite-Volume (FV) method, is discussed. The FV method insures the total conservation of the variable φ, no matter how coarse the grid may be. This property is of great benefit when dealing with conservation equations. Since the method is well-known[1], only the basic principles are discussed and some particularities emerging in oceanographical and limnological applications are investigated in greater detail below.

The FV method is based on an interesting special case of the *method of weighted residuals* with the weighting function set equal to 1 in a finite subdomain (or volume), V_i, and 0

---

[1]The Finite-Volume method is described in detail in the excellent book by PATANKAR [189].

anywhere else (for the method of weighted residuals, see FINLAYSON AND SCRIVEN [75]). This concept leads to the weak form of (5.1),

$$\int_{V_i} Am\dot{\varphi}\, dz = \left(Ak\frac{\partial\varphi}{\partial z} \right)\Bigg|_{f_i}^{f_{i+1}} + \int_{V_i} AL\varphi dz + \int_{V_i} ASdz \; , \tag{5.2}$$

where f_i and f_{i+1} relate to the lower an upper boundaries of the volume[2] V_i. Adopting certain profile assumptions for the quantities appearing in (5.2) (see PATANKAR [189]), the integration can be carried out explicitly. With the geometrical quantities defined in Fig. 5.1 (for either grid, "A" or "B"), the spatially discretized form of (5.2) reads

$$\dot{\varphi}_i = F_i^u \frac{k_{i+1}^f}{m_i^c} \left(\varphi_{i+1} - \varphi_i \right) - F_i^l \frac{k_i^f}{m_i^c} \left(\varphi_i - \varphi_{i-1} \right) + \frac{1}{m_i^c} \left(L_i\varphi_i + S_i \right) \; , \tag{5.3}$$

where the abbreviations

$$F_i^u = \frac{A_{i+1}^f}{A_i^c \Delta_i \delta_{i+1}} \; , \quad F_i^l = \frac{A_i^f}{A_i^c \Delta_i \delta_i} \tag{5.4}$$

have been used. $\dot{\varphi}_i$ denotes the discretized form of the time derivative of φ. The superscripts "c" and "f" refer to quantities at the center or the face of a finite volume, respectively. As suggested in Fig. 5.1, the volume centers of grid "A" are centered between the volume faces, whereas the faces of grid "B" are centered between the neighbouring grid centers. This is a consequence of the staggered grids used here, in which mean quantities are defined on the "A" grid and turbulent quantities on the "B" grid. The relations obtained above hold unchanged for both grids.

For the boundary volumes expressions can also be obtained. For the lower boundary volume, the relation

$$\dot{\varphi}_0 = \frac{F_0^u k_1^f}{m_0^c} \left(\varphi_1 - \varphi_0 \right) + \frac{1}{m_0^c} \left(L_0\varphi_0 + S_0 \right) + \frac{F_0^l \delta_0}{m_0^c} q_0 \tag{5.5}$$

can be derived. For the upper boundary volume the relation

$$\dot{\varphi_N}^h = -\frac{F_N^l k_N^f}{m_N^c} \left(\varphi_N - \varphi_{N-1} \right) + \frac{1}{m_N^c} \left(L_N\varphi_N + S_N \right) + \frac{F_N^u \delta_{N+1}}{m_N^c} q_{N+1} \tag{5.6}$$

holds likewise (with N replaced by $N-1$ for quantities defined on grid "A"). The flux across the upper and lower volume faces is defined as

$$q = \left| k\frac{\partial\varphi}{\partial z} \right| \quad \text{at the volume faces} \; , \tag{5.7}$$

---

[2]In the one-dimensional case considered here, the integration over a volume simplifies to a one-dimensional integration.

B A
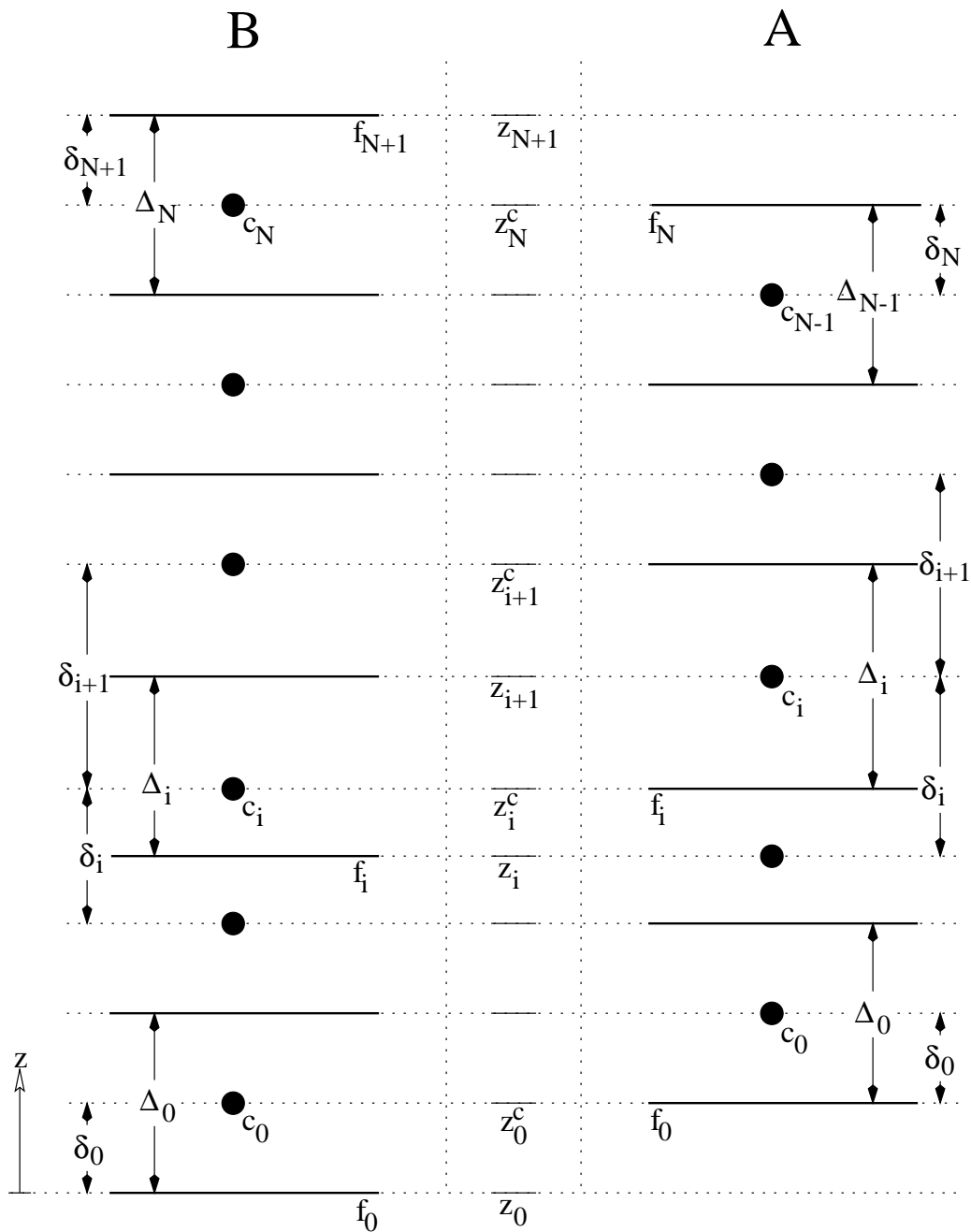
Figure 5.1: The numerical grids used in the Finite-Volume method. "A" and "B" refer to the differently centered grid types defined by PATANKAR [189] (pp. 68). Filled circles denote the centers of the finite volumes, thick horizontal lines their respective faces.

where an influx is counted positive by convention.

Note, that the treatment of the boundary conditions for the turbulent quantities (i.e. quantities on grid "B") is non-standard here. Most oceanic turbulence models that work

on a staggered grid (see, e.g., GOTM, `http://www.gotm.net`) assume the "wall" at the center of the boundary volume for the turbulent quantities. Flux boundary conditions for such quantities are then prescribed on the *inner* faces of the boundary volumes. BURCHARD AND PETERSEN [30] demonstrated that, due to the strong gradients of some turbulent quantities near the "wall", such models may become very inaccurate if prescribed (or Dirichlet) boundary conditions are used. For this reason, the above authors recommended to generally use flux boundary conditions for the turbulent quantities.

Alternatively, grid "B" illustrated in Fig. 5.1 assumes the "wall" at the *outer* face of the boundary volume. It was hoped, that by using this method, the difficulty with the Dirchlet boundary conditions could be avoided. It turned out that this was indeed the case but, unfortunately, now the flux boundary conditions could not accurately be described with a reasonable grid resolution. So the net gain is, say, relative. The recommendation of BURCHARD AND PETERSEN [30], to generally use only flux boundary conditions, is apparently valid only for their special (though popular) type of grid. Since boundary conditions for turbulent quantities are almost always based on asymptotic profile assumptions (see Appendix A.1), it seems to be a matter of taste, which grid is preferred. A collocated grid, which describes all variables at the same positions would probably provide a solution to the boundary face problem. Even though there are a number of industrial applications of the FV method on collocated grids (see FERZIGER AND PERIĆ [74]), they seem to be largely ignored in oceanography.

The discretized equations for $\dot{\varphi}$, (5.3), and the boundary conditions, (5.5) and (5.6), can be conveniently re-written in the form

$$\dot{\varphi}_i = K_{ij}\varphi_j + r_i \quad . \tag{5.8}$$

The vector r_i is then given by

$$r_i = \begin{pmatrix} \frac{F_0^l \delta_0}{m_0^c} q_0 + \frac{1}{m_0^c} S_0 \\ \cdots \\ \cdots \\ \frac{1}{m_i^c} S_i \\ \cdots \\ \cdots \\ \frac{F_N^u \delta_{N+1}}{m_N^c} q_{N+1} + \frac{1}{m_N^c} S_N \end{pmatrix} \quad , \tag{5.9}$$

where q_0 and q_{N+1} denote the fluxes of φ at the lower and upper volume faces, respectively. For a simple diffusion equation with source terms, as it is considered here, the spatial

discretization leads to a tri-diagonal matrix of the form

$$
K_{ij} = \begin{pmatrix}
-\ F_0^u \dfrac{k_1^f}{m_0^c} \\ +\ \dfrac{1}{m_0^c} L_0 & F_0^u \dfrac{k_1^f}{m_0^c} & 0 & 0 & 0 \\[2em]
\dots & \dots & \dots & \dots & \dots \\[2em]
0 & F_i^l \dfrac{k_i^f}{m_i^c} & \begin{matrix} -\ F_i^l \dfrac{k_i^f}{m_i^c} - F_i^u \dfrac{k_{i+1}^f}{m_i^c} \\ +\ \dfrac{1}{m_i^c} L_i \end{matrix} & F_i^u \dfrac{k_{i+1}^f}{m_i^c} & 0 \\[2em]
\dots & \dots & \dots & \dots & \dots \\[2em]
0 & 0 & 0 & F_N^l \dfrac{k_N^f}{m_N^c} & \begin{matrix} -\ F_N^l \dfrac{k_N^f}{m_N^c} \\ +\ \dfrac{1}{m_N^c} L_N \end{matrix}
\end{pmatrix}
\tag{5.10}
$$

where the dots mark omitted lines in the matrix. Here, (5.9) and (5.10) are formulated for turbulent quantities on grid "B". For mean flow quantities on grid "A", N has to be replaced by $N - 1$ in these equations, which remain unchanged otherwise.

5.2 Discretization of Non-Negative Variables

Turbulence models have to insure that certain turbulent parameters, which are non-negative by definition, cannot assume values smaller than zero. Examples are the diagonal elements of the Reynolds stress tensor and their sum, the rate of dissipation ϵ, the turbulent length scale l, and the turbulent frequency ω. In addition, if the condition $\varphi \geq 0$ is satisfied *identically*, the relation

$$
\dot{\varphi} > 0 , \quad \text{if} \quad \varphi = 0
\tag{5.11}
$$

has to hold. Models that conform to these conditions are usually referred to as realizable.

Clearly, a numerical scheme should preserve the realizability of the physical model. If a non-negative variable is discretized according to (5.3), this requirement leads to the following consideration: If it is assumed, that φ_i approaches zero at a single grid point,

(5.3) reduces to

$$\dot{\varphi}_i = F_i^u \frac{k_{i+1}^f}{m_i^c} \varphi_{i+1} + F_i^l \frac{k_i^f}{m_i^c} \varphi_{i-1} + \frac{1}{m_i^c} S_i \quad . \tag{5.12}$$

Then, since all quantities on the right hand side of this equation, except S_i, are either positive or zero by definition, a necessary condition for numerical realizability, analogous to (5.11), is

$$S_i > 0 \quad . \tag{5.13}$$

PATANKAR [189] arrived at the same result, however, with a different argument.

There is another requirement for the numerical scheme, which is not only related to non-negative variables. Assuming that the variable φ is stationary, (5.3) simplifies to

$$\left(F_i^u \frac{k_{i+1}^f}{m_i^c} + F_i^l \frac{k_i^f}{m_i^c} - \frac{1}{m_i^c} L_i \right) \varphi_i = F_i^u \frac{k_{i+1}^f}{m_i^c} \varphi_{i+1} + F_i^l \frac{k_i^f}{m_i^c} \varphi_{i-1} + \frac{1}{m_i^c} S_i \quad . \tag{5.14}$$

PATANKAR [189] remarked in this context that for given grid geometry, diffusivity and source terms, on physical grounds, the value of φ_i should increase if one or both of the neighbour values increase. This argument leads to the necessary condition

$$L_i < 0 \quad . \tag{5.15}$$

A violation of this condition can lead to a fatal feedback between an increasing value of φ_i and an increasing contribution of the linear source term.

To insure (5.13) and (5.15), PATANKAR [189] suggested to split the source term of a non-negative variable in a positive and a negative contribution, S_i^{pos} and S_i^{neg}, respectively, and set

$$S_i = S_i^{\text{pos}} \,, \quad L_i = \frac{S_i^{\text{neg}}}{\varphi_i^*} \,, \tag{5.16}$$

where φ_i^* is the current value of the φ_i, either from the last time-step or from the last iteration (see below).

5.3   Discretization of the Boundary Conditions

Since some mean and turbulent quantities exhibit strong gradients when approaching a rigid wall (see Appendix A.1), care must be observed in discretizing the boundary conditions. An example is the velocity in the logarithmic region of the law-of-the-wall

in the bottom boundary layer, which behaves according to (A.10). This equation is re-written here for the velocity u_b^c at the lowest grid point, z_b^c, as

$$u_b^c = \frac{u_*}{\kappa} \ln \left(\frac{z_b^c + z_0}{z_0} \right) , \qquad (5.17)$$

where z_0 denotes the roughness length of the sediment. Using the relationship $u_*^2 = -\tau_b/\rho$ with the bottom momentum flux τ_b, (5.17) can be squared and solved for u_*^2 as a function of tu_b^c. In the two-dimensional case one obtains

$$\begin{aligned}
\frac{\tau_b^x}{\rho} &= -\frac{\kappa^2}{r^2} u_b^c \sqrt{(u_b^c)^2 + (v_b^c)^2} , \\
\frac{\tau_b^y}{\rho} &= -\frac{\kappa^2}{r^2} v_b^c \sqrt{(u_b^c)^2 + (v_b^c)^2} ,
\end{aligned} \qquad (5.18)$$

where τ_b^x and τ_b^y denote the shear stresses in the x and y directions at the bottom, respectively, and

$$r = \ln \left(\frac{z_b^c + z_0}{z_0} \right) . \qquad (5.19)$$

Other authors (e.g. BAUMERT AND RADACH [12]) pointed out that the FV method is based on an integral average of variables in a finite volume, and hence for the evaluation of this average advantage should be taken of the known profiles in the logarithmic region. The average of the velocity in the lowest volume is defined by

$$\overline{u}_b = \frac{1}{\Delta_b} \int_{z_b^f}^{z_b^f + \Delta_b} u(z) \, dz , \qquad (5.20)$$

where Δ_b is the height, and z_b^f the position of the lower face of the lowest volume. An explicit expression for $\overline{u}_b$ can be obtained by integrating (A.10) over the lowest volume. If now, in the spirit of the FV method, u_b^c is identified with this average, expressions identical to (5.18) are obtained. However, the factor r is now defined as

$$r = \ln \left[\frac{1}{e} \left(1 + \frac{1}{p} \right)^{p+1} \frac{z_0 + z_b^f}{z_0} \right] , \qquad p = \frac{z_0 + z_b^f}{\Delta_b} . \qquad (5.21)$$

This equation generalizes previous results, since it applies to all kinds of boundary volumes, provided the boundary volume is entirely inside the logarithmic flow region[3].

Analogously, the rate of dissipation at the center of the lowest volume can be either computed directly from $(A.6)_1$,

$$\epsilon_b^c = (c_\mu^0)^3 \frac{k^{\frac{3}{2}}}{\kappa(z_b^c + z_0)} , \qquad (5.22)$$

---

[3]In the context of dynamical boundary layers in lakes (see Section 4.2), this implies that $z_b^f + \Delta_b$ should be considerably smaller than $1\,\mathrm{m}$.

or by identifying the value of ϵ_b^c with the average value of ϵ in the lowest volume,

$$\overline{\epsilon}_b = \frac{1}{\Delta_b} \int_{z_b^f}^{z_b^f + \Delta_b} \epsilon(z)\, dz \quad . \tag{5.23}$$

If this integral is solved for the known profile of ϵ in the logarithmic part of the law-of-the-wall, $(A.6)_1$, $\overline{\epsilon}_b$ can be obtained from

$$\overline{\epsilon}_b = \frac{(c_\mu^0)^3 k^{\frac{3}{2}}}{\kappa(z_0 + z_b^f)} \ln\left(1 + \frac{1}{p}\right)^p \ , \tag{5.24}$$

where the geometrical quantities p and z_b^f have already been defined in the context of (5.21).

Similar considerations lead also to an expression for the value of ω in the lowest volume. It turns out, however, that both, the direct and the volume averaged versions of the boundary conditions yield almost identical results for the numerical grids used here. Even though both alternatives are available in the program code, it is recommended thus to use the direct evaluation from the law-of-the-wall relations, since the computational costs are slightly smaller.

5.4   Time-Stepping Schemes

The spatial discretization of (5.1) with a FE or FV method leads to a linear system of first order differential equations for the variable φ of the form

$$\boldsymbol{M}\dot{\boldsymbol{\varphi}} = \boldsymbol{K}^*\boldsymbol{\varphi} + \boldsymbol{r}^* \ , \tag{5.25}$$

where $\boldsymbol{M}$ and $\boldsymbol{K}^*$ are usually referred to as the mass matrix and the coefficient matrix, respectively. $\boldsymbol{r}^*$ is the vector of the right hand sides. If a FE method is used, the mass matrix, emerging from the spatial discretization of the left hand side of (5.1), is in general not strictly diagonal[4]. There are, however, techniques to diagonalize $\boldsymbol{M}$ (see REDDY [198]). If a FV discretization is adopted, the resulting mass matrix is always diagonal. In such cases, $\boldsymbol{M}$ can easily be inverted and (5.25) is immediately re-written as

$$\dot{\boldsymbol{\varphi}} = \boldsymbol{M}^{-1}\left(\boldsymbol{K}^*\boldsymbol{\varphi} + \boldsymbol{r}^*\right) = \underbrace{\boldsymbol{K}\boldsymbol{\varphi} + \boldsymbol{r}}_{\boldsymbol{R}} \ , \tag{5.26}$$

---

[4]In most cases, the mass matrix will be banded with small bandwidth.

where in the last step the inverse (also diagonal) mass matrix, $\boldsymbol{M}^{-1}$, was absorbed into the new coefficient matrix, $\boldsymbol{K}$, and the new vector $\boldsymbol{r}$. Then, (5.26) is identical to (5.8) derived above.

(5.26) is advanced in time with a generalized multi-step method, written down here for an equidistant time-step, Δt, in the form

$$
\begin{aligned}
\boldsymbol{\varphi}^{t+1} &= \alpha_0 \boldsymbol{\varphi}^t + \alpha_1 \boldsymbol{\varphi}^{t-1} + \alpha_2 \boldsymbol{\varphi}^{t-2} + (\ldots) \\
&+ \Delta t \beta_{\text{impl}} \boldsymbol{R}^{t+1} + \Delta t \beta_0 \boldsymbol{R}^t + \Delta t \beta_1 \boldsymbol{R}^{t-1} + (\ldots) ,
\end{aligned}
\tag{5.27}
$$

where $\boldsymbol{\varphi}^{t+i} := \boldsymbol{\varphi}(t + i\Delta t)$ and $\boldsymbol{R}^{t+i} := \boldsymbol{R}(t + i\Delta t, \boldsymbol{\varphi}(t + i\Delta t))$. For $\beta_0, \beta_1, \ldots = 0$ the so-called implicit backward differencing formulae (BDF) are obtained. On the other hand, for $\alpha_0 = 1$ and $\alpha_1, \alpha_2, \ldots = 0$ some well-known quadrature-based implicit methods can be recovered (TÖRNING AND SPELLUCCI [269]). In the latter case, (5.27) can be re-arranged as

$$
\begin{aligned}
\left(\boldsymbol{K}^{t+1} - \frac{1}{\beta_{\text{impl}} \Delta t} \boldsymbol{I} \right) \boldsymbol{\varphi}^{t+1} &= -\boldsymbol{r}^{t+1} - \frac{1}{\beta_{\text{impl}} \Delta t} \boldsymbol{\varphi}^t - \frac{\beta_0}{\beta_{\text{impl}}} \underbrace{\left(\boldsymbol{K}^t \boldsymbol{\varphi}^t + \boldsymbol{r}^t \right)}_{\boldsymbol{R}^t} \\
&- \frac{\beta_1}{\beta_{\text{impl}}} \underbrace{\left(\boldsymbol{K}^{t-1} \boldsymbol{\varphi}^{t-1} + \boldsymbol{r}^{t-1} \right)}_{\boldsymbol{R}^{t-1}} - (\ldots) ,
\end{aligned}
\tag{5.28}
$$

where use was made of the definition of $\boldsymbol{R}$ in (5.26). Parameters for the schemes implemented in the numerical code are given in Tab. 5.1.

	β^{impl}	β_0	β_1
Euler (Backward)	1	0	0
Trapezoidal Rule	$\frac{1}{2}$	$\frac{1}{2}$	0
Adams-Moulton (2nd order)	$\frac{5}{12}$	$\frac{8}{12}$	$-\frac{1}{12}$

Table 5.1: Coefficients of different multi-step methods based on quadrature according to (5.28).

Clearly, $\boldsymbol{K}^{t+1}$ and $\boldsymbol{r}^{t+1}$ in (5.28) depend on $\boldsymbol{\varphi}^{t+1}$. Hence (5.28) is in general a non-linear system that can only be solved iteratively. Here, the equations for the different mean flow and turbulent quantities are solved successively and due to their non-linear coupling, the time-step has to be reduced to small values for reasons of accuracy. Since the computational cost for one iteration is not much smaller than that for a complete time-step, no advantage was felt in using an iteration procedure (even though it was

implemented). Instead, it is recommended to apply a simplified, quasi-implicit scheme of the form

$$
\begin{aligned}
\left(\boldsymbol{K}^t - \frac{1}{\beta_{\mathrm{impl}}\Delta t}\boldsymbol{I}\right)\boldsymbol{\varphi}^{t+1} \;=\;& -\boldsymbol{r}^t - \frac{1}{\beta_{\mathrm{impl}}\Delta t}\boldsymbol{\varphi}^t - \frac{\beta_0}{\beta_{\mathrm{impl}}}\underbrace{\left(\boldsymbol{K}^t\boldsymbol{\varphi}^t + \boldsymbol{r}^t\right)}_{\boldsymbol{R}^t} \\
& - \frac{\beta_1}{\beta_{\mathrm{impl}}}\underbrace{\left(\boldsymbol{K}^{t-1}\boldsymbol{\varphi}^{t-1} + \boldsymbol{r}^{t-1}\right)}_{\boldsymbol{R}^{t-1}} \;-\; (\ldots)\,,
\end{aligned}
\tag{5.29}
$$

which can be solved directly, since $\boldsymbol{K}^t$ and $\boldsymbol{r}^t$ (and hence also the boundary conditions) are evaluated at the current time-level. In other words: The time-step is also the iteration-step.

5.5   Numerical Performance

To investigate the numerical robustness of the k-ϵ model and the k-ω model, a few very brief tests are shown here. Since both models perform quite similarly in stably stratified flows, all tests reported here deal with unstratified situations. It turned out, surprisingly, that in such situations the k-ω model exhibits a behavior very different (and very undesirable) compared to the k-ϵ model under certain circumstances.

First, the shear-driven unstratified entrainment experiment of Fig. 5.2 is considered. The parameters given in this figure correspond to a situation typical for an unstratified lake in winter, 6 hours after the onset of a wind of medium strength. Three different types of numerical grids have been used: 1.) A very fine grid with a resolution of $0.2\,\mathrm{m}$ and additional zooming at the boundaries. This is probably the finest resolution a three-dimensional model allows for at present. 2.) A *homogeneous* grid of the same resolution 3.) A coarse homogeneous grid with a resolution of $2\,\mathrm{m}$.

It is apparent from Fig. 5.2 that in the largest part of the mixing layer the grid resolution plays only a marginal role. Especially notable is the fact that both models deal very well with the strong velocity gradients close to the surface. However, some differences are visible close to the entrainment region. There, a coarser grid leads to deeper entrainment. The k-ϵ model performs slightly better than the k-ω model.

Differences between the models become more obvious from profiles of the turbulent diffusivity of momentum, as displayed in Fig. 5.3. In contrast to the k-ϵ model, the k-ω model exhibits considerable differences between the diffusivity computed with the fine grid and that computed with the fine, zooming grid in a large part of the mixing layer.
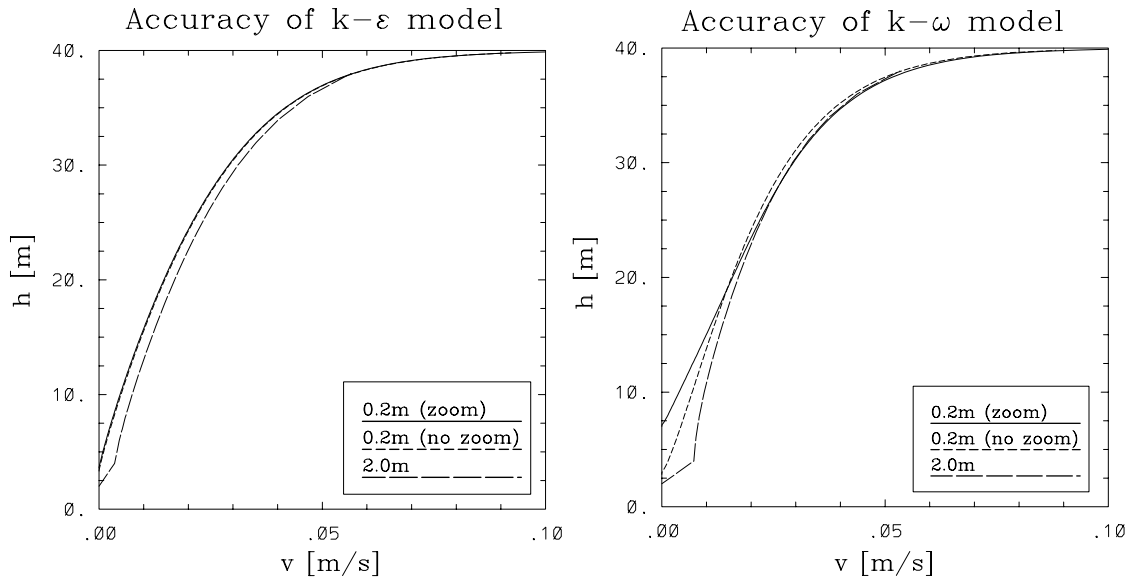
Figure 5.2: Velocity at height, h, after 6 hours of entrainment in an unstratified fluid, driven by a constant surface stress, for different grid resolutions. "Zoom" refers to a grid with higher resolutions at the boundaries. Left panel: k-ϵ model. Right panel: k-ω model. $z_0 = 10^{-3}$ m, $u_* = 6 \cdot 10^{-3}$ ms^{-1}, $\omega_{\min} = 10^{-3}$ s^{-1}.
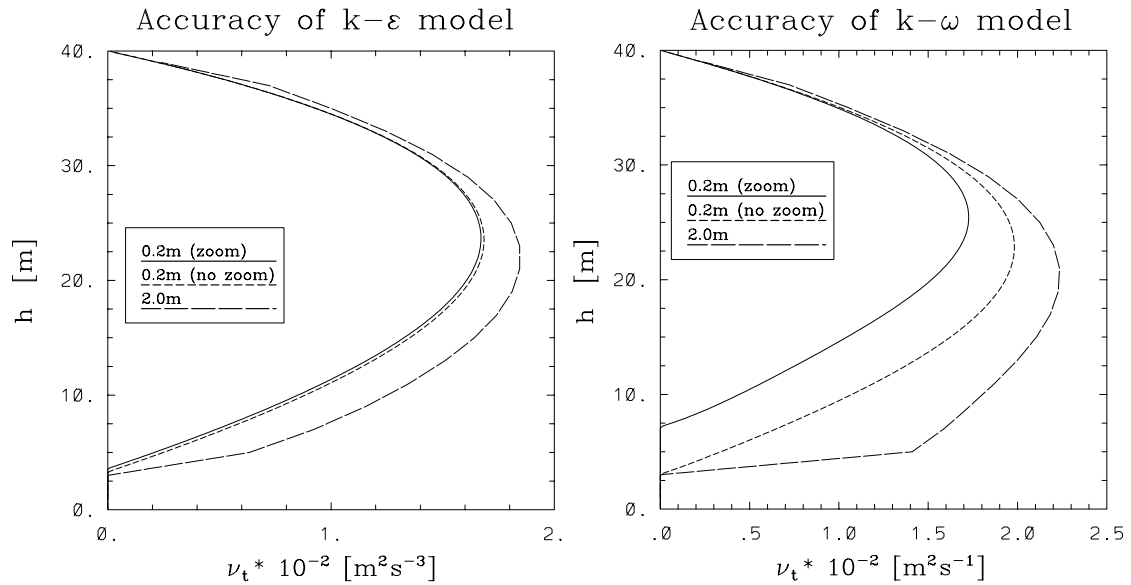
Figure 5.3: Same as Fig. 5.2, but now for the turbulent diffusivity, ν_t.

The situation is even worse with the coarse grid: Compared to the finest grid, the k-ω model predicts deviations of more than a factor of three in some parts of the mixing layer. The deviations of the k-ϵ model, though also considerable, are much smaller in this case.

The most serious problem with the k-ω model in unstratified entrainment situations is,

however, caused by its sensitivity to the value of ω prescribed in the quiescent region below the entrainment layer. In numerical codes very small values for the turbulent quantities have to be prescribed in this region in order to avoid divisions by zero. If these values are made small enough, their effect on turbulent quantities in the mixing layer and, in particular, on the entrainment depth should be felt neither in stratified nor in unstratified entrainment situations. Indeed, this behavior is corroborated by the computed results of the k-ϵ model in all cases (not shown). Unfortunately, however, the k-ω model is extremely sensitive with respect to the value of ω_{min} prescribed in the quiescent region below the mixing layer. Fig. 5.4 reveals that the maximum value of the turbulent diffusivity and the entrainment depth are strong functions of ω_{min}. It is thus impossible to fix the "real"

Accuracy of k−ω model
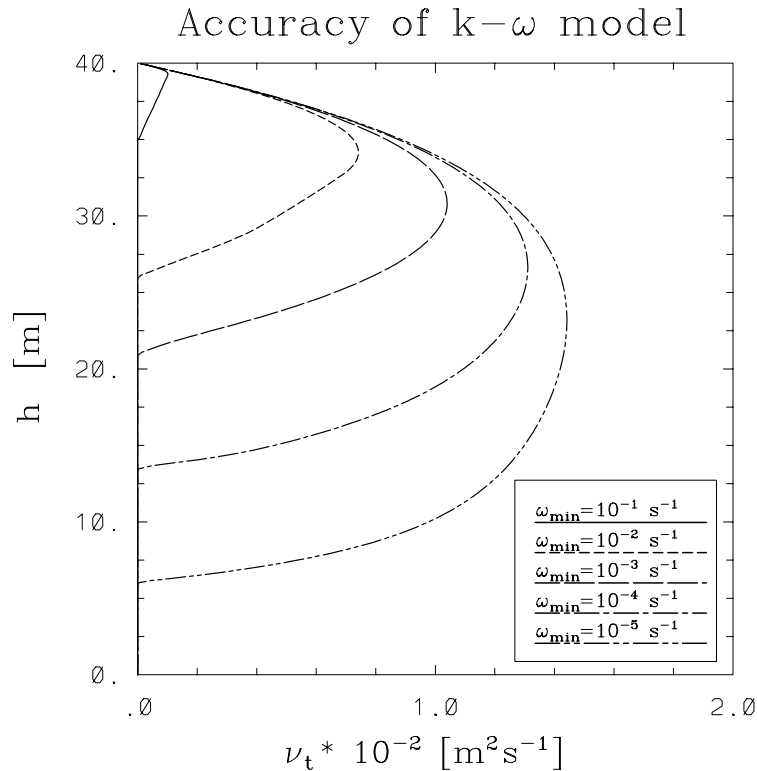
Figure 5.4: Same as Fig. 5.3, but now after 3 hours shear entrainment with the high resolution zoomed grid and different values for ω_{min}. Only the k-ω model is displayed.

entrainment depth predicted by this model. In fact, for the computations of Fig. 5.2 and Fig. 5.3 the value of ω_{min} has been adjusted for the k-ω model to predict an approximately equal entrainment depth as the k-ϵ model.

Even though it is not shown here, a very similar problem also appears in unstratified, *shear-free* entrainment situations. Moreover, the sensibility of the k-ω model with respect to ω_{min} seems not to be a numerical problem, since the effect appeared also for the

finest grid resolution. Note, that no comparable complications appear in the stratified case. Then, the value of $\omega_{\min}$ can be chosen as small as desired and, in fact, the k-ω models appears to be even somewhat more robust than the k-ϵ model. Nevertheless, the theoretical superiority of the k-ω model, illustrated in the preceeding chapters, is overshadowed by this numerical problem and the universal applicability of the k-ω model has to await a solution.

Chapter 6

Object-Oriented Programming Techniques in Turbulence Modelling

6.1 Introduction

Most institutions involved in scientific computation projects have to face a considerable consumption of man-power, devoted to the search for subtle errors in complicated and large programs. This fact should neither be considered a fate nor a consequence of incompetent staff. It should rather be accepted that complex, large-scale numerical software can only be developed, maintained, and extended at extravagant expenses, because of the fact that most often antiquated structural programming languages like FORTRAN are applied. Even though in particular FORTRAN has undergone a considerable evolution during the past decades (see DUBOIS [66]), compatibility requirements with early versions of this language prohibit the elimination of many of its deficiencies, namely its low level of abstraction, its restricted type-safety, and its limited re-usability.

As an answer to the inherent problems of structural languages in large software projects, a number of so-called object-oriented languages with a high level of abstraction appeared. Because of its compatibility with the very popular structural language C, it was in particular C++, developed by STROUSTRUP [248], that attracted considerable interest in the scientific computing community since about a decade (WONG ET AL. [296], STEINER ET AL. [245]). Even though the advantages of using this language in scientific computing have been illustrated many times and numerous successful techniques are known (see e.g. BARTON AND NACKMAN [8]), the advocators of structural languages tenaciously produce

two apparently timeless arguments against it: "C++ is too complicated" and "C++ is too slow for scientific computing".

To reply to the former statement, one first needs to find an agreement about what the stereotype *complicated* means in this context. Of course, there is little doubt that C++ will appear *complicated* to a FORTRAN programmer, simply due to the fact that it is *different* from FORTRAN (and, admittedly, since its grammar and semantics are somewhat more extensive). On the other hand, however, I am convinced that the formulation of any complex mathematical model in terms of an abstract and truly object-oriented computer language is much more *readable* and *understandable* (and hence exactly *not complicated*) compared to FORTRAN or any other structural language[1]. Scientific computing has become computational science, and as within any other scientific field it is evident that a higher level self-contained theory opens up new vistas and new understanding from a different and elevated point of view[2]. In terms of computer languages this statement expresses the fact that "language shapes the way we think and determines what we can think about" (STROUSTRUP [248]).

The second statement, "C++ is not fast enough", indicates that speed may be an important issue for some scientific applications. A couple of interesting investigations upon this topic have been conducted and, in fact, less than a decade ago, HANEY [98] had to state that speed differences between C++ programs for typical numerical matrix operations and similar programs written in C or FORTRAN "may be uncomfortably large". The evolution of compiler technology and class design, however, advanced extremely fast, and a couple of years later this and other authors pointed out that C++, even though allowing for a high level of abstraction, now also was able to retain a reasonable run-time efficiency (HANEY [99], ROBINSON [204], HANEY AND CROTINGER [100]). Since then, many scientists were drawn to C++, since it offers the possibility to translate physical models and mathematical expressions more directly into readable and maintainable code. It is thus no wonder that a drastically increasing number of object-oriented scientific software could be observed, an impressive example being the Finite-Element method: Even though first object-oriented approaches to this method were reported not before the early 1990's (see MACKIE [158]), today the reference list of the last few years alone fills several pages (MACKERLE [157]).

---

[1]Readers sceptical about this statement should risk the trauma of having a look in the FORTRAN source code of a large-scale Finite-Element program.

[2]A more practical argument for studying object-oriented languages could be added: It takes typically one week to either study a standard text book on object-oriented techniques or to find an intricate memory segmentation fault in a large-scale numerical FORTRAN code.

A couple of object-oriented multi-purpose frameworks for efficient numerical computations are known[3], but only few suggestions have been reported specifically for computational fluid dynamics and, in particular, for turbulence modelling. Here, an object-oriented approach to turbulence modelling, using state-of-the-art object-oriented techniques is attempted. This chapter may also be perceived as part of a manual for the numerical software.[4]

6.2   Basic Concepts

The mathematical models developed in the preceeding chapters were translated to an object-oriented design using the programming language C++ (STROUSTRUP [248]). In this chapter, however, the object-oriented framework will be expressed in terms of the so-called Unified Modeling Language (UML). Even though developed only recently (see BOOCH ET AL. [18]), UML has already become a standard for the specification and visualization of object-oriented concepts *independent of the actual programming language.* UML was chosen, since the basic principles of this meta-language are easy to grasp and even readers with little or no background in object-oriented design will be able to follow through the text, at least to some degree.

The development and testing of the numerical software presented here would not have been possible in the short time that was available without the extensive use of existing libraries. Generic lists, vectors and countless other utilities were provided by the Standard Template Library (STL), an object-oriented package that was so successful in the past, that it is sometimes considered a native part of C++ now (STROUSTRUP [248]). Matrix operations were based on the object-oriented Matrix Template Library (MTL), a very fast, generic tool developed recently by SIEK AND LUMNSDAINE [226]. It appears to be probable, that this library will also become a standard like the STL in the near future. Since MTL is still in development, suitable capabilities for the inversion of matrices were not yet available. Instead, matrix inversions were performed by using the LAPACK library (see ANDERSON ET AL. [5]). LAPACK contains more than 500 000 lines of excellently tested and established FORTRAN code for all types of matrix manipulations.

---

[3]The POOMA project, initiated at the Los Alamos National Laboratory (LANL), is an excellent example of an object-oriented framework for applications in computational science requiring high-performance parallel computers. (see `http://www.acl.lanl.gov/PoomaFramework/index.html`)

[4]Readers not familiar with object-oriented programming are encouraged to continue reading. It is the purpose of object-oriented techniques to make things easier or at least to make difficulties apparent. Thus, many of the concepts outlined below are intuitively comprehendible, even with little or no experience.

It would have been a dogmatic re-invention of the wheel not to use these facilities. The FORTRAN routines were wrapped in C++ interfaces in order to make them accessible for more abstract operations in a manner described in BARTON AND NACKMAN [8]. Hence, most low-level operations are executed in FORTRAN, and a possible performance penalty of C++ (see above) could be excluded from the outset.

6.3   A Simple Class

As with any other language, object-oriented languages have their own grammar and vocabulary and their own conventions and definitions. It is evident that this section cannot replace a textbook on object-oriented techniques, and thus the descriptions given here should be perceived as working conventions, rather than as the precise definitions given by the creators of UML and C++.

First, it should not come as a surprise that object-oriented methods deal with objects. In the context of objects, the following useful working definitions apply:

- Objects with common *attributes* and *operations* can be grouped into *classes*. New classes introduce new *types*, extending the built-in types like `int` (for integers) or `float` (for floating point numbers).

- Attributes of a class describe the *properties* of its objects or, in other words, *what its objects consist of.*

- Operations of a class describe the *behavior* of its objects, or, in other words, *what one can do with its objects.*

- All objects of a class have the same attributes, but the attributes of each object can adopt different *values*. The values of all attributes of an object collectively define its *state*.

Fig. 6.1 explains the above definitions by means of the simple class `LinearSystem`, which is actually part of the class library developed here. This figure illustrates that a class is depicted in UML as a rectangle with three compartments divided by horizontal lines[5]. The name of the class is found in the upper compartment, the attributes in the middle,

```
                                    ┌ ─ ─ ─ ─ ─ ─ ┐
                                    ¦ T_Matrix   ¦
                                    ¦ T_Vector   ¦
              ┌─────────────────────└ ─ ─ ─ ─ ─ ─ ┘
              │      LinearSystem              │
              ├───────────────────────────────┤
              │ -a: T_Matrix                  │
              │ -x: T_Vector                  │
              │ -b: T_Vector                  │
              ├───────────────────────────────┤
              │ +getA()                       │
              │ +getX()                       │
              │ +getB()()                     │
              │ +setColumn()                  │
              │ +setRow()                     │
              │ +solveYourself()              │
              │ +printYourself()              │
              └───────────────────────────────┘
```
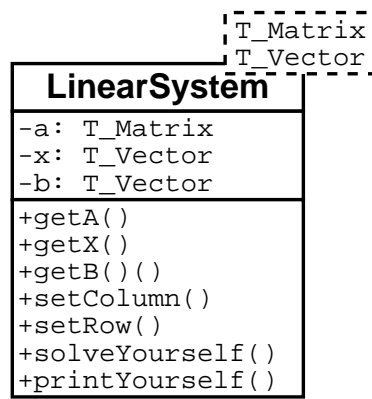
Figure 6.1: Class `LinearSystem`, used to assemble and solve a linear system.

and the operations in the lower compartment.

As shown in Fig. 6.1, the attributes of the class `LinearSystem` are the following objects:
The matrix, `a`, the vector of the unknowns, `x`, and the vector of right hand side, `b`. In
accordance with

$$Ax = b \, , \tag{6.1}$$

this is what most readers perceive a linear system should consist of[6].

The type of each attribute is depicted after a colon to the right of the object's name.
E.g., the type of the matrix, `a`, is recognized to be `T_Matrix`. However, no information
so far was given about what properties and what behavior objects of the type T_Matrix
should have and, in fact, this was no coincidence: There are many different types of
matrices known in mathematics (e.g. tridiagonal, sparse, banded, symmetric, ...), and
the `LinearSystem` should be usable with all of the them. To make the `LinearSystem`
independent of the actual type of the matrix, use of *template parameters* was made, a
very powerful feature of C++. With this technique, the desired type of the matrix, `a`,
can be given as an additional parameter from outside the class. Template parameters are
depicted in UML as character strings in a small rectangle in the upper right corner of the
class. Indeed, the type of the matrix, `a`, is seen to coincide with the name of the template
parameter, `T_Matrix`. Any matrix type that can be generated with the MTL library can
be substituted for the template parameter. The same arguments apply to the type of the
vectors `x` and `b`, called `T_Vector`. Besides matrices, there are also several different vector

---

[5]The little rectangle in the upper right corner is a UML convention for the specification of so-called
"template parameters". This is discussed below.

[6]Note, that object names are generally written uncapitalized in UML. This is the reason, why "`a`"
was used instead of the capital "`A`" as in (6.1).

types that can be generated with the MTL library.

As remarked above, the operations of the class `LinearSystem` are depicted in the lower compartment of the class diagram in Fig. 6.1. These operations define what one can do with an object of this class. The first operation, `getA()`, makes the elements of the matrix, `a`, accessible. If it is called with two arguments[7], describing the row and the column number of the matrix, `a`, it will return the appropriate matrix element. Clearly, this operation is crucial for the element-wise assembly of the global coefficient matrix in any numerical scheme. Similar operations follow, granting access to other parts of the linear system, e.g. to the vector of the unknowns, `x`, and the vector of the right hand sides, `b`. Also provided are operations allowing for the assignment of values to complete columns and rows of the matrix (`getColumn()`, `getRow()`).

The operation `solveYourself()` executes the solution of the `LinearSystem` after the matrix and the right hand side have been assembled. Without going into detail, it should be pointed out that this operation recognizes the type of the matrix, `a`, chooses an appropriate solver and solves the system. This is consistent with the perception that the way, in which a linear system is solved, should depend only on the type of its matrix. Currently, direct solvers for several standard matrix types from the LAPACK library (written in FORTRAN), but also some iterative solvers from the MTL library, are provided. `LinearSystem` is thus a very flexible class that can be used with any object-oriented numerical code.

6.4   The Abstraction of a Transport Equation

It was illustrated in Chapter 5, that the general transport equation (5.1) can be discretized in form of the linear system (5.29). Now, the problem has to be attacked, how this procedure can be abstractly expressed in an object-oriented vocabulary.

An appropriate class, `Transport_1D`, is presented in Fig. 6.2. This class contains all information about the geometry, the assembly of the linear system, the boundary conditions and the numerical time-stepping method. The knowledge about the numerical grid and the spatial discretization (e.g., how to compute gradients of a grid variable) has been delegated to the first attribute of `Transport_1D`, an object called `geom`. The type of this object is determined by the template parameter `T_Geometry` in a way outlined above.

---

[7]For clarity, the arguments of most operations have been omitted here.

With this method, `Transport_1D` will be usable with different types of discretization techniques, depending on the class, which the object `geom` belongs to. One particular class, `FV_Geometry` (not shown), was developed here to implement the Finite-Volume method introduced in Chapter 5. Other geometry classes, for example a class called `FE_Geometry` implementing a Finite-Element method, could be developed and substituted.

```
                                                      ┌ ─ ─ ─ ─ ─ ─ ─ ┐
                                                      ¦ T_Geometry    ¦
┌─────────────────────────────────────────────────── └ ─ ─ ─ ─ ─ ─ ─ ┘──┐
│                      Transport_1D                                        │
├──────────────────────────────────────────────────────────────────────┤
│ -geom: T_Geometry                                                       │
│ -ls: LinearSystemType                                                    │
├──────────────────────────────────────────────────────────────────────┤
│ +discretizeYourself()                                                    │
│ +setLowerBoundaryFlux()                                                  │
│ +setUpperBoundaryFlux()                                                  │
│ +setGridValue()                                                          │
│ +doTimestepOn(v:EulerVariableType,dt:ValueType)                          │
│ +doTimestepOn(v:TrapezoidalVariableType,dt:ValueType)                    │
│ -solveLinearSystem()                                                     │
└──────────────────────────────────────────────────────────────────────┘
```
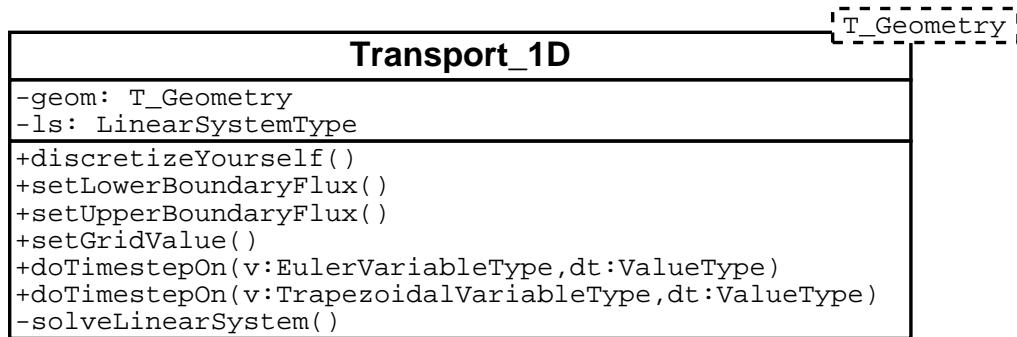
Figure 6.2:   Class `Transport_1D`, used to discretize the one-dimensional transport equation.

The second attribute of `Transport_1D` is the object `ls` of type `LinearSystemType`. This type has to correspond to some variant of the class `LinearSystem` introduced above. The types of the template parameters of this class, `T_Matrix` and `T_Vector`, have to be "known" by the geometry class of type `T_Geometry`, because the structure of the matrix follows directly from its discretization. The Finite-Volume method, e.g., leads to tridiagonal matrices (see Chapter 5) and hence the class `FV_Geometry` must store type information about a tridiagonal matrix from the MTL library, used to replace the template parameter `T_Matrix`.

The operation `discretizeYourself()` triggers the discretization of the transport equation and assembles the matrix in the linear system, `ls`. It is clear, that to this end `discretizeYourself()` has to rely heavily on the services provided by its attribute, `geom`. Other operations are provided in order to set the appropriate boundary conditions (see Fig. 6.2). More interesting are the operations performing the different types of timesteps, `doTimstepOn(...)`. One of their arguments is the field variable, `v`, supposed to be stepped forward in time. Field variables can be objects of several different classes, depending on the time-stepping scheme used to advance them in time. For the trapezoidal time-step, e.g., the object `v` will be of type `TrapezoidalVariableType`. Class diagrams for the different variable types are not given here, but without going into much detail, it should be noted that the variable, `v`, does not only provide storage for the actual grid values, but also for the right hand sides of the linear system at past time-steps, i.e. $\boldsymbol{R}^t$,

$\boldsymbol{R}^{t-1}$, ... in (5.29). As explained in the context of this equation, the number of right hand sides to be stored depends on the time-stepping procedure. Since the right hand sides contain information about the "history" of the variable, it was felt that the most appropriate place for them was in the object, `v`, itself[8].

The operation `doTimestepOn(...)` automatically recognizes the type of the variable in its argument and performs the corresponding time-step. At the end of each time-step, when the matrix and the right hand side are assembled, `doTimestepOn(...)` calls `solveLinearSystem()`, which in turn calls the operation `solveYourself()` of the attribute `ls` (the linear system, see above).

6.5   The Class Structure of Turbulence Models

It was illustrated in Chapter 2 that the Reynolds decomposition of turbulent fields leads to ensemble averaged variables describing the *mean flow*, and, on the other hand, to a number of statistical quantities describing the properties of the *turbulence*. The evolution of the mean flow is determined by the *Reynolds Averaged Navier Stokes equations (called RANS in the following)*, and the turbulence is described by a *turbulence model*. Note, that in these two sentences the essential vocabulary (written in *italic* style) of an appropriate class structure has already been spelled in a natural way.

Fig. 6.3 depicts the main classes and their relations. Class diagrams for the classes `MeanFlow` and `Turbulence`, introduced in this figure, are not given here. However, their structure is very simple, since they consist primarily of several field variables (of type `T_Variable`, see above) expressing the mean flow and turbulent fields. Among them are the different velocity components, the temperature, but also the turbulent diffusivities, and the turbulent correlations. The operations of the classes `MeanFlow` and `Turbulence` simply give access to each of their variables.

It is seen from Fig. 6.3, that the class `RANS`, explained in detail below, is responsible for the correct time-stepping of the variables contained in an object of the class `MeanFlow`. To this end, it needs information about the `Turbulence` and about the boundary conditions of the mean flow, `MeanBCs` (this class is also not shown here). The class `TurbModel`, explained below, provides operations to compute the turbulent fields. Clearly, for these

---

[8]It would have been probably more elegant to derive each of the different classes for the variables from a common base class. However, frequently accessed abstract operations, necessarily introduced then, might have caused a critical performance drawback.
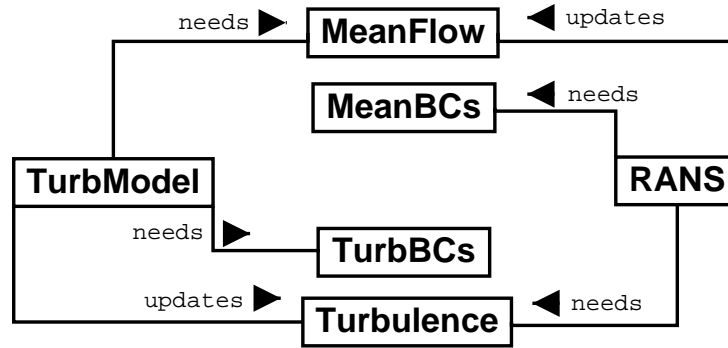
Figure 6.3: Global structure and relations of classes for the description of turbulent flow.

operations some knowledge about the `MeanFlow` and the boundary conditions for the turbulent quantities, `TurbBCs` (not shown), is required.

The purpose of an object of the class `RANS`, depicted in Fig. 6.4, is to update all variables contained in an object of the class `MeanFlow` (velocities, temperature, ...). Since the
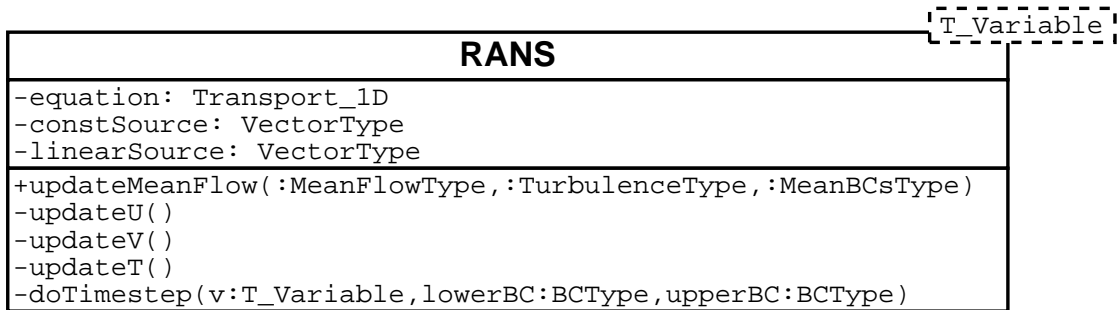
Figure 6.4: Class `RANS`, describing the Reynolds Averaged Navier-Stokes equations (RANS).

evolution of all variables is governed by the generalized transport equation, expressed by the class `Transport_1D`, an object of this type, `equation`, is found among the attributes in Fig. 6.4. The other two attributes listed in this figure, `constSource` and `linearSource`, are needed to hold the source terms of the respective variable at each time-step, e.g. the Coriolis forces for the velocity components or the radiative heat production for the temperature.

The most important operation, `updateMeanFields(...)`, performs a time-step on the mean fields. It needs, obviously, objects of the classes `MeanFlow` and `MeanBCs`, but also some information about the `Turbulence` (for example the turbulent diffusivities). This

operation will in turn call some helper operations, e.g. the operation `updateU()`, which assembles the appropriate source terms for the velocity component u and finally calls `doTimestep(...)`. The source terms will be forwarded to the object `equation` during each time-step.

6.6   The Abstraction of an Algebraic Stress Model

All parts of the general framework, shown in Fig. 6.3, have been briefly addressed so far, except the class *TurbModel*, which represents the turbulence model. However, a flexible and efficient abstraction for a turbulence model is much more difficult to find than that for the RANS, simply due to the fact that there is a large number of different turbulence models based on different structures, and all have to fit in the framework. Here, a general solution, applicable for any Algebraic Stress Model (ASM) is suggested.

The fundamental class hierarchy of such a turbulence model is illustrated in Fig. 6.5. The arrows seen in this figure denote a new fundamental relation between classes that was not encountered yet: *Inheritance* or *derivation from base classes*. Arrows point from the derived class to its base class. The class *CanutoASM*, e.g., is derived from its base class *TurbModel*. Only the most important aspects of inheritance can be mentioned here, for
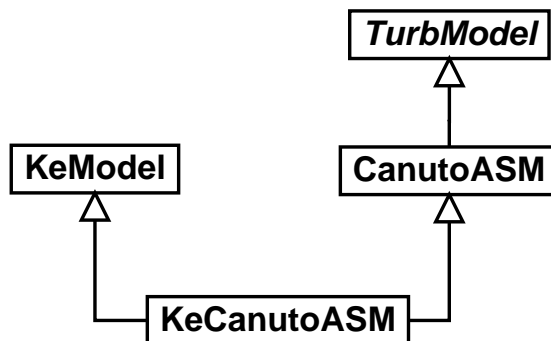
Figure 6.5:   Inheritance pattern for an Algebraic Stress Model (ASM).

a precise definition of this class relation the reader should refer to a standard text book on object-oriented techniques (e.g. STROUSTRUP [248]). The mechanisms of inheritance are governed by the following basic rules:

- *public* and *protected* attributes of a base class are *inherited* by a derived class. This means that the operations of the derived class have access to such attributes of a

base class *as if they belonged to the derived class itself.* Public attributes are denoted with the symbol "+" in UML, protected attributes with the symbol "#". *Private* attributes, denoted with the symbol "−", cannot be accessed from outside the class, not even from a derived class.

- Public and protected operations provided by a base class are also *inherited.* This means that such operations can be called with objects of a derived class *as if they belonged to the derived class itself.*

- Operations of a derived class *override* operations of a base class, if they have the same *signature*, i.e. the same name *and* the same arguments. This mechanism is known as *polymorphism.* Operations with the same name, but with different arguments are *not* overridden. Examples are provided below.

The class **CanutoASM**, shown in Fig. 6.5, refers to the ASM of CANUTO ET AL. [38] (introduced in Chapter 2). This model will serve as an example here, but it could have been replaced by any other ASM. **CanutoASM** was derived from the base class **TurbModel**, since it is semantically clear that the ASM of CANUTO ET AL. [38] *is* a turbulence model in general. On the other hand, however, it is evident from the original publication that this ASM also *is* a two-equation model, and thus should be derived from a two-equation model, say from a k-ϵ model, as well. C++ allows to resolve this apparent contradiction by a mechanism called *multiple inheritance*, allowing classes to have more than one base class: The new class KeCanutoASM is derived from both, the class **CanutoASM** and the class KeModel, which implements the functionality of a k-ϵ model. Thus, KeCanutoASM inherits all public and protected attributes and operations of both of its base classes. It will be seen below, that this class structure is a very powerful concept.

Fig. 6.6 illustrates that the base class **TurbModel** is somewhat different from the classes encountered above: First, it does not contain any attributes. Second, its operations are written *slanted*, an UML convention for *abstract* operations[9]. Abstract operations do not implement any functionality and have to be overridden by operations of the same signature (see above) in one of the derived classes, which actually implement a functionality. It is evident, that no meaningful objects can be created from a class that has only abstract operations and no attributes. Such classes are referred to as *abstract* classes, their names conventionally also written *slanted* in UML. Abstract classes are an abstract representation of a certain *expected functionality* and serve as so-called *interface base classes*, through which the functionality of derived classes can be accessed.

---

[9]In C++ such operations are referred to as *pure virtual member functions.*

```
                                                                    ┌ ─ ─ ─ ─ ─ ─ ┐
                                                                    ¦ T_Variable  ¦
┌───────────────────────────────────────────────────────────────┐ └ ─ ─ ─ ─ ─ ─ ┘
│                           TurbModel                             │
├───────────────────────────────────────────────────────────────┤
│ +updateYourself(:MeanFlowType,:TurbulenceType,:TurbBCsType)     │
│ +computeTurb(:MeanFlowType,:TurbulenceType)                     │
│ +giveKappa()                                                    │
└───────────────────────────────────────────────────────────────┘
```
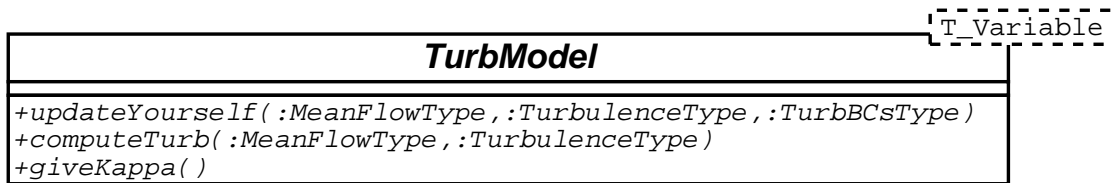
Figure 6.6:   Abstract interface base class `TurbModel`, providing flexible access to the functionality of the complete turbulence model.

The interesting question is now, what is the abstract functionality of a turbulence model? Here, it is assumed that the essence of any ensemble-averaged turbulence model is its ability to compute turbulent quantities from a given mean flow and its history, provided a turbulent length-scale and a turbulent time-scale are known (see, e.g., the discussion in the context of equation (18) of SPEZIALE [237]). In the class *TurbModel*, this functionality is abstractly expressed by the two operations *computeTurb()* and *updateYourself()*, shown in Fig. 6.6. The former operation takes an object of the type `MeanFlowType` as its argument to compute an object of the type `TurbulenceType`. The operation *updateYourself()* was provided as a means of updating internal variables of the turbulence model, expressing the turbulent length-scale and the turbulent time-scale[10].

Essentially, the complete functionality of any ensemble averaged turbulence model is contained in theses two functions[11]. It turned out that very few other, less obvious, operations have to be supplied for convenience. An example is *giveKappa()*, which returns the von Kármán constant, κ, a property of the turbulence model that is also needed to compute the boundary conditions for the velocity field in the logarithmic boundary layer (see Appendix A.1). *Note, that the turbulence model will be accessed only through the interface provided by these few functions.* How the turbulent quantities are actually computed is an *implementation secret* of the model.

The class *CanutoASM*, derived from the interface base class *TurbModel*, is an example of a class that is abstract (i.e. no objects can be created from it), but that provides already a certain functionality expressed by its operations. Its operation *updateYourself(...)*, overriding the operation with the same signature in its base class *TurbModel*, had to be declared "abstract", since *CanutoASM* does not have any attributes to be updated. For

---

[10]The term "internal variable" was chosen to emphasize, that such quantities are intrinsic properties of the turbulence model, that need not to be known by the RANS (in contrast to the correlation $\langle u'w' \rangle$, for example).

[11]The operation *updateYourself()* could also have been absorbed in *computeTurb()*. However, for reasons that cannot be explained here, it is desirable to distinguish between operations that change the state of their objects (like *updateYourself()*) and operations that do not (like *computeTurb()*).

the same reason the operation *computeTurb(:MeanFlowType ...)* had to be declared "abstract" as well. Thus, implementations for both operations have to be provided by one of the classes derived from *CanutoASM* (see below).
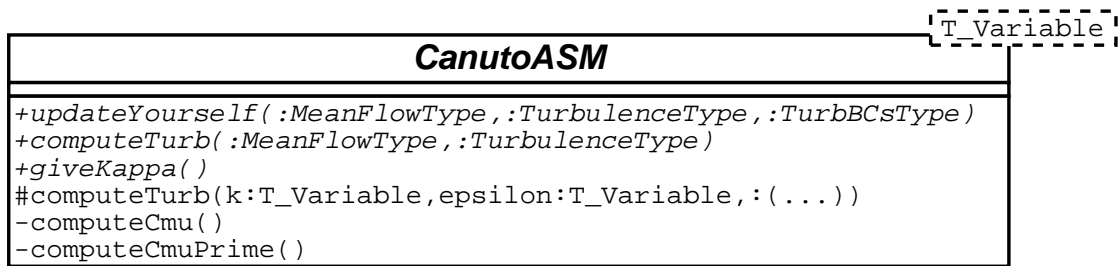

Figure 6.7: Abstract class *CanutoASM*, implementing the functionality of the ASM of Canuto et al. [38]

The essential functionality of the ASM of Canuto et al. [38] (and of many others) is its ability to compute turbulent correlations, provided the mean flow parameters, a turbulent length-scale, and a turbulent time-scale are given, irrespective of how they have been derived. Here, the variables k and ϵ have been chosen to express the latter two quantities, since ϵ has to be computed in most models anyway for insertion in the budget of k. The functionality just described is implemented in form of the operation `computeTurb(k:T_Variable, epsilon:T_Variable, ...)`[12]. This operation was declared "protected" and can thus be called from any derived class as soon as updated values of k and ϵ (here: the objects `k` and `epsilon`) are available. For the computation of the turbulent fields, this operation can use the services of other operations like `computeCmu()` or `computeCmuPrime()`, computing the stability functions.

The second important base class in Fig. 6.5 is `KeModel`, an abstraction of the well-known k-ϵ two-equation model. There are other classes to replace `KeModel`, like `KwModel` (the k-ω model) or `M_Y_Model` (the Mellor-Yamada model) not shown here[13]. It could be objected, that each of these classes should itself also be derived from a more general class (called, e.g., `TwoEquationModel`), which implements the general functionality of a two-equation model. In fact, this would have been a very consistent and code-reducing method, and there is only one reason why this idea was not pursued any further: It is planned in the near future to replace each of the two-equation models with one single *generic* two-equation model, in which the second equation describes the evolution of a general variable

---

[12]Note, that `computeTurb(k:T_Variable, ...)` has the same name as *computeTurb(:MeanFlowType, ...)* (declared in the class *TurbModel*), but different arguments. It will thus *not* override this function.

[13]Not only two-equation models can replace the class `KeModel`. In fact, any other class, capable of computing a turbulent length-scale and a turbulent time-scale (i.e. k and ϵ here), would be appropriate.

$k^m \epsilon^n$, where m and n are rational numbers (see BURCHARD [26]). All two-equation models used in this study can be recovered by setting m and n to the appropriate values. Even though abstraction in object-oriented languages is a powerful tool, being a physicist I felt that it is much more satisfying to have a higher abstraction level in the physical model.
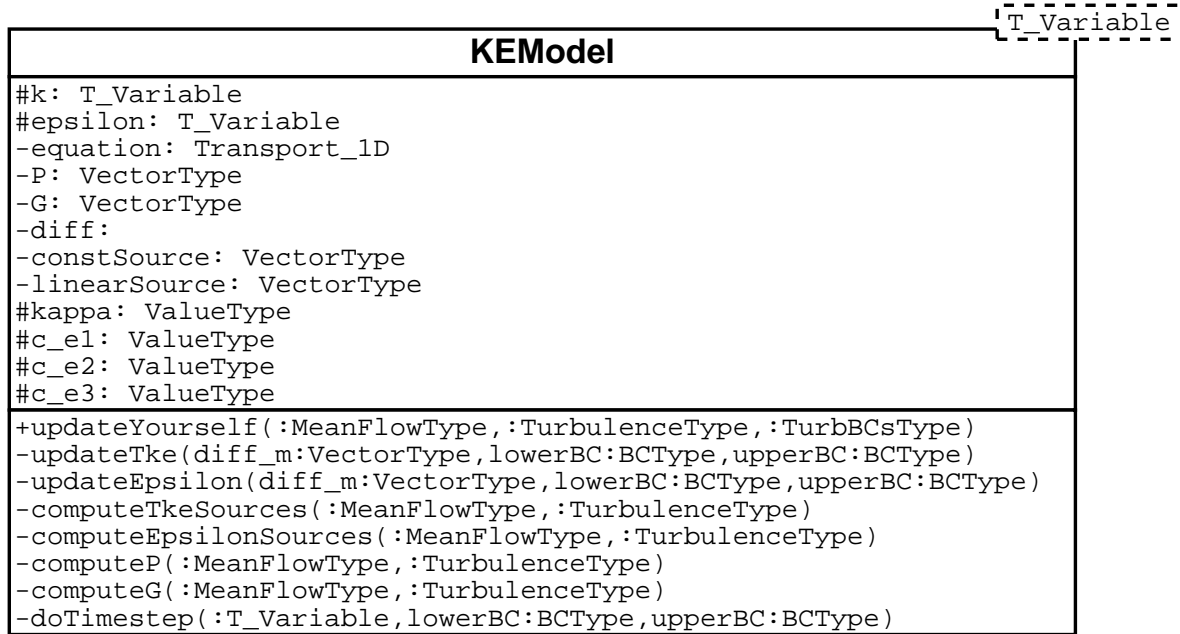
```
                                                              ┌ ─ ─ ─ ─ ─ ─ ┐
                                                               T_Variable
┌──────────────────────────────────────────────────────────┐ └ ─ ─ ─ ─ ─ ─ ┘
│                          KEModel                           │
├──────────────────────────────────────────────────────────┤
│#k: T_Variable                                              │
│#epsilon: T_Variable                                        │
│-equation: Transport_1D                                     │
│-P: VectorType                                              │
│-G: VectorType                                              │
│-diff:                                                      │
│-constSource: VectorType                                    │
│-linearSource: VectorType                                   │
│#kappa: ValueType                                           │
│#c_e1: ValueType                                            │
│#c_e2: ValueType                                            │
│#c_e3: ValueType                                            │
├──────────────────────────────────────────────────────────┤
│+updateYourself(:MeanFlowType,:TurbulenceType,:TurbBCsType) │
│-updateTke(diff_m:VectorType,lowerBC:BCType,upperBC:BCType) │
│-updateEpsilon(diff_m:VectorType,lowerBC:BCType,upperBC:BCType)│
│-computeTkeSources(:MeanFlowType,:TurbulenceType)           │
│-computeEpsilonSources(:MeanFlowType,:TurbulenceType)       │
│-computeP(:MeanFlowType,:TurbulenceType)                    │
│-computeG(:MeanFlowType,:TurbulenceType)                    │
│-doTimestep(:T_Variable,lowerBC:BCType,upperBC:BCType)      │
└──────────────────────────────────────────────────────────┘
```

Figure 6.8:   The class `KeModel` used to update the values of the variables k and ϵ.

The responsibility of the class `KeModel` (or any other class that replaces it) is easy to define: For given objects of the types `MeanFlow`, `Turbulence`, and `TurbBCs` (the boundary conditions) it should provide updated values of k and ϵ at each time-step, as required by the ASM. As illustrated in Fig. 6.8, `k` and `epsilon` are among the first attributes of `KeModel`. They are of the type `T_Variable`, supplied in form of a template parameter from outside (see above). These two objects are marked "protected" (with an #) and are thus visible and accessible only from derived classes. The discretization and updating of `k` and `epsilon` is performed by `equation`, an object of the class `Transport_1D`, encountered already several times above. As with the class `RANS`, attributes are defined to hold the constant and linear source terms and the turbulent diffusivities. In addition, the objects `P` and `G`, representing shear and buoyancy production of turbulence at all grid points, have been declared. From (3.13) it is clear, that these quantities are needed in updating both, `k` and `epsilon`. The extra memory required for storing them is traded against the saved computational cost for re-computing them a second time at each time-step.

Found among the attributes of the `KeModel` are also its model constants, some of which

are listed in Fig. 6.8. Upon creation of an object of this class, these constants are assigned the standard values of the k-ϵ model. However, model constants are declared "protected" and can be changed by a derived class. This mechanism was necessary, since some model constants (e.g. κ, $c_{\epsilon 3}$, c_{μ}^0) might have to be changed after their initial assignment in order to comply with the ASM (see Chapter 3).

As remarked above, the only responsibility of the class `KeModel` is updating its internal state (i.e. the variables `k` and `epsilon`), and hence only one public (generally accessible) operation was declared. This operation, `updateYourself(...)`, updates the values of `k` and `epsilon` for given mean flow and turbulent parameters and boundary conditions at each time-step. `updateYourself()` will use the services of the private operations `updateTke()` and `updateEpsilon()`. These operations compute the respective constant and linear source terms (which in turn require the computation of the attributes `P` and `G`). Finally the operation `doTimestep(...)` forwards all information to the object `equation`, which knows how perform the actual time-step (see above). All other operations listed in `KeModel` are helper functions with a functionality implied by their respective names.

6.7 Interaction of the Framework Components

The complete functionality of the model is available at this point. Only one link is missing: A component that makes correct use of the available facilities. As seen from Fig. 6.5, this task has been assigned to the class `KeCanutoASM`, derived from both, *CanutoASM* and `KeModel`. Its responsibilities are the proper creation and initialization of all base classes, the data exchange between objects, and the global management of the time-step.

As shown in Fig. 6.9, the class `KeCanutoASM` implements all the abstract operations declared in its base classes. This is required, since this class represents the top of the class hierarchy introduced above. Since `KeCanutoASM` has no attributes to be updated, its first operation, `updateYourself(...)`, simply forwards its arguments to an operation of the same name, declared in its base class `KeModel` (see lowest panel of this figure).

The second operation, `computeTurb(:MeanFlowType ...)`, has, on the one hand, access to the updated objects `k` and `epsilon` via its base class `KeModel` and, on the other hand, to an operation of the same name declared in its base class `CanutoASM`. As demonstrated above, the latter operation has the facilities to compute the `turbulence` object, provided `k` and `epsilon` are given. As illustrated in the middle panel of Fig. 6.9, all the operation `computeTurb(:MeanFlowType ...)` has to do, is calling `computeTurb(k:T_Variable,`

```
                                                          ┌ ─ ─ ─ ─ ─ ─ ┐
                                                            T_Variable
┌──────────────────────────────────────────────────┐ └ ─ ─ ─ ─ ─ ─ ┘
│                   KeCanutoASM                       │
├──────────────────────────────────────────────────┤
│ +updateYourself(:meanFlowType,:TurbulenceType,:TurbBCsType)
│ +computeTurb(:MeanFlowType,:TurbulenceType)
│ +giveKappa()
└──────────────────────────────────────────────────┘

        ┌──────────────────────────────────────────┐
        │ {                                          │
        │  CanutoASM<T_Variable>::                   │
        │  computeTurb(k,epsilon,meanFlow,turbulence, ...) │
        │ }                                          │
        └──────────────────────────────────────────┘

            ┌──────────────────────────────────────┐
            │ {                                      │
            │  KeModel<T_Variable>::updateYourself(); │
            │ }                                      │
            └──────────────────────────────────────┘
```
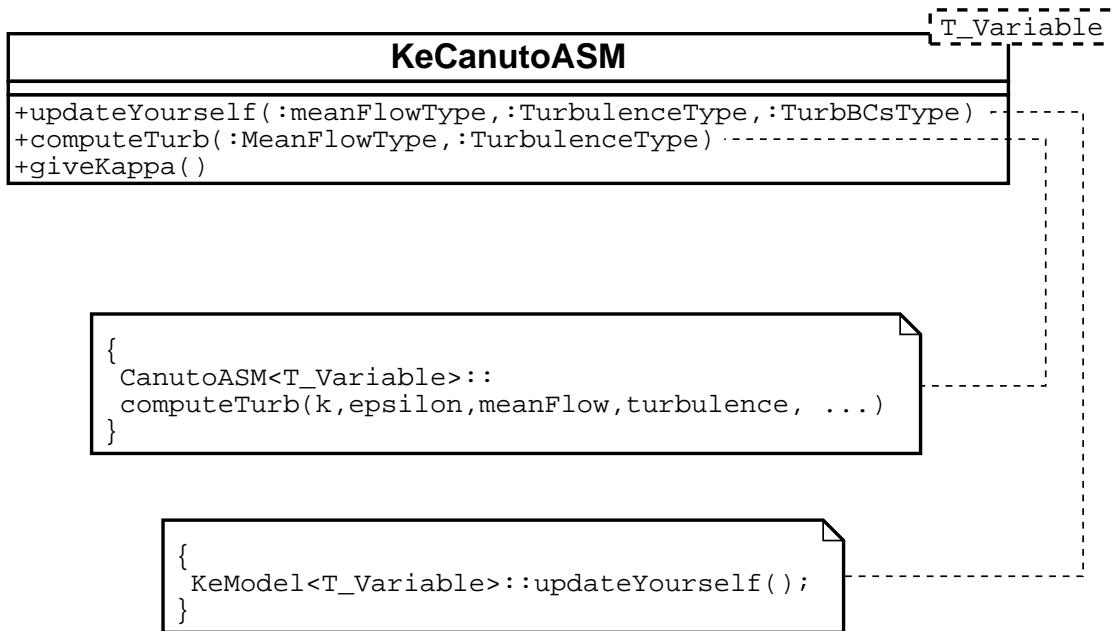
Figure 6.9: Class `KeCanutoASM`, responsible for data exchange and time-step management. The implementations of its operations (in C++) are given in the lower panels of this figure.

`...)` in *CanutoASM* with the updated arguments.

6.8 Dynamical Aspects of the Class System

In the previous sections, only the static aspects of the class system have been addressed. It is instructive to look also at the system "in action", when the interplay between different objects and operations becomes evident. UML provides several extra types of diagrams to model the dynamical aspects of a class system, however, for the brief discussion given here, it is more appropriate to simply use a literal description of what is happening.

It was remarked in the context of Fig. 6.6 that any part of the program can access the turbulence model only through a few interface operations declared in the class *TurbModel*. The cascade of actions triggered by a call to the services of each of these operation is illustrated below, starting with the very simple operation `getKappa()`, which returns the value of the von Kármán constant, κ (see Fig. 6.6).

Since *getKappa()* was declared "abstract" in `TurbModel` (i.e. it does not have any implementation), it will be searched for an implementation in one of the derived classes.

The class *CanutoASM*, derived from *TurbModel*, is the next candidate. However, this class cannot return an appropriate value of κ either, since κ is computed from one of the consistency equations (3.15)–(3.17) and the ASM has no knowledge about which two-equation model is used (or if one is used at all). Hence, *getKappa()* must be declared "abstract" also in this class. The next candidate is KeCanutoASM, derived from *CanutoASM*. Even though this class does not have any attribute called kappa, it has access to the protected attribute kappa of its second base class KeModel. Thus, the operation getKappa() from KeCanutoASM will return this attribute and the operation call is completed.

The next example is the operation *updateYourself(...)*, also declared in *TurbModel*. Recall from Fig. 6.6 that this operation takes several objects describing the mean and turbulent fields and the boundary conditions as its arguments. However, there is nothing to be updated in *TurbModel*, since this class has no attributes and hence *updateYourself(...)* was declared "abstract". The same applies to the derived class *CanutoASM*. The next derived class, KeCanutoASM, does not have any attributes either, but its base class KeModel has, and thus updating is delegated to this class as described in the context of Fig. 6.9 above.

The last example is the operation *computeTurb(:MeanFlowType ...)*, also declared "abstract" in the interface class *TurbModel*. Even though the derived class *CanutoASM* has the facilities to compute the turbulent fields (see above), this operation cannot be executed directly, since the two required fields, k and ϵ, are still missing. Since it is not the responsibility of *CanutoASM* to provide these fields, *computeTurb(...)* was declared "abstract" and it is relied on a derived class to provide the necessary information. The derived class KeCanutoASM does not know itself how to provide updated values of k and ϵ, but it has the base class KeModel with up-to-date values of k and epsilon, exactly the information needed. Thus, all the operation computeTurb(:MeanFlowType ...) of KeCanutoASM needs to do is forwarding these objects to the operation computeTurb(k:VariableType, ...) declared in its base class *CanutoASM*. As illustrated above, this operation has a complete implementation at its disposal to compute the turbulent fields.

To clarify the full power of the framework introduced in this section, some concluding remarks are necessary. The most important point to notice is the *generic* character of the framework: Models can be composed immediately from the following "orthogonal base components": 1.) The Algebraic Stress Model (ASM) component 2.) The k-ϵ component[14] 3.) The spatial discretization component 4.) The time-stepping component.

---

[14]This term refers to the model component that computes the turbulent length-scale and the turbulent time-scale (here the parameters k and ϵ) needed by the ASM. This may be, e.g., an arbitrary one- or

Alone from the components available at the moment, dozens of different models can be combined. Extensions (new numerical schemes, new turbulence models, ...) are easily imagined.

Moreover, since the turbulence model and the RANS will be represented by objects, encapsulating all their data and allowing for their access only through precisely defined interfaces, several models can easily co-exist at the same time in a single program. It is, in principle, conceivable to have one model computing the hydrodynamics of a lake (e.g., a k-ϵ model with the ASM of CANUTO ET AL. [38], discretized with the Finite-Volume method), coexisting with another model computing the wind field and other atmospheric quantities over the lake (e.g., a k-ω model with the ASM of GALPERIN ET AL. [81], discretized with a Finite-Element method). Coupling of these two models would be particularly easy, because only a few objects, encapsulating the boundary conditions, had to be considered. A third model could be added, especially appropriate for a refined computation of an incoming river mouth, and so on.

Even though there is a long way to go, before this vision will become reality, the first step has been taken by successfully applying the object-oriented design concepts, introduced here, to state-of-the-art one-dimensional turbulence models.

---

two-equation model.

Chapter 7

Conclusions

Many different topics have been discussed in this study, including recent ideas in turbulence modelling, oceanography and physical limnology, physical-biological interactions, numerical methods, and innovative programming approaches to turbulence modelling. In this chapter, the results are summarized, some conclusions are drawn, and the fields of future research are envisaged.

It was remarked in the introduction that a correct representation of the turbulent quantities forms one of the cornerstones of a reliable hydrodynamical model for natural waters and hence also for a biological sub-model. Numerous approved turbulence models are known in the literature, however, their respective authors tend to use different notations, making it uncomfortably difficult to compare these models. To achieve a better comparability, several well-known turbulence models, introduced in Chapter 2, were mapped into a unified notation, from which individual models can be easily recovered by setting the model constants to the values given in Tab. 2.1 and Tab. 2.2. The somewhat elaborate conversions between the original and the unified notation, respectively, are given in appendices.

Starting from this unified turbulence model, it was straightforward to invoke the two major simplifications: The algebraization of the system of differential equations describing the evolution of the turbulent quantities, and the application of the so-called boundary layer approximation. With these simplifications, a coupled linear system of 10 algebraic equations for the turbulent correlations was obtained and solved explicitly with the help of a symbolic algebra tool. It turned out, that the vertical turbulent fluxes of momentum and heat can be expressed in terms of so called stability functions that formed the basis

for many conclusions drawn in the following chapters[1]. Of course, a comparable procedure had been executed by other authors for their individual models. With this study, however, a general model in a unified notation is available[2], from which the most well-known turbulence models, applied in oceanography, can be recovered.

After a short discussion of the relative merits of integrated and differential turbulence models in geophysical applications, Chapter 3 continued with the introduction of three two-equation models, compared in great detail in the following sections: The k-ϵ model, the model of MELLOR AND YAMADA [169] and two versions of the k-ω model of WILCOX [293, 294]. Even though a few comparisons of the former two models are known in the oceanographical literature, apparently no investigations of the k-ω model in a geophysical context had been reported by the time this project started. This fact should not come as a surprise, since the k-ω model, in its original form, was not suited to deal with buoyancy affected flows, omnipresent in geophysical situations. Nevertheless, since the k-ω model was reported to be superior to the k-ϵ model in many unstratified industrial flows, interest was felt in an investigation of the qualities of this model in stratified flows, and particularly in oceanographical and limnological situations. To this end, in Chapter 3 a generalization of the k-ω model to stratified flows was introduced (also see UMLAUF AND HUTTER [280]). As summarized below, a number of interesting and unexpected results were obtained.

Before the structural differences between the three models were emphasized, an important flow type was explored, in which all models are isomorphic: The so-called structural equilibrium, mathematically established by the requirement that the time rate of the turbulent time-scale $\tau = k/\epsilon$ is zero. Turbulence in structural equilibrium is of particular interest, since a wealth of data from laboratory experiments and DNS exist, usable to verify turbulence models. Turbulent parameters obtained from stratified flow experiments of this type are most often expressed in terms of the gradient Richardson number, and it is only natural to look for analytical solutions of the turbulence models exhibiting also a functional dependence on this quantity. Many different sets of stability functions[3], expressible solely in terms of the gradient Richardson number have been suggested in the literature, but most of them were derived assuming the full equilibrium $P+G = \epsilon$. Clearly, this assumption does not hold in structural equilibrium, and no definite conclusions can

---

[1]As discussed in Chapter 2, rotational terms were not considered in the stability functions.

[2]In this context, "available" means that the model does not only exist "on paper", but also in form of a "symbolic notebook" of the symbolic algebra package "MATHEMATICA", from which new models can be easily derived and tested.

[3]Recall, that stability functions are the "essence" of any ASM, if the boundary layer approximation is invoked.

be drawn by comparing these stability functions (and quantities derived from them) with the experiments mentioned above. Besides this, apparently no successful attempts were reported to express the few existing non-equilibrium stability functions in terms of the Richardson number in structural equilibrium. Here, such stability functions, also valid in structural equilibrium, could be derived with the help of symbolic algebra. From these followed Richardson number depending expressions for the turbulent Prandtl number and for some important turbulent length scales, all quantities that could directly be compared to laboratory measurements and DNS in Chapter 3. The encouraging result was, that two-equation models predict the fundamental properties of the structural equilibrium fairly well, provided the Richardson number is not too large. However, some of the results were very sensitive with respect to small differences in model parameters, and even though all models are isomorphic in structural equilibrium, the best results were obtained with the parameters of the k-ω model.

A situation, in which structural differences between two-equation models are most essentially manifested, is the balance between turbulent diffusion and dissipation of turbulent kinetic energy. This case is also of some interest in oceanography and physical limnology because of the current belief, that below breaking waves there is a small fluid layer with approximately such a balance. So far, only inappropriate (though popular) analytical results have been reported in the oceanographical literature, all together assuming that the turbulent length scale in the diffusion-dissipation balance behaves exactly as in the logarithmic region of the law-of-the-wall. This is, of course, not true because the von Kármán constant, an important parameter in wall-bounded shear-flows, is completely irrelevant in shear-free situations like that described above. In Chapter 3, a new set of power law solutions was suggested for the non-linear coupled differential equations describing the diffusion-dissipation balance in two-equation models. A close investigation of the results revealed the surprising fact that the popular k-ϵ model exhibits a singularity for completely reasonable parameter combinations. The Mellor-Yamada model only computes results in accordance with measurements, if its wall function is neglected, and only the k-ω model performs satisfactorily in all situations. Currently, these results are extended and applied to the oceanic wave-mixed layer and an according publication is on its way (UMLAUF AND BURCHARD [279]).

Some applications of two-equation models in oceanography and limnology were described in Chapter 4. It was shown in the first parts of this chapter that in some unstratified standard situations (turbulent plane Couette flow, turbulent barotropic open channel flow) the k-ϵ model and the k-ω model perform very similarly. As demonstrated by other authors, also in stratified shear-driven flows, two-equation models tend to perform quite

similarly. It was also shown in this context, that in shear-driven mixed-layer entrainment experiments ("wind mixing"), the entrainment depth predicted by the k-ϵ model and the Mellor-Yamada model is controlled almost exclusively by the value of the steady-state Richardson number, Ri_{st}, at the bottom of the mixing layer. This result could be demonstrated to hold also for the new, buoyancy extended k-ω model. For this type of experiments, also a new theoretical result was obtained: The question of KUNDU [143], what would physically be the most relevant condition for the self-similarity of the problem, could be resolved: It was demonstrated that the conditions for the bulk Richardson number, $Ri_v = $ const., for the flux Richardson number , $Ri_f = $ const., and for the gradient Richardson number, $Ri = $ const. are completely equivalent, because turbulence at the bottom of the mixing layer is in a state of full equilibrium.

Besides these idealized test cases, also some direct applications to limnological problems were considered. The first of these was a simulation of the seiche induced, oscillating bottom boundary layer in Lake Alpnach, a small Swiss lake. Because of the excellent cooperation with the EAWAG (Switzerland), a unique set of continuously measured dissipation rate records in the turbulent bottom layer of this lake was available and directly comparable to the results computed by different two-equation models. The observed phase-lag between the dissipation rate and the current shear turned out to be under-predicted by both, the k-ω model and, though to a lesser extent, also by the k-ϵ model. The magnitude of the computed dissipation rate, however, was demonstrated to be in good agreement with the measured values. Previous techniques estimated the dissipation rate based on logarithmic fits to measured velocity profiles. It could be demonstrated that with this popular method the dissipation rate is overestimated by about an order of magnitude in dynamical boundary layers. In weakly stratified oscillating boundary layers, the predicted height of the (almost) homogenized bottom layer was also in good agreement with the measurements (also see UMLAUF AND LORKE [282]). Since the flux of momentum from the seiche motion to the boundaries, the exchange of properties between sediment and water, and also the redistribution of matter inside the water body, all fundamentally depend on the turbulence in the bottom layer, this encouraging result was an important step towards the development of a robust three-dimensional water quality model for lakes.

The second limnological application consisted of a coupled biological-physical model of the oxygen budget in Lake Ammer, a medium-sized Alpine lake. It was one of the few attempts of coupling a two-equation turbulence model to a biological sub-model, reported in the limnological literature. In contrast to most other approaches, here the biological sub-model did not include evolution equations for different aquatic species and nutrients.

It rather related all biological parameters to measured profiles of chlorophyll-a, interpreted as a measure of biomass. With this method, many of the uncertainties of a full biological parameterization are avoided, since effects like nutrient limitation, grazing pressure, etc. were already implicitly accounted for in the measured chlorophyll-a values. Computed results and measured data for both, temperature and oxygen, were demonstrated to be in good agreement. (also see JOEHNK AND UMLAUF [129]).

The numerical procedure was introduced in Chapter 5. It consists of an application of the popular Finite-Volume method, and thus this chapter was mainly conceived as part of a documentation of the numerical code. Nevertheless, a small novelty could be presented: The staggered grid used here employed a different kind of boundary volumes than that adopted by most other authors. It could be shown that the recommendation of BURCHARD AND PETERSEN [30], to generally only use flux boundary conditions for the turbulent quantities, is restricted to a special (though popular) type of boundary volumes. Accurate results can also be obtained with the classical Dirichlet-type boundary conditions, if the numerical grid suggested here is used.

Even though remarks on numerical methods can be found in many publications on turbulence modelling, most often only subtle hints are given of how the numerical procedure was actually translated to the programming language. Since much of the manpower in numerical turbulence research is devoted to coding issues, this under-representation is hard to justify. Chapter 6 extensively addresses coding issues and a new object-oriented approach to turbulence modelling, equally applicable to industrial and geophysical flows. Different classes of objects were assigned different responsibilities during the computation of mean flow and turbulent parameters. The resulting code is structured in different levels of abstraction, reaching from very abstract classes like **TurbModel** (representing a complete turbulence model) down to fast FORTRAN subroutines performing the actual "number crunching" by solving large linear systems. Due to the generic character of the class framework, base components can be almost arbitrarily combined to yield new models, and a program evolved that can be easily understood, extended and maintained.

Appendix A

Turbulence

A.1   Solution Close to a Rigid Wall

Close to a smooth rigid wall two independent length-scales can be formulated from the indicated dimensional parameters, namely, a viscous length-scale $\delta_v = \nu/u_*$ and an external length-scale δ. Here, $u_* = \tau_w/\rho$ is the friction velocity determined by the density and the shear stress at the wall, τ_w.[1] Dimensional analysis leads to the general functional form of the velocity profile

$$u = u_* \Phi\left(z^+, \zeta\right) \quad \text{and} \quad \frac{\partial u}{\partial z} = \frac{u_*}{z} \phi\left(z^+, \zeta\right) , \qquad (A.1)$$

where

$$z^+ = \frac{z}{\delta_v} \quad \text{and} \quad \zeta = \frac{z}{\delta} \quad . \qquad (A.2)$$

Usually, two limiting versions of the general statement (A.1) are considered: At $z \ll \delta$ the influence of the external scale δ is assumed to be negligible and the dependence on ζ drops out. At $z \gg \delta_v$ the influence of the viscosity on the relative motion of the fluid vanishes and (A.1) does not depend any longer on z^+. The existence of the first of these limits implies *Prandtl's universal law-of-the-wall*, while the existence of the second implies *Kármán's velocity defect law*.

It is well-known that there exists an overlap region with a logarithmic velocity profile in which both laws are assumed to be valid (YAGLOM [300], SPURK [241]). This region is

---

[1]For completely rough walls the viscous scale δ_v is replaced by the roughness length z_0. An additional length-scale $\delta_p = u_*^2/\alpha_p$ is introduced in the presence of a pressure-gradient $\alpha_p = \rho^{-1} dP/dx$. This case is not considered here.

referred to as the *logarithmic region* of the law-of- the-wall. The solutions computed by two-equation models in this region will be investigated in the following section.

A.1.1   The Logarithmic Region of the Law of the Wall

From the equations of motion and dimensional arguments it follows that in the logarithmic region the relations

$$-\langle u'w' \rangle = \frac{\tau_w}{\rho} = u_*^2 \quad \text{and} \quad \frac{\partial u}{\partial z} = \frac{u_*}{\kappa(z + z_0)} \tag{A.3}$$

hold, if the pressure is constant and the viscosity exerts no direct influence on the flow. Here, κ is the so-called *von Kármán constant* and z_0 is the *roughness length*.

In this flow region, the turbulent kinetic energy, k, is constant and only related to the friction velocity, u_*, via

$$k = \frac{u_*^2}{c_B} , \tag{A.4}$$

where the dimensionless constant $c_B \approx 0.3$ is sometimes referred to as the Bradshaw constant.

If a simple mixing length model of the form

$$u_*^2 = \nu_t \frac{\partial u}{\partial z} \tag{A.5}$$

is applied and (A.3) and (A.4) are used, some standard turbulent quantities can be computed as

$$P = \epsilon = \frac{u_*^3}{\kappa(z + z_0)} , \quad \omega = \frac{c_B}{(c_\mu^0)^4} \frac{u_*^2}{\kappa(z + z_0)} , \quad l = \kappa(z + z_0) , \quad \nu_t = \kappa u_*(z + z_0) \quad . \tag{A.6}$$

Following most authors, the origin $z = 0$ has been shifted by the roughness length z_0.

All turbulence models considered in the main part compute the friction velocity, u_*, according to

$$u_*^2 = \frac{\tau}{\rho} = \nu_t \frac{\partial u}{\partial z} = c_\mu^\epsilon \frac{k^2}{\epsilon} \frac{\partial u}{\partial z} , \tag{A.7}$$

which, making use of (A.3), (A.4), and (A.6) can be transformed to the simple statement

$$c_B = \sqrt{c_\mu^\epsilon} \quad , \text{with} \quad c_\mu^\epsilon = \tilde{c}_\mu^\epsilon(\alpha_M) \quad (\text{see (2.53)}) \quad . \tag{A.8}$$

Hence, all models predict a constant friction velocity u_* only if the function $\tilde{c}_\mu^\epsilon$ is constant and equal to the square of Bradshaw's constant, c_B^2.

For the quasi-equilibrium stability functions introduced in Section 2.3.2 this is obviously the case: In the unstratified logarithmic boundary layer the buoyancy parameter is $\alpha_N = 0$ and $\tilde{c}_\mu^\epsilon$ becomes a constant. For the non-equilibrium stability functions (as those of (2.60) and (2.61)) a dependence on α_M remains, and it has to be shown that α_M becomes a constant in the logarithmic boundary layer. Indeed, using (A.3), (A.6), and (A.8) the following relations emerge

$$\alpha_M := \frac{k^2}{\epsilon^2}\left(\frac{\partial u}{\partial z}\right)^2 = \frac{1}{c_\mu^\epsilon} \quad \Rightarrow \quad c_\mu^\epsilon = \tilde{c}_\mu^\epsilon(\alpha_M) = \tilde{c}_\mu^\epsilon\left(\frac{1}{c_\mu^\epsilon}\right) \quad . \tag{A.9}$$

The last relation is a non-linear equation for the value of c_μ^ϵ in the logarithmic boundary layer. For the non-equilibrium stability functions (2.60) a value of $c_\mu^\epsilon = 0.077$ can be computed, considerably lower than the standard value $c_\mu^\epsilon = 0.09$. Since $P = \epsilon$ holds in the logarithmic boundary layer, this value coincides with the value computed by the quasi-equilibrium version of the non-equilibrium stability functions in the unstratified case $Ri = \alpha_N = 0$ (see Fig. 3.13). This is not surprising, since the equilibrium $P + G = \epsilon$ has been assumed in their derivation.

Finally, integration of the second of (A.3) yields the well-known logarithmic law-of-the-wall

$$\frac{u}{u_*} = \frac{1}{\kappa}\ln\left(\frac{z + z_0}{z_0}\right) , \tag{A.10}$$

where the coordinate z has been shifted by the roughness length z_0.

A.1.2 The Roughness Length

The standard form of the logarithmic velocity profile for hydraulically smooth walls can be recovered from (A.10) by setting

$$z_0 = a_s \frac{\nu}{u_*} , \tag{A.11}$$

with the dimensionless constant a_s. If (A.11) is inserted in (A.10) and the dimensionless quantities

$$u^+ = \frac{u}{u_*} \quad \text{and} \quad z^+ = \frac{zu_*}{\nu} \tag{A.12}$$

are introduced, (A.10) can be re-written as

$$u^+ = \frac{1}{\kappa}\ln\left(z^+ + a_s\right) + \underbrace{\frac{1}{\kappa}\ln\frac{1}{a_s}}_{B} \quad . \tag{A.13}$$

The appearance of the constant a_s in the argument of the logarithm stems from the fact that the origin has been shifted by the roughness length z_0. However, adopting the standard values $\kappa = 0.4$ and $B = 5.0$, $a_s = 0.135$ can be computed. This is a value very small compared to $z^+ \approx 5$, below which the logarithmic law is known to loose its validity anyway. Thus, the solution (A.13), computed by the two-equation models, is almost identical to the more familiar form

$$u^+ = \frac{1}{\kappa} \ln z^+ + B \quad . \tag{A.14}$$

The solution for a completely rough wall is obtained from (A.10), if

$$z_0 = k_s e^{-C\kappa} \, , \tag{A.15}$$

which linearly relates the *sand roughness* k_s to the roughness length z_0. The resulting velocity profile reads

$$\frac{u}{u_*} = \frac{1}{\kappa} \ln \left(\frac{z + z_0}{k_s} \right) + C \quad . \tag{A.16}$$

It differs from the standard form only by its shift z_0 from the origin. Often cited values for a completely rough plate are $\kappa = 0.4$ and $C = 8.0$, from which a sand roughness $k_s = 24.53 \, z_0$ can be computed.

Between the limits of hydraulically smooth and completely rough surfaces numerous interpolating formulae have been suggested (cf. SCHLICHTING AND GERSTEN [217], pp. 517). Since usually only little is known about the precise properties of the sediment structure in lakes and the ocean, it is appropriate here to simply add both contributions and obtain

$$z_0 = a_s \frac{\nu}{u_*} + k_s e^{-C\kappa} \quad . \tag{A.17}$$

This formula yields the correct limits for smooth and rough surfaces and interpolates by simple superposition in between.

A.2   Boundary Layer Approximation

It has been shown in Section 2.3 that the so-called boundary layer approximation greatly simplifies the equations of motion and the equations describing the transport of turbulent quantities. Recall, that in the boundary layer approximation, all horizontal gradients (i.e., gradients in the x- and y-direction) are negligible, except the horizontal pressure-gradient in the momentum balance.

In this section, the boundary layer approximation is accepted in order to simplify the tensor quantities appearing in the ASM (2.34)–(2.36). The form of a tensor quantity, simplified in this manner, will be referred to as its *boundary layer form* from now on. By inserting the boundary layer forms into the ASM (2.34)–(2.36), the boundary layer form of the ASM given in (2.39)–(2.48) can be obtained.

The starting point is the derivation of the boundary layer form of the symmetric and anti-symmetric parts of the velocity gradient as defined in (2.17). If only vertical gradients are considered, they reduce to

$$
S_{ij} = \begin{pmatrix} 0 & 0 & \frac{1}{2}\frac{\partial u}{\partial z} \\ 0 & 0 & \frac{1}{2}\frac{\partial v}{\partial z} \\ \frac{1}{2}\frac{\partial u}{\partial z} & \frac{1}{2}\frac{\partial v}{\partial z} & 0 \end{pmatrix} \quad \text{and} \quad W_{ij} = \begin{pmatrix} 0 & 0 & \frac{1}{2}\frac{\partial u}{\partial z} \\ 0 & 0 & \frac{1}{2}\frac{\partial v}{\partial z} \\ -\frac{1}{2}\frac{\partial u}{\partial z} & -\frac{1}{2}\frac{\partial v}{\partial z} & 0 \end{pmatrix} , \tag{A.18}
$$

respectively.

The production of Reynolds stresses by the mean shear is

$$
P_{ij} = -\langle u_i' u_l' \rangle \frac{\partial u_j}{\partial x_l} - \langle u_j' u_l' \rangle \frac{\partial u_i}{\partial x_l} ,
$$

as defined in (2.8). In its boundary layer form this tensor reduces to

$$
P_{ij} = \begin{pmatrix} -2\langle u'w' \rangle \frac{\partial u}{\partial z} & -\langle v'w' \rangle \frac{\partial u}{\partial z} -\langle u'w' \rangle \frac{\partial v}{\partial z} & -\langle w'^2 \rangle \frac{\partial u}{\partial z} \\ -\langle v'w' \rangle \frac{\partial u}{\partial z} -\langle u'w' \rangle \frac{\partial v}{\partial z} & -2\langle v'w' \rangle \frac{\partial v}{\partial z} & -\langle w'^2 \rangle \frac{\partial v}{\partial z} \\ -\langle w'^2 \rangle \frac{\partial u}{\partial z} & -\langle w'^2 \rangle \frac{\partial v}{\partial z} & 0 \end{pmatrix} . \tag{A.19}
$$

Similarly, the "anisotropic production" tensor

$$
D_{ij} = -\langle u_i' u_l' \rangle \frac{\partial u_l}{\partial x_j} - \langle u_j' u_l' \rangle \frac{\partial u_l}{\partial x_i} ,
$$

defined in $(2.15)_1$, reduces to the form

$$D_{ij} = \begin{pmatrix} 0 & 0 & -\langle u'^2 \rangle \dfrac{\partial u}{\partial z} \\ & & -\langle u'v' \rangle \dfrac{\partial v}{\partial z} \\[2ex] 0 & 0 & -\langle v'^2 \rangle \dfrac{\partial v}{\partial z} \\ & & -\langle u'v' \rangle \dfrac{\partial u}{\partial z} \\[2ex] -\langle u'^2 \rangle \dfrac{\partial u}{\partial z} & -\langle v'^2 \rangle \dfrac{\partial v}{\partial z} & -2\langle u'w' \rangle \dfrac{\partial u}{\partial z} \\ -\langle u'v' \rangle \dfrac{\partial v}{\partial z} & -\langle u'v' \rangle \dfrac{\partial u}{\partial z} & -2\langle v'w' \rangle \dfrac{\partial v}{\partial z} \end{pmatrix} . \qquad (A.20)$$

It is a bit more tedious to derive the boundary layer form of the "anisotropic production" tensor Σ_{ij} extensively used by CANUTO ET AL. [37, 38]. It is defined in $(2.15)_2$ and will be re-written here for convenience:

$$\Sigma_{ij} = S_{il}b_{lj} + S_{jl}b_{li} - \frac{2}{3}\delta_{ij}S_{lm}b_{lm} ,$$

where the symmetric part of the velocity gradient defined in $(2.17)_1$ and the anisotropic part of the Reynolds stress defined in (2.16) have been used.

The expression for Σ_{ij} can be easily re-written in the form

$$\Sigma_{ij} = S_{il}\langle u'_l u'_j \rangle + S_{jl}\langle u'_l u'_i \rangle - \frac{4}{3}K S_{ij} + \frac{2}{3}\delta_{ij}P \qquad (A.21)$$

or in terms of P_{ij} and D_{ij} as

$$\Sigma_{ij} = -\frac{1}{2}(P_{ij} + D_{ij}) - \frac{4}{3}k S_{ij} + \frac{2}{3}\delta_{ij}P \quad . \qquad (A.22)$$

Thus, using the already known boundary layer forms of P_{ij} and D_{ij}, (A.19) and (A.20), the boundary layer form of Σ_{ij} can be shown to take the form

$$\Sigma_{ij} = \frac{1}{2} \begin{pmatrix} \frac{2}{3}\langle u'w' \rangle \dfrac{\partial u}{\partial z} & \langle v'w' \rangle \dfrac{\partial u}{\partial z} & (\langle u'^2 \rangle + \langle w'^2 \rangle - \frac{4}{3}k)\dfrac{\partial u}{\partial z} \\ -\frac{4}{3}\langle v'w' \rangle \dfrac{\partial v}{\partial z} & +\langle u'w' \rangle \dfrac{\partial v}{\partial z} & +\langle u'v' \rangle \dfrac{\partial v}{\partial z} \\[3ex] \langle v'w' \rangle \dfrac{\partial u}{\partial z} & -\frac{4}{3}\langle u'w' \rangle \dfrac{\partial u}{\partial z} & (\langle v'^2 \rangle + \langle w'^2 \rangle - \frac{4}{3}k)\dfrac{\partial v}{\partial z} \\ +\langle u'w' \rangle \dfrac{\partial v}{\partial z} & +\frac{2}{3}\langle v'w' \rangle \dfrac{\partial v}{\partial z} & +\langle u'v' \rangle \dfrac{\partial u}{\partial z} \\[3ex] (\langle u'^2 \rangle + \langle w'^2 \rangle - \frac{4}{3}k)\dfrac{\partial u}{\partial z} & (\langle v'^2 \rangle + \langle w'^2 \rangle - \frac{4}{3}k)\dfrac{\partial v}{\partial z} & \frac{2}{3}\langle u'w' \rangle \dfrac{\partial u}{\partial z} \\ +\langle u'v' \rangle \dfrac{\partial v}{\partial z} & +\langle u'v' \rangle \dfrac{\partial u}{\partial z} & +\frac{2}{3}\langle v'w' \rangle \dfrac{\partial v}{\partial z} \end{pmatrix} .$$

$$(A.23)$$

Another "anisotropic production" tensor, Z_{ij}, was introduced in $(2.15)_3$ and is defined by

$$Z_{ij} = W_{il}^* \left(\langle u_l' u_j' \rangle - \frac{2}{3} \delta_{lj} k \right) + W_{jl}^* \left(\langle u_l' u_i' \rangle - \frac{2}{3} \delta_{li} k \right) ,$$

where the tensor W_{ij}^* has been defined in $(2.17)_3$. This equation can be simply re-written as

$$Z_{ij} = -\frac{1}{2} \left(P_{ij} - D_{ij} + F_{ij} \right) \quad . \tag{A.24}$$

Hence the boundary layer form of Z_{ij} can also be found by using the known tensors P_{ij}, D_{ij}, and F_{ij} defined in (A.19), (A.20), and (A.31), respectively, to yield

$$Z_{ij} = \frac{1}{2} \begin{pmatrix} 2\langle u'w'\rangle \dfrac{\partial u}{\partial z} & \begin{matrix}\langle v'w'\rangle\dfrac{\partial u}{\partial z}\\+\langle u'w'\rangle\dfrac{\partial v}{\partial z}\end{matrix} & \begin{matrix}(\langle w'^2\rangle - \langle u'^2\rangle)\dfrac{\partial u}{\partial z}\\-\langle u'v'\rangle\dfrac{\partial v}{\partial z}\end{matrix} \\[3em] \begin{matrix}\langle v'w'\rangle\dfrac{\partial u}{\partial z}\\+\langle u'w'\rangle\dfrac{\partial v}{\partial z}\end{matrix} & 2\langle v'w'\rangle\dfrac{\partial v}{\partial z} & \begin{matrix}(\langle w'^2\rangle - \langle v'^2\rangle)\dfrac{\partial v}{\partial z}\\-\langle u'v'\rangle\dfrac{\partial u}{\partial z}\end{matrix} \\[3em] \begin{matrix}(\langle w'^2\rangle - \langle u'^2\rangle)\dfrac{\partial u}{\partial z}\\-\langle u'v'\rangle\dfrac{\partial v}{\partial z}\end{matrix} & \begin{matrix}(\langle w'^2\rangle - \langle v'^2\rangle)\dfrac{\partial v}{\partial z}\\-\langle u'v'\rangle\dfrac{\partial u}{\partial z}\end{matrix} & \begin{matrix}-2\langle u'w'\rangle\dfrac{\partial u}{\partial z}\\-2\langle v'w'\rangle\dfrac{\partial v}{\partial z}\end{matrix} \end{pmatrix} - \frac{1}{2}F_{ij} \quad . \tag{A.25}$$

The production of Reynolds stresses by buoyancy,

$$G_{ij} = g\delta_{i3}\alpha\langle\theta' u_j'\rangle + g\delta_{j3}\alpha\langle\theta' u_i'\rangle ,$$

has been defined in (2.8). In its boundary layer form it can be re-written as

$$G_{ij} = \begin{pmatrix} 0 & 0 & g\alpha\langle\theta' u'\rangle \\ 0 & 0 & g\alpha\langle\theta' v'\rangle \\ g\alpha\langle\theta' u'\rangle & g\alpha\langle\theta' v'\rangle & 2g\alpha\langle\theta' w'\rangle \end{pmatrix} \quad . \tag{A.26}$$

The same is possible for the two temperature-flux-production terms,

$$P_{\theta u1} = -\langle u_i' u_l'\rangle \frac{\partial \theta}{\partial x_l} \qquad \text{and} \qquad P_{\theta u2} = -\langle \theta u_l'\rangle \frac{\partial u_i}{\partial x_l} ,$$

which have been defined in (2.9). They become

$$P_i^{\theta u1} = \begin{pmatrix} -\langle u'w'\rangle\dfrac{\partial\theta}{\partial z} \\ -\langle v'w'\rangle\dfrac{\partial\theta}{\partial z} \\ -\langle w'^2\rangle\dfrac{\partial\theta}{\partial z} \end{pmatrix} , \quad P_i^{\theta u2} = \begin{pmatrix} -\langle\theta'w'\rangle\dfrac{\partial u}{\partial z} \\ -\langle\theta'w'\rangle\dfrac{\partial v}{\partial z} \\ 0 \end{pmatrix} \quad . \tag{A.27}$$

(2.9) also defines a buoyancy production term according to

$$G_i^{\theta u} = g\delta_{i3}\alpha\langle\theta'^2\rangle \; ,$$

which retains only its third component in the boundary layer form as in

$$G_i^{\theta u} = \begin{pmatrix} 0 \\ 0 \\ g\alpha\langle\theta'^2\rangle \end{pmatrix} \qquad . \tag{A.28}$$

The equation describing the transport of turbulent kinetic energy, (2.11), and the equation for the transport of temperature variance, (2.10), introduce three scalar production terms. In the boundary layer approximation they can be written as

$$
\begin{aligned}
P &= D = -\langle u'w'\rangle\frac{\partial u}{\partial z} - \langle v'w'\rangle\frac{\partial v}{\partial z} \; , \\
G &= g\alpha\langle\theta'w'\rangle \; , \\
P^\theta &= -2\langle\theta'w'\rangle\frac{\partial\theta}{\partial z} \quad .
\end{aligned}
\tag{A.29}
$$

Even though it was decided in Section 2.3 not to include any explicit or implicit Coriolis terms before a clear indication for their importance is given, the boundary layer form of the explicit terms shall be prepared here for later reference. Starting from the definition of the explicit Coriolis terms in (2.8),

$$F_{ij} = -f_{il}\langle u'_j u'_l\rangle - f_{jl}\langle u'_i u'_l\rangle \; , \tag{A.30}$$

their boundary layer form can be shown to reduce to

$$F_{ij} = \begin{pmatrix}
\begin{matrix} 2f\langle u'v'\rangle \\ -2\tilde{f}\langle u'w'\rangle \end{matrix} & \begin{matrix} f\left(\langle v'^2\rangle - \langle u'^2\rangle\right) \\ -\tilde{f}\langle v'w'\rangle \end{matrix} & \begin{matrix} \tilde{f}\left(\langle u'^2\rangle - \langle w'^2\rangle\right) \\ +f\langle v'w'\rangle \end{matrix} \\[2em]
\begin{matrix} f\left(\langle v'^2\rangle - \langle u'^2\rangle\right) \\ -\tilde{f}\langle v'w'\rangle \end{matrix} & -2f\langle u'v'\rangle & \begin{matrix} -f\langle u'w'\rangle \\ +\tilde{f}\langle u'v'\rangle \end{matrix} \\[2em]
\begin{matrix} \tilde{f}\left(\langle u'^2\rangle - \langle w'^2\rangle\right) \\ +f\langle v'w'\rangle \end{matrix} & \begin{matrix} -f\langle u'w'\rangle \\ +\tilde{f}\langle u'v'\rangle \end{matrix} & 2\tilde{f}\langle u'w'\rangle
\end{pmatrix} \qquad . \tag{A.31}$$

In the same way, the Coriolis terms entering (2.9),

$$F_i^{\theta u} = -f_{il}\langle\theta'u'_l\rangle \; , \tag{A.32}$$

can be simplified and re-written as

$$F_i^{\theta u} = \begin{pmatrix} f\langle\theta'v'\rangle - \tilde{f}\langle\theta'w'\rangle \\ -f\langle\theta'u'\rangle \\ \tilde{f}\langle\theta'u'\rangle \end{pmatrix} \quad . \tag{A.33}$$

Note, that both components of the Coriolis parameter, f and $\tilde{f}$, are retained in (A.31) and (A.33), even though $\tilde{f}$ has been cancelled from the mean momentum budget, (2.37), by scaling arguments. However, there is no a-priori reason, why the horizontal turbulent fluctuations should not be of the same order of magnitude as the vertical fluctuations, considering only the scales that are supposed to be captured by the turbulence model.

A.3 Conversion Relations for the Model of Canuto et al. [37, 38]

The pressure-strain model of CANUTO ET AL. [37, 38], written in the notation used by the authors themselves (and defined in (2.13)), is expressed by

$$\phi_{ij} = -c_1\tau_p^{-1}\left(\langle u_i'u_j'\rangle - \delta_{ij}\frac{2}{3}k\right) + \frac{4}{5}kS_{ij}$$

$$+ \quad \alpha_1\Sigma_{ij} + \alpha_2 Z_{ij} - (1-\beta_5)\left(G_{ij} - \frac{2}{3}\delta_{ij}G\right) \quad .$$

Inserting the expression (A.22) and (A.24) into this equation, the pressure-strain model reads

$$\phi_{ij} = -c_1\tau_p^{-1}\left(\langle u_i'u_j'\rangle - \delta_{ij}\frac{2}{3}k\right) + \frac{4}{5}kS_{ij} - (1-\beta_5)\left(G_{ij} - \frac{2}{3}\delta_{ij}G\right)$$

$$\tag{A.34}$$

$$- \quad \frac{\alpha_1}{2}(P_{ij} + D_{ij}) - \alpha_1\frac{4}{3}kS_{ij} + \alpha_1\frac{2}{3}\delta_{ij}P - \frac{\alpha_2}{2}(P_{ij} - D_{ij}) - \frac{\alpha_2}{2}F_{ij} \; ,$$

which can be recast in the form

$$\phi_{ij} = -c_1\tau_p^{-1}\left(\langle u_i'u_j'\rangle - \delta_{ij}\frac{2}{3}k\right) - \left(\frac{4}{3}\alpha_1 - \frac{4}{5}\right)kS_{ij} - (1-\beta_5)\left(G_{ij} - \frac{2}{3}\delta_{ij}G\right)$$

$$- \quad \frac{\alpha_1 + \alpha_2}{2}\left(P_{ij} - \frac{2}{3}\delta_{ij}P\right) - \frac{\alpha_1 - \alpha_2}{2}\left(D_{ij} - \frac{2}{3}\delta_{ij}P\right) - \frac{\alpha_2}{2}F_{ij} \quad .$$

$$\tag{A.35}$$

Comparison of this equation with (2.12) reveals that the model of CANUTO ET AL. [37, 38] and the traditional model of GIBSON AND LAUNDER [87, 88] are isomorphic for the case of no rotation, if the relations

$$
\begin{aligned}
c_2 &= \frac{\alpha_1 + \alpha_2}{2}, & c_3 &= (1 - \beta_5), \\[2mm]
c_4 &= \frac{\alpha_1 - \alpha_2}{2}, & c_5 &= \frac{4}{3}\alpha_1 - \frac{4}{5},
\end{aligned}
\tag{A.36}
$$

obtained by inspection, are used.

Using the pressure-strain model (2.13), the transport equations for the Reynolds stress tensor (2.8) can be written as

$$
\begin{aligned}
\frac{\partial \langle u'_i u'_j \rangle}{\partial t} + u_l \frac{\partial \langle u'_i u'_j \rangle}{\partial x_l} &= \mathcal{D}_{ij} + P_{ij} + G_{ij} + F_{ij} - c_1 \tau_p^{-1} \left(\langle u'_i u'_j \rangle - \frac{2}{3}\delta_{ij}k \right) \\[3mm]
&+ \frac{4}{5}kS_{ij} - (1 - \beta_5)\left(G_{ij} - \frac{2}{3}\delta_{ij}G \right) \\[3mm]
&+ \alpha_1 \Sigma_{ij} + \alpha_2 Z_{ij} - \frac{2}{3}\delta_{ij}\epsilon \quad .
\end{aligned}
\tag{A.37}
$$

This equation should be contrasted to (2.24), to which it can be easily converted if the parameter relations (A.36) are used.

With some moderate algebra, (A.37) can be written very compactly in the form

$$
\begin{aligned}
\frac{\partial b_{ij}}{\partial t} + u_l \frac{\partial b_{ij}}{\partial x_l} &= \mathcal{D}^b_{ij} - c_1 \tau_p^{-1} b_{ij} - (1 - \alpha_1)\Sigma_{ij} - (1 - \alpha_2)\widetilde{Z}_{ij} \\[3mm]
&- \frac{8}{15}kS_{ij} + \beta_5 \left(G_{ij} - \frac{2}{3}\delta_{ij}G \right),
\end{aligned}
\tag{A.38}
$$

where $\mathcal{D}^b_{ij}$ denotes the turbulent diffusion of the anisotropy tensor b_{ij}, introduced in (2.16). The new tensor $\widetilde{Z}_{ij}$ is defined by

$$
\widetilde{Z}_{ij} = \widetilde{W}_{il}b_{lj} + \widetilde{W}_{jl}b_{li},
\tag{A.39}
$$

where the skew-symmetric part of the velocity gradient in its modified form

$$
\widetilde{W}_{ij} = W_{ij} + \frac{2 - \alpha_2}{1 - \alpha_2}\epsilon_{ilj}\Omega_l = W_{ij} + \frac{2 - \alpha_2}{2(1 - \alpha_2)}f_{ij}
\tag{A.40}
$$

has been used. Note, that the definition (A.40) is not in contradiction to the mandatory form $(2.17)_3$. It is merely a consequence of algebraic manipulations in order to absorb both, the explicit (i.e.: F_{ij}) and the implicit Coriolis terms in the tensor $\widetilde{Z}_{ij}$.

The linear part of the model for the pressure-temperature-gradient correlations, suggested by CANUTO ET AL. [37, 38] reads

$$\phi_i^\theta = -\frac{5}{2}\left(1 + \frac{1}{\sigma_t}\right)\tau_p^{-1}\langle\theta'u_i'\rangle + \frac{3}{4}\alpha_3 S_{ij}\langle\theta'u_j'\rangle + \frac{5}{4}\alpha_3 W_{ij}^*\langle\theta'u_j'\rangle - \gamma_1 G_i^{\theta u} , \qquad (A.41)$$

if the original notation suggested by the authors is used. It is obvious, that this model can be converted to the form (2.19), re-written here for convenience as

$$\phi_i^\theta = -c_1^\theta \tau_p^{-1}\langle\theta'u_i'\rangle + c_2^\theta S_{ij}\langle\theta'u_j'\rangle + c_3^\theta W_{ij}^*\langle\theta'u_j'\rangle - c_4^\theta G_i^{\theta u} ,$$

if the following parameter relations are used:

$$
\begin{aligned}
c_1^\theta &= \frac{5}{2}\left(1 + \frac{1}{\sigma_t}\right), & c_2^\theta &= \frac{3}{4}\alpha_3 , \\
c_3^\theta &= \frac{5}{4}\alpha_3 , & c_4^\theta &= \gamma_1 .
\end{aligned}
\qquad (A.42)
$$

By inspection, the model constant c^θ appearing in (2.22) is found to be $c^\theta = 2\sigma_t$. With these relations and the original model constants from Tab. A.1, the values in Tab. 2.1 and Tab. 2.2 have been computed.

Using (2.19), the balance equation for the turbulent heat flux (2.9) can be written as

$$
\begin{aligned}
\frac{\partial\langle\theta'u_i'\rangle}{\partial t} + u_l\frac{\partial\langle\theta'u_i'\rangle}{\partial x_l} =&\ \mathcal{D}_i^{\theta u} + P_i^{\theta u 1} + P_i^{\theta u 2} + G_i^{\theta u} + F_i^{\theta u} \\
&- c_1^\theta \tau_p^{-1}\langle\theta'u_i'\rangle + c_2^\theta S_{il}\langle\theta u_l'\rangle + c_3^\theta W_{il}^*\langle\theta u_l'\rangle - c_4^\theta G_i^{\theta u} .
\end{aligned}
\qquad (A.43)
$$

With the help of the convenient definition

$$\overline{W}_{ij} = W_{ij} + \frac{2 - c_3^\theta}{2(1 - c_3^\theta)}f_{ij} , \qquad (A.44)$$

analogous to (A.40), the transport equation for the turbulent heat flux (A.43) can be re-written in compact form as

$$
\begin{aligned}
\frac{\partial\langle\theta'u_i'\rangle}{\partial t} + u_l\frac{\partial\langle\theta'u_i'\rangle}{\partial x_l} =&\ \mathcal{D}_i^{\theta u} + P_i^{\theta u 1} - c_1^\theta \tau_p^{-1}\langle\theta'u_i'\rangle \\
&- (1 - c_2^\theta)S_{il}\langle\theta u_l'\rangle - (1 - c_3^\theta)\overline{W}_{il}\langle\theta u_l'\rangle + (1 - c_4^\theta)G_i^{\theta u}.
\end{aligned}
\qquad (A.45)
$$

Note again, that the definition (A.44) is not in contradiction to the compulsory form $(2.17)_3$. It merely follows as a result of the algebraic manipulations leading to the particularly compact form of (A.45), which coincides with (2.25) in the main part.

Table A.1:   Model constants of CANUTO ET AL. [37, 38]

c_1 (by insp.)	α_1	α_2	α_3	β_5	γ_1	σ_t
2.5	0.984	0.568	0.8	0.6	0.333	0.72

A.4   Conversion Between Mellor-Yamada and k-ϵ Parameters

In this section conversion relations between the model constants in the notation of MELLOR AND YAMADA [168, 169] and in the notion used in (2.24)–(2.26) are derived. From the definition of the turbulent kinetic energy, defined as $q^2/2$ in MELLOR AND YAMADA [168, 169], and their representation of the rate of dissipation, ϵ, it follows:

$$q = \sqrt{2}k^{\frac{1}{2}} , \quad q^3 = 2\sqrt{2}k^{\frac{3}{2}} , \tag{A.46}$$

and

$$\frac{2}{3}\delta_{ij}\epsilon = \frac{2}{3}\delta_{ij}\frac{q^3}{B_1 l} , \tag{A.47}$$

from which one can conclude that

$$\epsilon = \frac{q^3}{B_1 l} \quad \text{and} \quad l = \frac{2\sqrt{2}k^{\frac{3}{2}}}{B_1 \epsilon} \quad . \tag{A.48}$$

Comparison of the slow pressure-strain model in (2.12) (with $\tau_p = \tau = \frac{k}{\epsilon}$) with the corresponding model of MELLOR AND YAMADA [168, 169] yields

$$\frac{1}{c_1}\frac{k}{\epsilon} = 3A_1\frac{l}{q} \quad . \tag{A.49}$$

Using the relations derived above, the right hand side of this equation can be expressed as

$$3A_1\frac{l}{q} = 6\frac{A_1}{B_1}\frac{k}{\epsilon} , \tag{A.50}$$

leading to

$$c_1 = \frac{B_1}{6A_1} \quad . \tag{A.51}$$

From completely analogous calculations it can be deduced that

$$c_1^\theta = \frac{B_1}{6A_2} \quad \text{and} \quad c^\theta = 2\frac{B_2}{B_1} \quad . \tag{A.52}$$

It also follows simply from inspection that

$$c_5 = -4C_1 \quad . \tag{A.53}$$

Using the model constants fixed in MELLOR AND YAMADA [169] as

$$(A_1, A_2, B_1, B_2, C_1) = (0.92, 0.74, 16.6, 10.1, 0.08) \,, \tag{A.54}$$

the constants in the notation used here can be computed to be

$$(c_1, c_5, c_1^\theta, c^\theta) = (3.007, -0.32, 3.74, 1.217) \quad . \tag{A.55}$$

These are exactly the constants given in Tab. 2.1 and Tab. 2.2.

Appendix B

Shallow-Water Waves in Rotating Channels and Basins

For small to medium size lakes rotational effects in gravity waves are usually manifested as modifications of the solutions in which the rotation of the Earth is ignored. This can be demonstrated by considering the vertically integrated, linearized shallow water equations without friction of the form

$$\frac{\partial \zeta}{\partial t} + \left(\frac{\partial U}{\partial x} + \frac{\partial V}{\partial y} \right) = 0 \ , \tag{B.1}$$

$$\frac{\partial U}{\partial t} - fV = -gh\frac{\partial \zeta}{\partial x} \ , \quad \frac{\partial V}{\partial t} + fU = -gh\frac{\partial \zeta}{\partial y} \ , \tag{B.2}$$

where U and V are the vertically integrated horizontal velocities and ζ is the surface elevation (HUTTER [115]). The *barotropic* modes are obtained by setting h equal to the (constant) water depth, the *baroclinic* modes of a corresponding two-layer model by setting

$$h := h_i = \frac{\Delta \rho}{\rho_0} \frac{h_1 h_2}{h_1 + h_2} \ , \tag{B.3}$$

where $\Delta \rho$ is the density difference between a layer of thickness h_1 above the thermocline and a layer of thickness h_2 below the thermocline, and ρ_0 is a reference density.

For a detailed description of the wave solutions of (B.1) and (B.2) see MORTIMER [177] and HUTTER [115]. In the following only a brief summary of their results is presented.

B.1   Kelvin Waves

Solutions of (B.1) and (B.2) that enjoy a transverse variation of ζ in conformity with the Coriolis term can be constructed. To this end, a half infinite basin with constant depth and bounded at $y = 0$ is investigated; consider wave solutions of the form

$$U = U_0 h \Phi(y) e^{i(kx - \omega t)} , \quad V := 0 , \quad \zeta = \zeta_0 \Phi(y) e^{i(kx - \omega t)} , \tag{B.4}$$

which satisfy the no-flux condition through the side boundary; a forteriori, (B.4) requires V to vanish everywhere in the half space. Substitution of (B.4) in (B.1) and (B.2) yields the dispersion relation

$$c = c_{ph} = \frac{\omega}{k} = \sqrt{gh} , \tag{B.5}$$

and the solutions

$$\Phi(y) = \exp\left(-\frac{f}{c} y\right) , \quad \zeta_0 = \frac{c}{g} U_0 . \tag{B.6}$$

This solutions, named in the honour of Lord Kelvin, are modified in the presence of topography. They will be referred to as "Kelvin-type" waves then. Even though two Kelvin waves of identical frequency travelling in opposite directions can be superposed to yield a quasi-standing wave, it is well-known the Kelvin waves alone cannot satisfy the boundary conditions at the channels ends. However, modifications of the Kelvin wave solution necessary to overcome this complication are usually confined to the boundaries (MORTIMER [177]). In this case, the main part of the solution consists of a Kelvin wave travelling cyclonically around the basin, its amplitude decreasing exponentially towards the centre of the basin (see (B.6)$_1$).

B.2   Poincaré Waves

Kelvin waves have the property that the water particle motion is purely longitudinal. There are other wave solutions of (B.1) and (B.2) that satisfy the boundary condition $V = 0$ at the sides of a channel, however, may have non-trivial transverse velocity inside the channel. Eliminating U and ζ from the equations and seeking plane wave solutions for V,

$$V = V_0(y) \, e^{i(kx - \omega t)} , \tag{B.7}$$

yields the eigenvalue problem

$$\frac{\partial^2 V_0}{\partial y^2} + \left(\frac{\omega^2 - f^2}{gh} - k^2\right) V_0 = 0 , \quad 0 \le y \le B \tag{B.8}$$

for the distribution of V across a channel with the boundary conditions $V_0 = 0$ at $y = 0$ and $y = B$ (see HUTTER [115]). Equations (B.7) and (B.8) describe the Poincaré waves. The solution of (B.8) is

$$V_0 = \overline{V} \sin \left(\frac{m\pi}{B} y \right)$$ (B.9)

with the dispersion relation

$$k^2 = \frac{\omega^2 - f^2}{gh} - \frac{m^2 \pi^2}{B^2} , \quad (m = 1, 2, 3, \dots)$$ (B.10)

or alternatively

$$\omega^2 = f^2 + gh \left(k^2 + \frac{m^2 \pi^2}{B^2} \right) > f^2 + gh \frac{m^2 \pi^2}{B^2} = \omega_{\text{cut}}^2 .$$ (B.11)

Hence, Poincaré waves with real wave numbers, k, must have frequencies that are larger than the inertial frequency. This statement does not apply to the Kelvin waves.

It is also possible to construct solutions for the longitudinal velocity component,

$$U = \left\{ \alpha_m \sin \left(\frac{m\pi y}{B} \right) - \beta_m \cos \left(\frac{m\pi y}{B} \right) \right\} e^{i(kx - \omega t + \pi/2)} ,$$ (B.12)

where

$$\alpha_m = \phi_{km} \frac{\omega}{k} \overline{V} , \quad \beta_m = -\frac{gh}{f} \phi_{km} \frac{m\pi}{Bf} \frac{\omega}{f} \overline{V}$$ (B.13)

and

$$\phi_{km} = \frac{k^2 + \frac{m^2 \pi^2}{B^2}}{k^2 + \frac{m^2 \pi^2}{B^2} \frac{\omega^2}{f^2}} .$$ (B.14)

The above equations describe the barotropic modes of the Poincaré waves. By replacing the constant depth, h, by the equivalent depth, h_i, the baroclinic modes of the corresponding two-layer system are obtained. Modifications of this type of waves by topography are referred to as "Poincaré-type" waves here. As with the Kelvin waves, Poincaré waves alone cannot satisfy the boundary conditions at the channel ends (see HUTTER [115]).

Bibliography

[1] R. Abid and C. G. Speziale. Predicting equilibrium states with Reynolds stress closures in channel flow and homogeneous shear flow. *Phys. Fluids A*, 5(7):1776–1782, 1993.

[2] A. K. M. Ahsan and A. F. Blumberg. Three-dimensional hydrothermal model of Onondaga Lake. *J. Hydraul. Eng.*, 125:912–923, 1999.

[3] D. L. Aksnes and U. Lie. A coupled physical biological pelagic model of a shallow sill fjord. *Estuarine, Coastal and Shelf Science*, 31:459–486, 1990.

[4] J. S. Allen, P. A. Newberger, and J. Federiuk. Upwelling circulation on the oregon continental shelf. Part I: Response to idealized forcing. *J. Phys. Oceanogr.*, 25:1843–1866, 1995.

[5] Anderson et al. LAPACK: A portable linear algebra library for high-performance computers. Technical Report CS-90-105, Computer Science Dept., University of Tennessee, Knoxville, TN, USA, 1990.
(also see `http://www.netlib.org/lapack/`).

[6] L. Armi. Some evidence for boundary mixing in the deep ocean. *J. Geophys. Res.*, 83(C4):1971–1979, 1978.

[7] L. Armi. Effects of variation in eddy diffusivity on property distribution in the oceans. *J. Marine Res.*, 37:515–530, 1979.

[8] J. J. Barton and L. R. Nackman. *Scientific and Engineering C++*. Addison-Wesley, 1994.

[9] E. Bäuerle. Tranverse baroclinic oscillations in Lake Überlingen. *Aquat. Sci.*, 56(2):145–160, 1994.

[10] E. Baum and E. A. Caponi. Modeling the effects of buoyancy on the evolution of geophysical boundary layers. *J. Geophys. Res.*, 97(C10):15513–15527, 1992.

[11] H. Baumert and H. Peters. Second-moment closures and length scales for weakly stratified turbulent shear flows. *J. Geophys. Res.*, 105(C3):6453–6468, 2000.

[12] H. Baumert and G. Radach. Hysteresis of turbulent kinetic energy in nonrotational tidal flows. *J. Geophys. Res.*, 97(C):3669–3677, 1992.

[13] D. Beletsky, W. P. O'Connor, D. J. Schwab, and D. E. Dietrich. Numerical simulation of internal Kelvin waves and coastal upwelling. *J. Phys. Oceanogr.*, 27:1197–1215, 1997.

[14] A. K. Blackadar. The vertical distribution of wind and turbulent exchange in a neutral atmosphere. *J. Geohys. Res.*, 67:3095–3102, 1962.

[15] A. F. Blumberg, L. A. Khan, and J. P. St. John. Three-dimensional hydrodynamic model of New York harbor region. *J. Hydraul. Eng.*, 125:799–816, 1999.

[16] A. F. Blumberg and G. L. Mellor. A description of a three-dimensional coastal ocean circulation model. In N. S. Heaps, editor, *Three-Dimensional Coastal Ocean Models*, volume 4 of *Coastal and Esturaine Sciences*, pages 1–16. American Geophysical Union, 1987.

[17] A. F. Blumberg and D. M. Di Toro. Effects of climate warming on dissolved oxygen concentrations in Lake Erie. *Trans. Am. Fish. Soc.*, 119:210–223, 1990.

[18] G. Booch, J. Rumbaugh, and I. Jacobson. *The Unified Modeling Language User Guide.* Addison-Wesley, 1999.

[19] I. S. Bowen. The ratio of heat losses by conduction and by evaportion from any water surface. *Phys. Rev.*, 27(2):779–787, 1926.

[20] P. Bradshaw. *An Introduction to Turbulence and its Measurement.* Pergamon, 1975.

[21] D. A. Briggs, J. H. Ferziger, J. R Koseff, and S. G. Monismith. Entrainment in a shear-free turbulent mixing layer. *J. Fluid Mech.*, 310:215–241, 1996.

[22] D. A. Briggs, J. H. Ferziger, J. R Koseff, and S. G. Monismith. Turbulent mixing in a shear-free stably stratified two-layer fluid. *J. Fluid Mech.*, 354:175–208, 1998.

[23] H. Bührer and A. H. Ambühl. Die Einleitung von gereingtem Abwasser in Seen. *Z. Hydrol.*, 37:347–369, 1975.

[24] H. Burchard. Note on the q^2l equation by Mellor and Yamada [1982]. *J. Phys. Oceanogr.*, 2000. accepted.

[25] H. Burchard. Simulating the wave-enhanced layer under breaking surface waves with two-equation turbulence models. *J. Phys. Oceanogr.*, 2000. submitted.

[26] H. Burchard. Applied turbulence modelling in marine waters. Habilitation Thesis, submitted to the Department of Geo-Sciences at the University of Hamburg, Germany, February 2001.

[27] H. Burchard and H. Baumert. On the performace of a mixed-layer model based on the $k - \epsilon$ turbulence closure. *J. Geophys. Res. (C5)*, 100:8523–8540, 1995.

[28] H. Burchard and K. Bolding. Comparative analysis of four second-moment turbulence closure models for the oceanic mixed layer. *J. Phys. Oceanogr.*, 2000. accepted.

[29] H. Burchard and E. Deleersnijder. Investigating the stability of algebraic non-equilibrium second-moment turbulence closure models. *Ocean Modelling Online*, 2000. accepted.

[30] H. Burchard and O. Petersen. Models of turbulence in the marine enviroment - a comparative study of two-equation turbulence models. *J. Mar. Syst.*, 21:29–53, 1999.

[31] H. Burchard, O. Peterson, and T. P. Rippeth. Comparing the performance of the mellor-yamada and the $k - \epsilon$ two-equation turbulence models. *J. Geophys. Res. (C5)*, 103:10,543–10,554, 1998.

[32] J. A. Businger et al. Flux-profile relationships in the atmospheric surface layer. *J. Atmos. Sci.*, 28:181–189, 1971.

[33] D. R. Caldwell and T. M Chriss. The viscous sublayer at the sea floor. *Science*, 205:1131–1132, 1979.

[34] C. Cambon and J. F. Scott. Linear and nonlinear models of anisotropic turbulence. *Ann. Rev. Fluid Mech.*, 31:1–53, 1999.

[35] V. M. Canuto. Turbulent convection with overshooting: Reynolds stress approach. *Astrophys. J.*, 392:218–232, 1992.

[36] V. M. Canuto. Turbulent convection with overshooting: Reynolds stress approach. II. *Astrophys. J.*, 416:331–354, 1993.

[37] V. M. Canuto. Large eddy simulation of turbulence: A subgrid scale model including shear, vorticity, rotation, and buoyancy. *Astrophys. J.*, 428:729–752, 1994.

[38] V. M. Canuto, A. Howard, Y. Cheng, and M. S. Dubovikov. Ocean turbulence I: One-point closure model. Momentum and heat vertical diffusivities with and without rotation. *J. Phys. Oceanogr.*, 2000. accepted.

[39] V. M. Canuto and F. Minotti. Stratified turbulence in the atmosphere and oceans: A new subgrid model. *J. Atmos. Sci.*, 50(13):1925–1935, 1993.

[40] V. M. Canuto, F. Minotti, C. Ronchi, M. Ypma, and O. Zeman. Second-order closure PBL model with new third-order moments: Comparison with LES data. *J. Atmos. Sci.*, 51:1605–1618, 1994.

[41] J. Capblancq and J. Catalan. Phytoplankton: Wich and how much. In R. Margalef, editor, *Limnology now: A paradigm of planetary problems*, pages 9–36. Elsevier, 1994.

[42] I. Celik and W. Rodi. Simulation of free-surface effects in turbulent channel flows. *PhysicoChemical Hydrodynamics*, 5(3/4):217–227, 1984.

[43] C. T. Chen and F. J. Millero. Precise thermodynamic properties of natural waters covering only the limnological range. *Limnol. Oceanogr.*, 31(3):657 – 662, 1986.

[44] D. Chen, L. M. Rothstein, and A. J. Busalacchi. A hybrid vertical mixing scheme and its application to tropical ocean models. *J. Phys. Oceanogr.*, 24:2156–2179, 1994.

[45] Y. Cheng and V. M. Canuto. Stably stratified shear turbulence: A new model for the energy dissipation length scale. *J. Atmos. Sci.*, 51(16):2384–2396, 1994.

[46] P. Y. Chou. On the velocity correlations and the solution of the equations of turbulent fluctuation. *Quart. Appl. Math.*, 3:38, 1945.

[47] T. M. Chriss and D. R. Caldwell. Evidence for the influence of form drag on the bottom boundary layer flow. *J. Geophys. Res.*, 87(C6):4148–4154, 1982.

[48] T. M. Chriss and D. R. Caldwell. Universal similarity and the thickness of the viscous sublayer at the ocean floor. *J. Geophys. Res.*, 89(C4):6403–6414, 1984.

[49] B. V. Chubarenko, Y. Wang, I. P. Chubarenko, and K. Hutter. Barotropic wind-driven circulation patterns in a closed rectangular basin of variable depth influenced by a peninsula or an island. *Anales Geophysicae*, 18:706–727, 2000.

[50] T. J. Craft, N. Z. Ince, and B. E. Launder. Recent developments in second-moment closure for buoyancy-affected flows. *Dynamics of Atmospheres and Oceans*, 23:99–114, 1996.

[51] T. J. Craft, B. E. Launder, and K. Suga. Development and application of a cubic eddy-viscosity model of turbulence. *J. Heat and Fluid Flow*, 17:108–115, 1996.

[52] P. D. Craig. Velocity profiles and surface roughness under breaking waves. *J. Geophys. Res.*, 101:1265–1277, 1996.

[53] P. D. Craig and M. L. Banner. Modeling wave-enhanced turbulence in the ocean surface layer. *J. Phys. Oceanogr.*, 24:2546–2559, 1994.

[54] T. Cromwell. Pycnoclines created by mixing in an aquarium tank. *J. Mar. Res.*, 18:73, 1960.

[55] S. D. Culberson and R. H. Piedrahita. Aquaculture pond ecosystem model: temperature and dissolved oxygen prediction – mechanism and application. *Ecol. Model.*, 89:231–258, 1996.

[56] S. J. D. d'Alessio, K. Abdella, and N. A. McFarlane. A new second-order turbulence closure scheme for modeling the oceanic mixed layer. *J. Phys. Oceanogr.*, 28:1624–1641, 1998.

[57] J. W. Deardorff and G. E. Willis. Further results from a laboratory model of the convective planetary boundary layer. *Boundary-Layer Meteor.*, 32:205–236, 1985.

[58] E. Deleersnijder. A note on the stability functions of the Mellor-Yamada level $2\frac{1}{2}$ turbulence closure. *Bulletin de la Société Royale des Sciences de Liège*, 61:397–404, 1992.

[59] E. Deleersnijder and P. Luyten. On the practical advantages of the quasi-equilibrium version of the Mellor and Yamada level 2.5 turbulence closure applied to marine modelling. *Appl. Math. Modelling*, 18:281–287, 1994.

[60] K. L. Denman. A time-dependent model of the upper ocean. *J. Phys. Oceanogr.*, 3:173–184, 1973.

[61] K. L. Denman and A. E. Gargett. Biological-physical interactions in the upper ocean: The role of vertical and small scale processes. *Ann. Rev. Fluid. Mech.*, 27:225–255, 1995.

[62] I. P. D. deSilva, J. Imberger, and G. N Ivey. Localized mixing due to a breaking internal wave ray at a sloping bed. *J. Fluid Mech.*, 350:1–27, 1997.

[63] R. K. Dewey and W. R. Crawford. Bottom stress estimates from vertical dissipation rate profiles on the continental shelf. *J. Phys. Oceanogr.*, 18:1167–1177, 1988.

[64] T. D. Dickey and G. L. Mellor. Decaying turbulence in neutral and stratified fluids. *J. Fluid Mech.*, 99:13, 1980.

[65] T. M. Dillon. Vertical overturns: A comparison of Thorpe and Ozmidov length scales. *J. Geophys. Res.*, 87(C12):9601–9613, 1982.

[66] P. F. Dubois. FORTRAN: A space odyssey. *Computing in Science and Egineering*, 3(2):54–59, 2001.

[67] F. Einaudi and J. J. Finnigan. Wave-turbulence dynamics in the stably stratified boundary layer. *J. Atmos. Sci.*, 50(13):1841–1864, 1993.

[68] V. W. Ekman. On the influence of the earths rotation on ocean-currents. *Ark. Mat. Astr. Fys.*, 2(11):1–52, 1905.

[69] T. H. Ellison and J. S. Turner. Turbulent entrainment in stratified flows. *J. Fluid Mech.*, 6:423–448, 1959.

[70] T. Ezer. On the seasonal mixed layer simulated by a basin-scale ocean model and the Mellor-Yamada turbulence scheme. *J Geophys. Res.*, 105(C7):16843–16855, 2000.

[71] X. Fang and H. G. Stefan. Interaction between oxygen transfer mechanisms in lake models. *J. Env. Eng.*, 121(6):447–454, 1995.

[72] S. Federiuk and J. S. Allen. Upwelling circulation on the oregon continental shelf. Part II: Simulations and comparisons with observations. *J. Phys. Oceanogr.*, 25:1867–1889, 1995.

[73] H. J. S. Fernando. Turbulent mixing in stratified fluids. *Ann. Rev. Fluid Mech.*, 23:455–493, 1991.

[74] J. H. Ferziger and M. Perić. *Computational Methods for Fluid Dynamics*. Springer-Verlag Berlin, 2nd edition, 1999.

[75] B. A. Finlayson and L. E. Scriven. The method of weighted residuals — a review. *Appl. Mech. Rev.*, 19(6):735–748, 1966.

[76] W. C. Forsythe, Jr. E. J. Rykiel, R. S. Stahl, H. Wu, and R. M. Schoolfield. A model comparison for daylength as a function of latitude and day of the year. *Ecol. Model*, 80:87–95, 1995.

[77] U. Franke, K. Hutter, and K. Jöhnk. A physical-biological coupled model for algal dynamics in lakes. *Bulletin of Mathematical Biology*, 61:239–272, 1999.

[78] P. J. S Franks. Coupled physical-biological models in oceanography. *Reviews of Geophysics, Supplement*, pages 1177–1187, 1995.

[79] H. Frey. A three-dimensional, baroclinic shelf sea circulation model — 1. The turbulence closure scheme and the one-dimensional test model. *Cont. Shelf Res.*, 11(4):365–395, 1991.

[80] B. Galperin, L. H. Kantha, S. Hassid, and A. Rosati. A quasi-equilibrium turbulent energy model for geophysical flows. *J. Atmos. Sci.*, 45(1):55–62, 1988.

[81] B. Galperin, A. Rosati, L. H. Kantha, and G. L. Mellor. Modeling rotating stratified turbulent flows with an application to the oceanic mixed layer. *J. Phys. Oceanogr.*, 19:901–916, 1989.

[82] C. Garrett. The role of secondary circulation in boundary mixing. *J. Geophys. Res.*, 95(C3):3181–3188, 1990.

[83] C. Garrett. Marginal mixing theories. *Atmosphere-Ocean*, 29(2):313–339, 1991.

[84] T. B. Gatski and C. G. Speziale. On explicit algebraic stress models. *J. Fluid Mech.*, 254:59–78, 1993.

[85] J. R. Gemmrich and D. M. Farmer. Near-surface turbulence and thermal structure in a wind-driven sea. *J. Phys. Oceanogr.*, 29:480–499, 1999.

[86] T. Gerz, U. Schumann, and S. E. Elghobashi. Direct numerical simulation of stratified homogeneous turbulent shear flows. *J. Fluid Mech.*, 200:563–594, 1989.

[87] M. M. Gibson and B. E. Launder. On the calculation of horizontal, turbulent, free shear flows under gravitational influence. *J. Heat Transfer*, 98C:81–87, 1976.

[88] M. M. Gibson and B. E. Launder. Ground effects on pressure fluctuations in the atmospheric boundary layer. *J. Fluid Mech.*, 86:491–511, 1978.

[89] E. U. Gloor. *Methode der Temperaturmikrostruktur und deren Anwendung auf die Bodengrenzschicht in geschichteten Wasserkörpern.* PhD thesis, Eidgenössische Technische Hochschule (ETH) Zürich, Switzerland, 1995. Nr. 11336.

[90] M. Gloor, A. Wüest, and D. M. Imboden. Dynamics of mixed bottom layers and its implications for diapycnal transport in a stratified, natural water basin. *J. Geophys. Res.*, 105(C5):8629–8646, 2000.

[91] M. Gloor, A. Wüest, and M. Münnich. Benthic boundary mixing and resuspension induced by internal seiches. *Hydrobiologica*, 284:59–68, 1994.

[92] G.-H. Goudsmit, F. Peeters, M. Gloor, and A. Wüest. Boundary versus internal diapycnal mixing in stratified natural waters. *J. Geophys. Res.*, 102(C13):27903–27914, 1997.

[93] M. C. Gregg. Diapycnal mixing in the thermocline: A review. *J. Geophys. Res.*, 92(C5):5249–5286, 1987.

[94] M. C. Gregg. Scaling turbulent dissipation in the thermocline. *J. Geophys. Res.*, 94(C7):9686–9698, 1989.

[95] G. Gust and G. L. Weatherly. Velocities, turbulence, and skin friction in a deep-sea logarithmic layer. *J. Geophys. Res.*, 90(C3):4779–4792, 1985.

[96] P. Güting and K. Hutter. Modelling wind-induced circulation in the homogeneous Lake Constance using a k-ϵ-closure. *Aquatic Sciences*, 60:266–277, 1998.

[97] D. P. Hamilton and S. G. Schladow. Prediction of water quality in lakes and reservoirs. Part I — Model description. *Ecol. Model.*, 96:91–110, 1997.

[98] S. W. Haney. Is C++ fast enough for scientific computing? *Computers in Physics*, 8(6):690–694, 1994.

[99] S. W. Haney. Beating the abstraction penalty in C++ using expression templates. *Computers in Physics*, 10(6):552–557, 1996.

[100] S. W. Haney and J. Crotinger. How templates enable high-performance scientific computing in c++. *Computing in Science and Engineering*, 1(4):66–72, 1999.

[101] K. Hanjalić and B. E. Launder. A reynolds stress model of turbulence and its application to thin shear flows. *J. Fuid Mech.*, 52:609–638, 1972.

[102] I. A. Hannoun, H. J. S. Fernando, and E. J. List. Turbulence structure near a sharp density interface. *J. Fuid Mech.*, 189:189–209, 1988.

[103] I. A. Hannoun and E. J. List. Turbulent mixing at a shear free density interface. *J. Fuid Mech.*, 189:211–234, 1988.

[104] G. P. Harris. Photosynthesis, productivity, and growth: The physiological ecology of phytoplankton. *Archiv für Hydrobiologie, Beiheft 10*, 1978.

[105] C. Häse. *Die Vorhersage der Produktivität des Phytoplanktons im Bodensee unter Berücksichtigung der Temperatur sowie der spektralen Zusammensetzung des Unterwasser-Strahlungsfeldes.* Konstanzer Dissertationen, Vol. 514, University of Konstanz, 1996. Hartung-Gorre Verlag.

[106] S. Hassid and B. Galperin. A turbulent energy model for geophysical flow. *Boundary-Layer Meteor.*, 26:397–412, 1983.

[107] B. Henderson-Sellers. *Engineering Limnology.* Pitman Publishing, Boston, London, Melbourne, 1984.

[108] B. R. Hodges, J. Imberger, and A. Saggio. Modeling basin-scale internal waves in a stratified lake. *Limnol. Oceanogr.*, 2000. in press.

[109] S. E. Holt, J. R. Koseff, and J. H. Ferziger. A numerical study of the evolution and structure of homogeneous stably stratified sheared turbulence. *J. Fluid Mech.*, 237:499–539, 1991.

[110] E. J. Hopfinger. Turbulence in stratified fluids: A review. *J. Geophys. Res.*, 92(C5):5287–5303, 1987.

[111] E. J. Hopfinger and J. A. Toly. Spatially decaying turbulence and its relation to mixing across density interfaces. *J. Fluid Mech.*, 78:155–175, 1976.

[112] K. M. F. Hussain and W. C. Reynolds. The mechanics of an organized wave in turbulent shear flow. *J. Fluid Mech.*, 41:241–258, 1970.

[113] K. M. F. Hussain and W. C. Reynolds. The mechanics of an organized wave in turbulent shear flow. Part 2. Experimental results. *J. Fluid Mech.*, 54:241–261, 1972.

[114] K. Hutter, editor. *Hydrodynamics of Lakes.* Springer-Verlag Berlin, Vienna/New York, 1984. [CISM-Lectures].

[115] K. Hutter. Waves and oscillations in the ocean and in lakes. In K. Hutter, editor, *Continuum Mechanics in Enviromental Sciences and Geophysics.* Springer-Verlag, Berlin/Heidelberg/New York, 1993.

[116] J. Imberger. The diurnal mixed layer. *Limnol. Oceanogr.*, 30(4):737–770, 1985.

[117] J. Imberger. Flux paths in a stratified lake: A review. In J. Imberger, editor, *Physical Processes in Lakes and Oceans*, Coastal and Esturaine Studies, pages 1–17. American Geophysical Union, 1998.

[118] J. Imberger and G. N. Ivey. On the nature of turbulence in a stratified fluid. Part II: Application to lakes. *J. Phys. Oceanogr.*, 21:659–680, 1991.

[119] J. Imberger and G. N. Ivey. Boundary mixing in stratified reservoirs. *J. Fluid. Mech.*, 248:477–491, 1993.

[120] J. Imberger and J. C. Patterson. A dynamic reservoir simulation model - DYRESM:5. In H. Fischer, editor, *Transport models for inland and coastal waters*, pages 310–361, 1981.

[121] D. M. Imboden and S. Emerson. Natural radon and phosphorous as limnological tracers. *Limnol. Oceanogr.*, 23:77–90, 1978.

[122] D. M. Imboden and A. Wüest. Mixing mechanisms in lakes. In A. Lerman, editor, *Lakes*, pages 83–138. Springer, New York, 1994.

[123] E. C. Itseire, K. N. Helland, and C. W. van Atta. The evolution of grid-generated turbulence in a stably stratfied fluid. *J. Fluid Mech.*, 162:299–338, 1986.

[124] E. C. Itsweire, J. R. Koseff, D. A. Briggs, and J. H. Ferziger. Turbulence in stratified shear flows: Implications for interpreting shear-induced mixing in the ocean. *J. Phys. Oceanogr.*, 23:1508–1522, 1995.

[125] G. N. Ivey and J. Imberger. On the nature of turbulence in a stratified fluid. Part I: The energetics of mixing. *J. Phys. Oceanogr.*, 21:650–658, 1991.

[126] F. C. Jacobitz, S. Sarkar, and C. W. van Atta. Direct numerical simulations of the turbulence evolution in a uniformly sheared and stably stratifed flow. *J. Fluid Mech.*, 342:231–261, 1997.

[127] S. Jakarlić. *Reynolds-Spannungs-Modellierung komplexer turbulenter Strömungen*. PhD thesis, University of Erlangen-Nürnberg, Technische Fakultät, Germany, 1997.

[128] A. D. Jassby and T. Platt. Mathematical formulation of the relationship between photosynthesis and light of phytoplankton. *Limnol. Oceanogr.*, 21:540–547, 1976.

[129] K. Joehnk and L. Umlauf. Modelling the metalimnetic oxygen minimum in a medium sized alpine lake. *Ecol. Model.*, 136:67–80, 2001.

[130] K. Jöhnk. 1D Hydrodynamische Modelle in der Limnophysik. Turbulenz-Meromixis-Sauerstoff. Habilitation thesis, Department of Mechanics, Technical University at Darmstadt, Germany, 2000. in German.

[131] K. Jöhnk and K. Hutter. Simulation der Schichtung und des Sauerstoffgehaltes im Ammersee. Final report, Institut zur Erforschung und zum Schutz der Gewässer, Konstanz, Germany, 1998. in German.

[132] W. P. Jones and B. E. Launder. The prediction of laminarization with a two-equation model of turbulence. *Int. J. Heat Mass Transfer*, 15:301–314, 1972.

[133] S. E. Jørgensen. State of the art of ecological modelling in limnology. *Ecol. Model.*, 78:101–115, 1995.

[134] H.-J. Kaltenbach, T. Gerz, and U. Schumann. Large-Eddy simulation of homogeneous turbulence and diffusion in stably stratified shear flow. *J. Fluid Mech.*, 280:1–40, 1994.

[135] L. H. Kantha and C. A. Clayson. An improved mixed layer model for geophysical applications. *J. Geophys. Res.*, 99(C12):25235–25266, 1994.

[136] L. H. Kantha, O. M. Phillips, and R. S. Azad. On turbulent entrainment at a stable density interface. *J. Fluid Mech.*, 79(4):753–768, 1977.

[137] H. Kato and O. M. Phillips. On the penetration of a turbulent layer into stratified fluid. *J. Fluid Mech.*, 37(4):643–655, 1969.

[138] J. Kirk. *Light and Photosynthesis in Aquatic Ecosystems*. Cambridge University Press, Cambridge, 1983.

[139] A. N. Kolmogorov. Local structure of turbulence in incompressible viscous fluid of very large Reynolds number. *Doklady Akademiya Nauk SSSR*, 30:299–301, 1941.

[140] S. Komori, H. Ueda, F. Ogino, and T. Mizushina. Turbulence structure in a stably stratified open-channel flow. *J. Fluid Mech.*, 130:13–26, 1983.

[141] E. B. Kraus and J. S. Turner. A one-dimensional model of the seasonal thermocline - II. The general theory and its consequences. *Tellus*, 19:98–105, 1967.

[142] P. K. Kundu. A numerical investigation of mixed layer dynamics. *J. Phys. Oceanogr.*, 10:320–336, 1980.

[143] P. K. Kundu. Self-similarity in stress-driven entrainment experiments. *J. Geophys. Res.*, 86:1979–1988, 1981.

[144] W. Lampert and U. Sommer. *Limnoecology*. Oxford University Press, Inc., 1997.

[145] W. G Large and G. B. Crawford. Observations and simulations of upper ocean response to wind events during the ocean storms experiment. *J. Phys. Oceanogr.*, 25:2831–2852, 1974.

[146] B. E. Launder. On the effects of a gravitational field on the turbulent transport of heat and momentum. *J. Fluid Mech.*, 67:569–581, 1975.

[147] B. E. Launder, G. J. Reece, and W. Rodi. Progress in the development of Reynolds stress turbulent closure. *J. Fluid Mech.*, 68:537–566, 1975.

[148] B. E. Launder and D. B. Spalding. The numerical computation of turbulent flow. *Comp. Meth. Appl. Mech. Eng.*, 3:269–288, 1974.

[149] U. Lemmin and D. M. Imboden. Dynamics of bottom currents in a small lake. *Limnol. Oceanogr.*, 32(1):62–75, 1987.

[150] J. H. Lienhard and C. W. van Atta. The decay of turbulence in stably stratified flow. *J. Fluid Mech.*, 210:57–112, 1990.

[151] P. F. Linden. The deepening of a mixed layer in a stratified fluid. *J. Fluid Mech.*, 71(2):385–405, 1975.

[152] D. M. Livingstone and D. M. Imboden. The prediction of hypolimnetic oxygen profiles: a plea for a deductive approach. *Can. J. Fish. Aquat. Sci.*, 53:924–932, 1996.

[153] D. M. Livingstone and D. M. Imboden. Reply - The prediction of hypolimnetic oxygen profiles: a plea for a deductive approach. *Can. J. Fish. Aquat. Sci.*, 54:740–741, 1997.

[154] J. L. Lumley. Computational modeling of turbulent flow. *Adv. Appl. Mech.*, 18, 123–176.

[155] J. L. Lumley. Toward a turbulent constitutive equation. *J. Fluid Mech.*, 41(2):413–434, 1970.

[156] P. J. Luyten, E. Deleersnijder, J. Ozer, and K. G. Ruddik. Presentation of a family of turbulence closure models for stratified shallow water flows and preliminary application to the Rhine outflow region. *Cont. Shelf Res.*, 16(1), 1996.

[157] J. Mackerle. Object-oriented techniques in FEM and BEM. A bibliography (1996–1999). *Finite Elements in Analysis and Design*, 36:189–196, 2000.

[158] R. I. Mackie. Object oriented programming of the finite element method. *Int. J. Num. Meth. Eng.*, 35:425–436, 1992.

[159] D. E. Marti and D. M. Imboden. Thermische Energieflüsse am Beispiel der Sempachersee. *Scheiz. Z. Hydrol.*, 48(2):196–228, 1986.

[160] P. J. Martin. Simulation of the mixed layer at OWS November and Papa with several models. *J. Geophys. Res.*, 90(C1):903–916, 1985.

[161] W. McMillan. Cooling from open water surfaces: Part 1: Lake Trawsfynydd cooling investigation. Final Report NW/SSD/RR/1204/73, Scientific Services Department, CEGB Manchester, 1973.

[162] R. O. Megard, D. W. Tonkyn, and W. H. Senft. Kinetics of oxygenic photosynthesis in planktonic algae. *J. Plankt. Res.*, 6(2):325–337, 1984.

[163] G. L. Mellor. Analytic prediction of the properties of planetary surface layers. *J. Atmos. Sci.*, 30:1061–1069, 1973.

[164] G. L. Mellor. One-dimensional ocean surface layer modeling, a problem and a solution. *J. Phys. Oceanogr.*, 2000. in press.

[165] G. L. Mellor and P. A. Durbin. The structure and dynamics of the ocean surface mixed layer. *J. Phys. Oceanogr.*, 3:718–728, 1975.

[166] G. L. Mellor and H. J. Herring. A survey of the mean turbulent field closure models. *AIAA J.*, 11(5):590–599, 1973.

[167] G. L. Mellor and P. T. Strub. Similarity solutions for the stratified turbulent Rayleigh problem. *J. Phys. Oceanogr.*, 10:455–460, 1980.

[168] G. L. Mellor and T. Yamada. A hierarchy of turbulence closure models for planetary boundary layers. *J. Atmos. Sci.*, 31:1791–1806, 1974.

[169] G. L. Mellor and T. Yamada. Development of a tubulence closure model for geophysical fluid problems. *Reviews of Geophysics and Space Physics*, 20(4):851–875, 1982.

[170] D. V. Mironov, V. M. Gryanik, C.-H. Moeng, D. J. Olbers, and T. H. Warncke. Vertical turbulence structure and second-moment budgets in convection with rotation: A large-eddy simulation. *Quart. J. Roy. Meteor. Soc.*, 126:477–516, 2000.

[171] B. Mohammadi and O. Pironeau. *Analysis of the k-ϵ Turbulence Model.* Research in Applied Mathematics. John Wiley & Sons, 1994.

[172] J. R. Moisan and E. E. Hofmann. Modeling nutrient and plankton processes in the California coastal transition zone. 1. A time- and depth-dependent model. *J. Geophys. Res.*, 101:22647–22676, 1996.

[173] J. R. Moisan, E. E. Hofmann, and D. B. Haidvogel. Modeling nutrient and plankton processes in the California coastal transition zone. 2. A three dimensional physical-bioptical model. *J. Geophys. Res.*, 101:22677–22691, 1996.

[174] L. A. Molot. Comment - The prediction of hypolimnetic oxygen profiles: a plea for a deductive approach. *Can. J. Fish. Aquat. Sci.*, 54:739, 1997.

[175] A. S. Monin and A. M. Obukhov. Basic laws of turbulent mixing in the ground layer of the atmosphere. *Akad. Nauk USSR Geofiz. Inst. Tr.*, 153:163–187, 1954.

[176] M. J. Moore and R. R. Long. An experimental investigation of stratified shearing flow. *J. Fluid Mech.*, 49(4):635–655, 1971.

[177] C. H. Mortimer. Lake hydrodynamics. *Mitt. Internat. Verein. Limnol.*, 20:174–197, 1974.

[178] C. H. Mortimer. The oxygen content of air-saturated fresh waters over ranges of temperature and atmospheric pressure of limnological interest. *Mitt. Internat. Verein. Limnol.*, 22:1–23, 1981.

[179] J. N. Moum. Energy-containing scales of turbulence in the ocean thermocline. *J. Geophys. Res.*, 101(C6):14095–14109, 1996.

[180] W. H. Munk and E. R. Anderson. Notes on the theory of the thermocline. *J. Mar. Res.*, 3:276–295, 1948.

[181] M. Münnich, A. Wüest, and D. M. Imboden. Observations of the second vertical mode of the internal seiche in an alpine lake. *Limnol. Oceanogr.*, 37(8):1705–1719, 1992.

[182] F. T. M. Nieuwstadt. The turbulent structure of the stable, nocturnal boundary layer. *J. Atmos. Sci.*, 41, 1984.

[183] P. P. Niiler. Deepening of the wind mixed layer. *J. Mar. Res.*, 33, 1975.

[184] R. I. Nokes. On the entrainment rate across a density interface. *J. Fluid Mech.*, 188:185–204, 1988.

[185] A. Omstedt, J. Sahlberg, and U. Svensson. Measured and numerically-simulated autumn cooling in the Bay of Bothnia. *Tellus*, 35A:231–240, 1983.

[186] R. V. Ozmidov. On the turbulent exchange in a stably stratified ocean. *Akad. Nauk USSR Izv. Atmos. Ocean Phys.*, 1(8):853–860, 1965.

[187] R. C. Pacanowsci and S. G. H. Philander. Parameterization of vertical mixing in numerical models of tropical oceans. *J. Phys. Oceanogr.*, 11:1443–1451, 1981.

[188] R. A. Parker. Eddy diffusion of phytoplankton and nutrients: estimating coefficients from simulated and observed vertical distributions. *J. Plankton. Res*, 13:815–830, 1991.

[189] S. V. Patankar. *Numerical Heat Transfer and Fluid Flow*. Taylor & Francis, 1980.

[190] J. C. Patterson, B. R. Allenson, and G. N. Ivey. A dissolved oxygen budget model for Lake Erie in summer. *Freshwater Biology*, 15:683–694, 1985.

[191] P. S. Piccarillo and C. W. van Atta. The evolution of a uniformly sheared thermally stratified turbulent flow. *J. Fluid Mech.*, 334:61–68, 1997.

[192] R. T. Pollard, P. B. Rhines, and R. O. R. Y. Thompson. The deepening of the wind mixed layer. *Geophys. Fluid Dyn.*, 3:381–404, 1973.

[193] L. Prandtl. Bericht über Untersuchungen zur ausgebildeten Turbulenz. *Zeitschrift für angewandte Mathematik und Mechanik*, 5(2):136, 1925.

[194] L. Prandtl. Über ein neues Formelsystem für die ausgebildete Turbulenz. *Nachr. Akad. Wiss. Göttingen, math. phys. Klasse*, pages 6–19, 1945.

[195] J. F. Price. On the scaling of stress driven entrainment experiments. *J. Fluid Mech.*, 90(3):509–529, 1979.

[196] J. F. Price, C. N. K. Mooers, and J. C. van Leer. Observation and simulation of storm-induced mixed-layer deepening. *J. Phys. Oceanogr.*, 8:582–599, 1978.

[197] R. Rajar and M. Cetina. Hydrodynamic and water qualitiy modelling: An experience. *Ecol. Model.*, 101:195–207, 1997.

[198] J. N. Reddy. *An Introduction to the Finite Element Method*. McGraw-Hill, Inc., New York, 2nd edition, 1993.

[199] C. S. Reynolds. Plants in Motion: Physical-Biological Interaction in the Plankton. In J. Imberger, editor, *Physical Processes in Lakes and Oceans*, Coastal and Esturaine Studies, pages 535–560. American Geophysical Union, 1998.

[200] K. J. Richards. Modeling the benthic boundary layer. *J. Phys. Oceanogr.*, 12:428–439, 1982.

[201] R. A. Richardson, G. G. Sutyrin, D. Hebert, and L. M. Rothstein. Universality of the modeled small-scale response of the upper tropical ocean to squall wind forcing. *J. Phys. Oceanogr.*, 29(3):519–529, 1999.

[202] M. J. Riley and H. G. Stefan. MINLAKE: A dynamic lake water quality simulation model. *Ecol. Model.*, 43:155–182, 1988.

[203] R. D. Robarts and P. R. B. Ward. Vertical diffusion and nutrients transport in a tropical lake (Lake McIllwaine, Rhodesia. *Hydrobiologia*, 59:213–221, 1978.

[204] A. D. Robinson. C++ gets faster for scientific computing. *Computers in Physics*, 10(5):458–462, 1996.

[205] W. Rodi. A new algebraic relation for calculating the Reynolds stresses. *Z. angew. Math. Mech.*, 56:T 219–T 221, 1976.

[206] W. Rodi. Examples of calculation methods for flow and mixing in stratified fluids. *J. Geophys. Res. (C5)*, 92:5305–5328, 1987.

[207] W. Rodi. *Tubulence Models and Their Application to Hydraulics*. IAHR Monograph Series. A. A. Balkema, Rotterdam/Brookfield, 1993.

[208] J. J. Rohr, E. C. Itsweire, K. N. Helland, and C. W. van Atta. Growth and decay of turbulence in a stably stratified shear flow. *J. Fluid Mech.*, 195:77–111, 1988.

[209] J. Rotta. Statistische Theorie nichthomogener Turbulenz. 1. Mitteilung. *Z. Phys.*, 129:547–572, 1951.

[210] J. Rotta. Statistische Theorie nichthomogener Turbulenz. 2. Mitteilung. *Z. Phys.*, 131:51–77, 1951.

[211] H. Rouse and J. Dodu. Diffusion turbulente à travers une discontinuité de densité. *Houille Blanche*, 10:522, 1955.

[212] A. Sadiki, , W. Bauer, and K. Hutter. Thermodynamically consistent coefficient calibration in nonlinear and anisotropic closure models for turbulence. *Continuum Mech. Thermodyn.*, 12:131–149, 2000.

[213] A. Sadiki and K. Hutter. On the frame dependence and form invariance of the transport equations for the Reynolds stress tensor and the turbulent heat flux vector: its consequences on closure models in turbulence modelling. *Continuum Mech. Thermodyn.*, 8:341–349, 1996.

[214] A. Sadiki and K. Hutter. On thermodynamics of turbulence: Development of first order closure models and critical evaluation of existing models. *J. Non-Equilib. Thermodyn.*, 25:131–160, 2000.

[215] J. Sander. Dynamical equations and turbulent closures in geophysics. *Continuum Mech. Thermodyn.*, 10:1–28, 1998.

[216] S. G. Schladow and D. P. Hamilton. Prediction of water quality in lakes and reservoirs. Part II — Model calibration, sensitivity analysis and application. *Ecol. Model.*, 96:111–123, 1997.

[217] H. Schlichting and K. Gersten. *Boundary Layer Theory*. Springer, 8th edition, 2000.

[218] U. Schumann. The countergradient heat flux in turbulent shear flows. *Nucl. Eng. Des.*, 100:255–262, 1987.

[219] U. Schumann. Subgrid length-scales for large-eddy simulation of stratified turbulence. *Theoret. Comput. Fluid Dynamics*, 2:279–290, 1991.

[220] U. Schumann and T. Gerz. Turbulent mixing in stably stratified shear flows. *J. Appl. Meteorol.*, 34:33–48, 1995.

[221] J. Schwoerbel. *Einführung in die Limnologie*. Gustav Fischer Verlag, Stuttart, Jena, 7th edition, 1993.

[222] F. S. Sherman, J. Imberger, and G. M. Corcos. Turbulence and mixing in stably stratified waters. *Ann. Rev. Fluid Mech.*, 10:267–288, 1978.

[223] T. S. Shih and A. Shabbir. Advances in modeling the pressure correlation terms in the second moment equations. In T. B. Gatsky, S. Sarkar, and C. G. Speziale, editors, *Studies in Turbulence*, pages 91–128. Springer, New York, 1992.

[224] N. Shima. Prediction of turbulent boundary layers with second-moment closure: Part I — effects of periodic pressure gradient, wall transpiration, and free-stream turbulence. *J. Fluids Eng.*, 115:56–63, 1993.

[225] C. C. Shir. A preliminary numerical study of atmospheric turbulent flows in the idealized planetary boundary layer. *J. Atmos. Sci.*, 30:1327–1339, 1973.

[226] J. G. Siek and A. Lumsdaine. The Matrix Template Library: Generic components for high-performance scientific computing. *Computing in Science and Engineering*, 1(6):70–78, 1999. (also see `http://www.lsc.nd.edu/research/mtl/`).

[227] J. F. A. Sleath. Turbulent oscillatory flow over rough beds. *J. Fluid Mech.*, 182:369–409, 1987.

[228] T. J. Smith and H. S. Takhar. On the calculation of the width averaged flow due to long waves in an open channel. *J. Hydr. Res.*, 17(4):329–340, 1979.

[229] T. J. Smith and H. S. Takhar. A mathematical model for partially mixed estuaries using the turbulence energy equation. *Estuarine, Coastal and Shelf Science*, 13:27–45, 1981.

[230] R. L. Soulsby and K. R. Dyer. The form of the near-bed velocity profile in a tidally accelerating flow. *J. Geophys. Res.*, 86(C9):8067–8074, 1981.

[231] S. Soyupak, L. Mukhallalati, D. Yemişen, A. Bayar, and C. Yurteri. Evaluation of eutrophication control strategies for the Keban Dam reservoir. *Ecol. Model.*, 97:99–110, 1997.

[232] C. G. Speziale. Invariance of turbulent closure models. *Physics Fluids*, 22:1033–1037, 1979.

[233] C. G. Speziale. On turbulent Reynolds stress closure and modern continuum mechanics. *Int. J. Non-Linear Mechanics*, 16(3/4):387–393, 1981.

[234] C. G. Speziale. Closure models for rotating two-dimensional turbulence. *Geophys. Astrophys. Fluid Dynamics*, 23:69–84, 1983.

[235] C. G. Speziale. On nonlinear k-l and k-ϵ models of turbulence. *J. Fluid. Mech.*, 178:459–475, 1987.

[236] C. G. Speziale. Turbulence modeling in noninertial frames of reference. *Theoret. Comput. Fluid Dynamics*, 1:3–19, 1989.

[237] C. G. Speziale. Analytical methods for the development of Reynolds-stress closures in turbulence. *Ann. Rev. Fluid Mech.*, 23:107–157, 1991.

[238] C. G. Speziale. Comparison of explicit and traditional algebraic stress models of turbulence. *AIAA J.*, 35(9):1506–1509, 1997.

[239] C. G. Speziale and N. M. G. Mhuiris. On the prediction of equilibrium states in homogeneous turbulence. *J. Fluid. Mech.*, 200:591–615, 1989.

[240] R. H. Spigel, J. Imberger, and K. N. Rayner. Modeling the diurnal mixed layer. *Limnol. Oceanogr.*, 31(3):533–556, 1986.

[241] J. H. Spurk. *Dimensionsanalyse.* Springer-Verlag, Berlin, 1992.

[242] P. K. Stansby. Semi-implicit finite volume shallow water flow and solute transport solver with k-ϵ turbulence model. *Int. J. Numer. Meth. Fluids*, 25:285–313, 1997.

[243] H. G. Stefan et al. Simulation of dissolved oxygen profiles in a transparent, dimictic lake. *Limnol. Oceanogr.*, 40(1):105–118, 1995.

[244] H. G. Stefan and X. Fang. Dissolved oxygen model for regional lake analysis. *Ecol. Model.*, 71:37–68, 1995.

[245] M. M. Steiner, W. Wenzel, J. W. Wilkins, and K. G. Wilson. Object-oriented techniques in large scientific computing projects: Experience with C++. *Computers and Physics*, 11(5):467–473, 1997.

[246] A. Sterl and A. Kattenberg. Embedding a mixed layer model into an ocean general circulation model of the Atlantic: Tthe importance of surface mixing for heat flux and temperature. *J. Geophys. Res.*, 99:14139–14157, 1994.

[247] D. C. Stillinger, K. N. Helland, and C. W. van Atta. Experiments on the transition of homogeneous turbulence to internal waves in a stratified fluid. *J. Fluid. Mech.*, 131:91–122, 1983.

[248] B. Stroustrup. *The C++ Programming Language*. Addison-Wesley, 3rd edition, 1997.

[249] U. Svensson. A mathematical model of the seasonal thermocline. Report 1002, Dept. of Water Resoureces Eng. Univ. of Lund, Sweden, 1978.

[250] U. Svensson. The structure of the turbulent Ekman layer. *Tellus*, 31:340–350, 1979.

[251] U. Svensson and J. Sahlberg. Formulae for pressure gradients in one-dimensional lake models. *J. Geophys. Res. (C4)*, 94:4939–4946, 1989.

[252] H. E. Sweers. A nomogram to estimate the heat-exchange coefficient at the air-water interface as a function of wind speed and temperature; a critical survey of some literature. *J. Hydrol.*, 30:375–401, 1976.

[253] W. C. Swinbank. Long-wave radiation from clear skies. *Quat. J. Roy. Meteor. Soc.*, 89:339–348, 1963.

[254] S. Tavoularis and S. Corrsin. Experiments in a nearly homogenous turbulent shear flow with a uniform mean temperature gradient. Part 1. *J. Fluid Mech.*, 104:311–348, 1981.

[255] S. Tavoularis and S. Corrsin. Experiments in a nearly homogenous turbulent shear flow with a uniform mean temperature gradient. Part 2. The fine structure. *J. Fluid Mech.*, 104:349–367, 1981.

[256] S. Tavoularis and U. Karnik. Further experiments on the evolution of turbulent stresses and scales in uniformly sheared turbulence. *J. Fluid Mech.*, 204:457–478, 1989.

[257] H. Tennekes. The decay of turbulence in plane homogeneous shear flow. In J. R. Herring and J. C. McWilliams, editors, *Lecture Notes on Turbulence*, pages 32–35. World Scientific, 1989.

[258] H. Tennekes and J. L. Lumley. *A First Course in Turbulence.* MIT Press, 1972.

[259] R. V. Thomann and J. A. Mueller. *Principles of surface water quality modelling and control.* Harper & Row Publ., New York, 1987.

[260] T. G. Thomas and H. S. Takhar. Turbulent mass transport and attenuation in Stokes waves. *Appl. Sci. Res.*, 49:1–29, 1992.

[261] R. O. R. Y. Thompson. A re-interpretation of the entrainment process in some laboratory experiments. *Dyn. Atmos. Oceans*, 4:45–55, 1979.

[262] S. M. Thompson and J. S. Turner. Mixing across an interface due to turbulence generated by an oscillating grid. *J. Fluid Mech.*, 67:349–368, 1957.

[263] S. A. Thorpe. A method of producing a shear flow in a stratified fluid. *J. Fluid Mech.*, 32(4):693–704, 1968.

[264] S. A. Thorpe. Experiments on the instability of stratified shear flows: miscible fluids. *J. Fluid Mech.*, 46(2):299–319, 1971.

[265] S. A. Thorpe. Experiments on instability and turbulence in a stratified shear flow. *J. Fluid Mech.*, 61(4):731–751, 1973.

[266] S. A. Thorpe. Turbulence in stratified fluids: A review of laboratory experiments. *Boundary-Layer Meteorol.*, 5:95–119, 1973.

[267] S. A. Thorpe. Turbulence and mixing in a Scottish loch. *Phil. Trans. R. Soc. London*, A 286:125–181, 1977.

[268] S. A. Thorpe. The dynamics of the boundary layers of the deep ocean. *Sci. Prog. Oxf.*, 72:189–206, 1988.

[269] W. Törning and P. Spellucci. *Numerische Mathematik fr Physiker und Ingenieure*, volume 2. Springer-Verlag, Berlin, 1990.

[270] A. A. Townsend. *The Structure of Turbulent Shear flow.* Cambridge University Press, 1976.

[271] H. J. Tucker and A. J. Reynolds. The distortion of turbulence by irrotational strain. *J. Fluid. Mech.*, 32:657–673, 1968.

[272] J. S. Turner. The influence of molecular diffusivity on the turbulent entrainment across a density interface. *J. Fluid Mech.*, 33(4):639–659, 1968.

[273] J. S. Turner. *Buoyancy Effects in Fluids.* Cambridge at the University Press, 1973.

[274] J. S. Turner and E. B. Kraus. A one-dimensional model of the seasonal thermocline - I. A laboratory experiment and its interpretation. *Tellus*, 19:88–97, 1967.

[275] M.-H. Tusseau, C. Lancelot, J.-M. Martin, and B. Tassin. 1-D coupled physical-biological model of the northwestern Mediterranean Sea. *Deep-Sea Res. II*, 44(3-4):851–880, 1997.

[276] Y. Tzur. One-dimensional diffusion equations fr the vertical transport in an oscillating stratified lake of varying cross-section. *Tellus*, 25:266–271, 1973.

[277] L. Umlauf. Strömungsdynamik im Ammersee. Diploma-thesis, Technical University of Darmstadt, Department of Mechanics III, Darmstadt, Germany, 1997.

[278] L. Umlauf. The behavior of stability functions in structural equilibrium turbulent flows. 2001. in preparation.

[279] L. Umlauf and H. Burchard. New analytical solutions for two-equation models in the wave-affected oceanic surface layer. 2001. in preparation.

[280] L. Umlauf and K. Hutter. The performance of a buoyancy extended k-ω model in weakly stratified turbulent shear flows. 2001. in preparation.

[281] L. Umlauf and K. Jöhnk. Modelling the oxygen stratification in Lake Ammer. In Madis-Jaak Lilover and Anu Reinhart, editors, *Proc. 4th Workshop on Physical Processes in Natural Waters*, number 10 in Report Series, pages 84–91, Tallin, Estonia, 1999. Estonian Marine Institute.

[282] L. Umlauf and A. Lorke. Modelling the seiche induced bottom boundary layer in a small alpine lake. 2001. in preparation.

[283] L. Umlauf, Y. Wang, and K. Hutter. Comparing two topography-following primitive equation models for lake circulation. *J. Comp. Phys.*, 153:638–659, 1999.

[284] B. G. Vager and B. A. Kagan. The dynamics of the turbulent boundary layer in a tidal current. *Izv. Acad. Sci. USSR Atmos. Oceanic Phys.*, 21:103–111, 1999.

[285] Y. Wang. *Windgetriebene Strmungen in einem Rechteckbecken und im Bodensee.* PhD thesis, Technische Hochschule Darmstadt, FB6, 1995.

[286] Y. Wang and K. Hutter. A semi-implicit semispectral primitive equation model for lake circulation and its stability performance. *J. Comput. Phys.*, 139:209–241, 1998.

[287] Y. Wang and K. Hutter. Methods of substructuring in lake circulation dynamics. *Adv. Water Resour.*, 23:399–425, 2000.

[288] R. Wannikhof, J. Ledwell, and J. Crusius. Gas transfer velocities in lakes measured with sulfur hexafluoride. In S. C. Wilhelms and J. S. Gulliver, editors, *Air water mass transfer*, pages 441–458. ASCE, 1991.

[289] G. L. Weatherly and P. J. Martin. On the structure and dynamics of the oceanic bottom boundary layer. *J. Phys. Oceanogr.*, 8:557–570, 1978.

[290] J. Weinstock. On the theory of turbulence in the buoyancy subrange of stably stratified flows. *J. Atmos. Sci.*, 35:634–649, 1978.

[291] J. Weinstock. Vertical turbulent diffusion in a stably stratified fluid. *J. Atmos. Sci.*, 35:1022–1027, 1978.

[292] R. G. Wetzel. *Limnology.* Saunders College Publ., Fort Worth, 2nd edition, 1983.

[293] D. C. Wilcox. Reassessment of the scale-determining equation for advanced turbulence models. *AIAA Journal*, 26(11):1299–1310, 1988.

[294] D. C. Wilcox. *Turbulence Modeling for CFD.* DCW Industries, Inc., 2nd edition, 1998.

[295] G. E. Willis and J. W. Deardorff. A laboratory model of the unstable planetary boundary layer. *J. Atmos. Sci.*, 31:1297–1307, 1974.

[296] M. K. W. Wong, K. G. Budge, J. S. Peery, and A. C. Robinson. Object-oriented numerics: A paradigm for numerical object-oriented programming. *Computers in Physics*, 7(6):655–663, 1993.

[297] J. D. Woods. Wave-induced shear instability in the summer thermocline. *J. Fluid. Mech.*, 32, 1968.

[298] A. Wüest and M. Gloor. Bottom boundary mixing: The role of near-sediment density stratification. In J. Imberger, editor, *Physical Processes in Lakes and Oceans*, volume 54 of *Coastal and Estuarine Studies*. American Geophysical Union, 1998.

[299] A. Wüest, D. C. van Senden, J. Imberger, G. Piepke, and M. Gloor. Comparison of diapycnal diffusivity measured by tracer and microstructure measurements. *Dyn. Atmos. Oceans*, 24:27–39, 1996.

[300] A. M. Yaglom. Similarity laws for constant-pressure and pressure-gradient turbulent wall flows. *Ann. Rev. Fluid Mech.*, 11:505–540, 1979.

[301] O. Zeman and J. L. Lumley. Modeling buoyancy driven mixed layers. *J. Atmos. Sci.*, 33:1974–1988, 1976.

[302] O. Zeman and J. L Lumley. *Turbulent Shear Flows*. Springer, 1979.

[303] O. Zeman and H. Tennekes. A self-contained model for the pressure terms in the turbulent stress equations of the neutral turbulent boundary layer. *J. Atmos. Sci.*, 32:1808–1813, 1975.

[304] O. Zeman and H. Tennekes. Parameterization of the turbulent energy budget at the top of the daytime atmospheric boundary layer. *J. Atmos. Sci.*, 34:111–123, 1993.

CV

Personal Details:

Full Name:	Lars Umlauf
Date of Birth:	16th October 1969
Nationality:	German

School Education:

Sept. 1976–June 1980	Aachtalschule Baienfurt (Elementary School)
Sept. 1980–Mai 1989	Spohn-Gymnasium Ravensburg (Humanistic Secondary School)

Civil Service:

Okt. 1989–Dez. 1990	Civil Service at the Malteser-Hilfsdienst e.V. (MHD)

University Education:

Okt. 1991–Aug. 1995	Student at the Department of Mechanical Engineering, Technical University of Darmstadt

Sept. 1995–Mai 1996	Student at the Departments of Mechanical Engineering and Mathematics, University of California, Berkeley
Okt. 1996–Jan. 1998	Student at the Department of Mechanics, Technical University of Darmstadt
Diploma Thesis:	Title: "Hydrodynamics of Lake Ammer" (A three-dimensional thermodynamically coupled model of a lake)
Diploma:	"Diplom-Ingenieur Mechanik"
Feb. 1998–Apr. 2001	Ph.D. Student at the Department of Mechanics, Technical University of Darmstadt Research Areas: Turbulence Modelling, Three-Dimensional Lake Modelling, Coupled Physical-Biological Modelling, Object-Oriented Techniques
From Mai 2001	Post-Doctoral Position at the Department of Civil Engineering, EPF Lausanne (Switzerland)